Atmospheric Measurement and Inverse Modeling to Improve Greenhouse Gas Emission Estimates

Contract Number 11-306

Investigators:

Marc L. Fischer and Seongeun Jeong
Lawrence Berkeley National Laboratory

Sally Newman
California Institute of Technology

Jingsong Zhang
University of California, Riverside

February 2016

Prepared for the
California Air Resources Board and
the California Environmental Protection Agency

DISCLAIMER

The statements and conclusions in this Report are those of the contractor and not necessarily those of the California Air Resources Board. The mention of commercial products, their source, or their use in the connection with material reported herein is not to be construed as actual or implied endorsement of such products.

ACKNOWLEDGEMENT

We gratefully acknowledge the team of collaborators who supported the network of GHG and meteorological measurements across California: Arlyn E. Andrews, Ray P. Bambha, Laura Bianco, Dave Bush, Craig Clements, Ed Dlugokencky, Dave Field, Heather Graven, Ralph Keeling, Jooil Kim, Brian W. LaFranchi, Neil Lareau, Scott Lehman, Mathew Lloyd, Hope A. Michelsen, John Miller, Ken Reichl, Peter Salameh, Christopher D. Sloop, Edward Wahl, Toby Walpert, Ray F. Weiss, Xiaomei Xu. We thank Xinguang Cui, Justin Bagley for assistance with modeling, John Lin, Christoph Gerbig, Steve Wofsy, Janusz Eluszkiewicz, Thomas Nehrkorn for sharing the STILT code and advice, Chris Potter and William Salas for sharing modeled CH_4 emission for use as a priori estimates, Ying-Kuang Hsu, Bart Croes, Jorn Herner, Abhilash Vijayan, Matthias Falk, Richard Bode, Anny Huang, Jessica Charrier, Kevin Eslinger, Larry Hunstaker, Ken Stroud, Mac McDougall, Jim Nyarady, and others for sharing CARB emissions information and providing valuable review comments, and Krishna Muriki for assistance running the WRF-STILT models on the LBNL-Lawrencium cluster. This study was funded in large part by the California Air Resources Board (ARB) under contract number 11-306, with support for some of earlier measurements from the University of California's Discovery Grant Program (Grant ID No. 213192) and the California Energy Commission's Natural Gas program, all conducted under U.S. Department of Energy Contract No. DE-AC02-05CH11231.

GLOSSARY OF TERMS, ACRONYMS AND SYMBOLS

Glossary of Terms and Acronyms

AB-32	Assembly Bill 32
AGL	above ground level
AGS	agricultural soils
AIR	aircraft sector for $ffCO_2$
AWB	agricultural waste burning
BAAQMD	Bay Area Air Quality Management District
Bayesian inverse model	an inverse modeling approach that uses a “prior” (guess before observations are taken into account) probability and a "likelihood function" derived from a statistical model (e.g., a normal probability distribution) for the observed data.
classical Bayesian inverse model	as opposed to a hierarchical Bayesian inverse model (see HBI), the uncertainties (e.g., model-measurement mismatch) are prescribed
CALFIRE	California Department of Forestry and Fire Protection
CARB	California Air Resources Board
CALGEM	California Greenhouse Gas Emission Measurements
CalNex	California research study at the nexus of air quality and climate change
CEC	California Energy Commission
CEM	cement production sector for $ffCO_2$
CH_4	methane
CI	confidence interval
CIMIS	California Irrigation Management Information System
CL	confidence level
CO	carbon monoxide
COM	commercial sector for $ffCO_2$
CO_2	carbon dioxide
CP	crop (mostly rice) agriculture
CV	Central Valley
DLS	dairy livestock sector for CH_4
DOE	Department of Energy
DJF	December, January, February
EDGAR	Emission Database for Global Atmospheric Research
EMT	energy manufacturing transformation sector for N_2O
EPA	Environmental Protection Agency
ESRL	Earth System Research Laboratory

Eulerian (approach)	an approach to observing fluid motion with focus on specific locations in the space
$ffCO_2$	fossil fuel carbon dioxide
5-L LSM	five-layer thermal diffusion land surface model
FLEXPART	FLEXible PARTicle dispersion model
footprint	sensitivity of measurements at a site to emissions across the landscape; represents concentration change at the measurement site due to change in the unit emission flux
GEIA	Global Emissions InitiAtive
Gg	giga gram, 10^9 g
GHG	greenhouse gas
GWP	global warming potential; a relative measure of how much heat a greenhouse gas traps in the atmosphere, typically compared to the amount of heat trapped by a similar mass of carbon dioxide
HBI	hierarchical Bayesian inversion; unknown parameters (e.g., model-measurement mismatch covariance) are estimated using probability distributions instead of being prescribed
ICOS	Integrated Cavity Output Spectroscopy
IDE	indirect emissions from NOx & NH_3 sector for N_2O
IND	industrial sector for $ffCO_2$
in-situ	a measurement system where instrumentation is located directly at the site and in contact with the air
inverse model	mathematical estimation technique to calculate the causal factors (e.g., most probable emissions in this study) from a set of observations
IPCC	Intergovernmental Panel on Climate Change
IPU	industrial processes and product use sector for N_2O
ISD	Integrated Surface Database
JAGS	just another Gibbs sampler
JJA	June, July, August
Lagrangian (approach)	an approach to observing fluid motion where the observer follows an individual parcel in space and time
LBNL	Lawrence Berkeley National Laboratory
LGR	Los Gatos Research
length scale	a parameter to characterize how close two points (in space and time) have to be to influence each other significantly; also called correlation length scale
LF	landfill sector for CH_4
lidar	a remote sensing technology that measures distance by illuminating a target with a laser; also written LIDAR
LSM	land surface model
LST	local standard time
MAM	March, April, May
MCMC	Markov chain Monte Carlo

μmol	micromole (10^{-6} mole)
mixing ratio	number of moles of a gas per mole of air or volume of a gas per volume of air; henceforth calculated per mol or volume of dry air
MNM	manure management sector for N_2O
MOB	on-road mobile sector for $ffCO_2$
MODIS	Moderate Resolution Imaging Spectroradiometer
MYNN2	Mellor–Yamada Nakanishi Niino Level 2.5 PBL scheme in WRF
NARR	North American Regional Reanalysis
NOM	non-road mobile sector for $ffCO_2$
N_2O	nitrous oxide
N2O	indirect N_2O emissions from agriculture
NDLS	non-dairy livestock sector for CH_4
NG	natural gas including petroleum production sector for CH_4
nmol	nanomole (10^{-9} mole)
NOAA	National Oceanic and Atmospheric Administration
NOAH	unified Noah land surface model
OPR	oil production & refineries sector for N_2O
PBL	planetary boundary layer; also known as the atmospheric boundary layer (ABL), the lowest part of the atmosphere directly influenced by its contact with a land surface.
PBLH	planetary boundary layer height
per mil	parts per thousand
PMF	Positive Matrix Factorization; a mathematical model for multivariate factor analysis, often used for pollutant source identification by reducing a large number of variables in complex datasets to combinations of source types
pmol	picomole (10^{-12} mole)
posterior	after the relevant observation is taken into account, optimized to the measurements
ppb	parts per billion
ppm	parts per million
prior	before observed data are taken into account
psig	pounds per square inch gage
PST	Pacific Standard Time
radiosonde	telemetry instrument deployed to the atmosphere (mostly by a balloon) that measures various atmospheric variables
RCO	buildings - residential & others sector for N_2O
RES	residential sector for $ffCO_2$
RM	petroleum refining and on-road mobile source sector for CH_4
RMS	root-mean-square
RMSE	root-mean-square error
SF	San Francisco
SFBA	San Francisco Bay Area
SFBI	scaling factor Bayesian inversion

SJSU	San Jose State University
SJV	San Joaquin Valley
SoCAB	South Coast Air Basin
SON	September, October, November
STILT	Stochastic Time-Inverted Lagrangian Transport
Tg	tera gram, 10^{12} g
TNR	non-road transportation sector for N_2O
TRO	road transportation sector for N_2O
UTC	Coordinated Universal Time
UTL	power production for $ffCO_2$
variogram	a function to describe the degree of spatial dependence of a spatial random field; practically the variance of the difference between field values at two locations
VOC	volatile organic compound
WL	wetland sector for CH_4
WRF	Weather Research and Forecasting model
WST	waste - solid & wastewater sector for N_2O
WW	wastewater sector for CH_4
YSU	Yonsei University

Symbols

α	a factor used to determine outliers after the first inversion
C	mixing ratio of CO_2
C_{bg}	background CO_2 mixing ratio
C_{ff}	fossil fuel component of CO_2 mixing ratio
C_{obs}	observed CO_2 mixing ratio
C_r	ecosystem respiration CO_2 mixing ratio
$\mathbf{D}$	generic data in a hierarchical Bayesian model
$\delta_{\mathrm{i,j}}$	Kronecker delta function (value of 1 if i = j, otherwise zero)
$\delta^{13}\mathrm{C}$	stable isotope ratio relative to standard: $(^{13}\mathrm{C}:^{12}\mathrm{C}/^{13}\mathrm{C}_{\mathrm{std}}:^{12}\mathrm{C}_{\mathrm{std}} - 1)$ *1000
$\Delta^{14}\mathrm{C}$	radiocarbon to ^{12}C ratio relative to std: $(^{14}\mathrm{C}:^{12}\mathrm{C}/^{14}\mathrm{C}_{\mathrm{std}}:^{12}\mathrm{C}_{\mathrm{std}} - 1)$ *1000
Δ_{ff}	Δ^{14}C of fossil fuel (typically -1000 per mil (‰), i.e., zero ^{14}C content)
Δ_{bg}	$\Delta^{14}CO_2$ of background air
Δ_{obs}	$\Delta^{14}CO_2$ of sample air
Δ_{r}	$\Delta^{14}CO_2$ of ecosystem respiration
$\mathbf{E}$	prior emissions (in matrix form)
ε	particle velocity error drawn from a Gaussian distribution with mean 0 and standard deviation equal to the observed standard deviation of boundary layer wind error (σ_u)
η	parameter used to construct the model-measurement covariance matrix (**R**) in the hierarchical Bayesian inversion
exp	exponential probability distribution
$\boldsymbol{\theta}$	generic parameters
$\boldsymbol{\Theta}$	joint parameter set estimated in the hierarchical inversion
$\mathbf{F}$	footprint (in matrix form)

$hCauchy$	half-Cauchy probability distribution
$\mathbf{K}$	predicted mixing ratio (in matrix form)
$\boldsymbol{\lambda}$	scaling factor vector
$\boldsymbol{\lambda}_{\mathbf{prior}}$	prior estimate for $\boldsymbol{\lambda}$
$\boldsymbol{\lambda}_{\mathbf{post}}$	posterior estimate for $\boldsymbol{\lambda}$
l_x	horizontal length scale
l_z	vertical length scale
l_t	temporal length scale
$\boldsymbol{\mu}_{\lambda}$	prior mean vector for $\boldsymbol{\lambda}$
N	normal probability distribution
p	probability density function
$\boldsymbol{\Phi}$	generic parameters
$\mathbf{Q}$	error covariance associated with scaling factor $\boldsymbol{\lambda}$
$\mathbf{R}$	model-measurement mismatch covariance matrix
σ	one standard deviation
σ_{dir}	wind direction error; random component represented by standard deviation of model - measurement
$\boldsymbol{\sigma}_{\lambda}$	square root of diagonal elements of uncertainty matrix for $\boldsymbol{\lambda}$ ($\mathbf{Q}$)
$\boldsymbol{\sigma}_{\mathbf{R}}$	parameter (vector) used to construct the model-measurement covariance matrix ($\mathbf{R}$) in the hierarchical inversion
σ_{R_s}	σ_{R} value for measurement site s
$\sigma_{R_{p\|s}}$	first-order prior estimate for σ_{R_s}
σ_{u}	boundary layer wind speed error; random component represented by standard deviation of model - measurement
σ_{zi}	boundary layer depth error; random component represented by standard deviation of model - measurement
τ	parameter used to construct the model-measurement covariance matrix ($\mathbf{R}$) in the hierarchical inversion
τ_{p}	hyper-parameter used to define the probability distribution for τ
$\mathbf{u}$	overall particle velocity vector
$\bar{\mathbf{u}}$	mean component of the particle velocity vector
$\mathbf{u}'$	turbulent component of particle velocity
$unif$	uniform probability distribution
$\mathbf{v}$	model-measurement mismatch vector with mean 0 and covariance matrix $\mathbf{R}$
$\mathbf{y}$	background-subtracted measurement vector
z_i	boundary layer height

TABLE OF CONTENTS

LIST OF FIGURES

LIST OF TABLES

ABSTRACT

California has committed to an ambitious plan to reduce statewide greenhouse gas (GHG) emissions to 1990 levels by 2020 through Assembly Bill 32 (AB-32), which requires accurate accounting of emissions for effective mitigation planning and verification of future emission reductions. Atmospheric GHG measurements from networks of towers can be combined with existing knowledge of emissions in a statistical inverse model -- weighing existing knowledge with the new observations -- to more accurately quantify GHG emissions. This study quantifies major anthropogenic GHGs including fossil fuel CO_2 (ffCO_2), methane (CH_4) and nitrous oxide (N_2O) emissions within California with a Bayesian inverse modeling framework, using atmospheric observations from an expanded GHG measurement network across California over multiple years. We first assess uncertainties in the transport model predictions using a combination of meteorological and carbon monoxide (CO) measurements. Comparison of predicted and measured CO mixing ratios at the four towers during June 2013 – May 2014 yields near-unity slopes (predicted vs. measured) for the majority of sites and seasons, suggesting that the model simulations are sufficient to estimate emissions of CO and likely other GHGs across California to within 10%. The results of this study indicate that ffCO_2 emissions from central California are within 6% of the prior estimate (i.e., the estimate based on existing knowledge before measured data are taken into account), and that in the South Coast Air Basin (SoCAB) ffCO_2 emissions are within 11% of the prior estimate for that region. Combining results from the two regions (i.e., central California and SoCAB), ffCO_2 emissions are consistent to within approximately 10% of the prior estimate.

Summing estimated CH_4 emissions across all air basins (i.e., subregions) of California, posterior results (i.e., results after the relevant atmospheric observation is taken into account) suggest that state annual anthropogenic CH_4 emissions are higher (1.2 - 1.8 times) than the anthropogenic emission in California Air Resources Board's (CARB) current GHG inventory. The estimated CH_4 emissions drop to 1.0 - 1.6 times the CARB inventory if results are corrected for the median CH_4 emissions assuming the 10% model bias in CO is applicable to CH_4. The CH_4 emissions from the Central Valley and major urban regions (SoCAB and San Francisco Bay Area, SFBA) account for 58% and 26 % of the total posterior emissions, respectively. This study combined with other studies suggests the livestock sector is the major contributor to the state total CH_4 emissions, in agreement with CARB's GHG inventory.

Using N_2O measurements from six sites across California, state annual anthropogenic N_2O emissions are estimated to be higher (1.5 – 2.5 times) than the current CARB inventory. The estimated N_2O emissions drop to 1.3 - 2.3 times the CARB inventory if corrected for the median N_2O emissions assuming the 10% model bias in CO is applicable to N_2O. This study's results reinforce the understanding that a large portion of the increase in global atmospheric N_2O can be attributed to the use of fertilizer, and agricultural activities are likely a significant source of anthropogenic N_2O emissions in California, as currently reflected in CARB's N_2O inventory. The results also indicate that seasonal variations in California's N_2O emissions relative to the annual average are likely smaller than for interior portions (e.g., Midwestern US) of the continental US, consistent with milder climate of California.

In summary, while the ffCO_2 emissions, which account for the majority of the total GHG emission in California, are not clearly distinguishable from the state inventory in central and southern California, CH_4 and N_2O emissions appear to be higher than current inventory estimates.

EXECUTIVE SUMMARY

Background

California has committed to an ambitious plan to reduce greenhouse gas (GHG) emissions to 1990 levels by 2020 through Assembly Bill 32 (AB-32), which requires accurate accounting of emissions for effective mitigation planning and verification of future emission reductions. This has prompted effort by the California Air Resources Board (CARB) and others to measure, quantify, and mitigate emissions of key GHGs. The state official GHG inventory reports that California currently emits a total of 459.3 Tg (1 Tg = 10^{12} g) CO_2 equivalent anthropogenic GHGs in 2013, with approximately 84% as carbon dioxide (CO_2), 9% as methane (CH_4), 3% as nitrous oxide (N_2O), and the remaining 4% as high global warming potential (High-GWP) GHGs [CARB, 2015]. While fossil fuel CO_2 emissions can be estimated from fuel sales and distributed using comparatively well-known activity data, previous studies (e.g., Hsu et al. [2009]; Wennberg et al. [2012]; Peischl et al. [2013]; Jeong et al. [2012b, 2013, 2014]) suggest that non-CO_2 GHG emissions from California are less certain, largely due to an incomplete understanding of emission processes for California's diverse emission sources.

Atmospheric GHG measurements from networks of towers, when combined with inverse model estimation techniques have the potential to accurately quantify current GHG emissions. Atmospheric inverse methods, which estimate the GHG emissions from in-situ (i.e., instrumentation located directly at the site and in contact with the air) and/or remotely sensed GHG mixing ratio measurements and modeled meteorology, can provide an independent test of GHG emission inventory and have been widely applied at both global and regional scales. In general, the components of atmospheric inverse emission estimates are GHG mixing ratio measurements, an atmospheric transport model (including chemistry for global simulations), in some cases prior estimates for GHG emissions and sinks or their spatial and temporal correlation structure, and a statistical technique to minimize differences between measured and predicted GHG mixing ratios. This research project constitutes a focused effort to rigorously evaluate the current annual statewide GHG inventories of selected anthropogenic non-CO_2 GHG (e.g., CH_4 and N_2O), and fossil fuel CO_2 emissions together with a measurement and modeling system capable of continuing those estimates into the future.

Objectives and Methods

The primary objectives of this study are to expand and employ atmospheric measurements to conduct robust and reliable estimation of anthropogenic GHG emissions in California over a complete annual cycle. To address these objectives, we expanded multi-site and multi-year atmospheric measurements in a collaborative GHG tower measurement network (a total of 13 sites) that includes six CARB monitoring stations and then quantified in-state $ffCO_2$, CH_4 and N_2O emissions for regions (i.e., air basins) of California with an atmospheric inverse model.

Fossil fuel CO_2 ($ffCO_2$), CH_4, N_2O, and CO (used for transport evaluation) measurements were made at a collaborative GHG network across California, primarily by the CARB Greenhouse Gas Research Monitoring Network. This research contract expanded the statewide monitoring effort by adding two important measurement stations: (1) the researchers continued existing semi-continuous in-situ measurements of CO_2, CO and CH_4 at three heights (30, 91, and 483 m above ground level, AGL) at Walnut Grove, CA, and continued flask sampling for the National Oceanic and Atmospheric Administration (NOAA), and (2) the researchers also established new GHG measurements at a tower site in San Bernardino, CA. The combined network conducted GHG measurements for $ffCO_2$ (from 3 sites), CH_4, (13 sites) and N_2O (6 sites) as well as CO measurements (5 sites; one coastal site in the San Francisco Bay Area (SFBA) is used only for background evaluation, not for comparison with predictions), significantly increasing its network density. In particular, the expanded GHG network is now likely to be effective in constraining CH_4 and N_2O emissions from California's major urban and rural regions, and provided (albeit limited) spatial coverage for $ffCO_2$ emissions in both central and southern California.

The inverse model adjusts spatially resolved prior estimates (i.e., the estimate based on existing knowledge before measured data are taken into account) of GHG emissions to provide a best match between the tower measurements and model predictions, which are computed using the prior emissions and an atmospheric transport model. Central to the inverse model approach, uncertainties in the GHG measurements, prior emissions model, and atmospheric transport are evaluated. In general, the network measurements are made with carefully calibrated instruments that provide sufficient precision, and accuracy measurement uncertainty is small compared to uncertainty generated by the transport model.

Of particular relevance to the current study, we have been active in developing and applying inverse methods to estimation of CH_4 emissions. In 2007, we started the California Energy Commission (CEC)-supported California Greenhouse Gas Emissions Measurement (CALGEM) project on CH_4 and other non-CO_2 GHG emissions, and in 2010, we began an inverse modeling project with CARB to estimate CH_4 emissions using data from new GHG measurement sites established by CARB. Building on our previous work, we employ the Weather Research and Forecasting and Stochastic Time-Inverted Lagrangian Transport (WRF-STILT) transport model, an atmospheric transport model widely used for various GHG applications. We identify transport model configurations that minimize systematic bias in critical transport variables (e.g., wind velocity, and turbulence) for different regions of California and then assess random uncertainty in transport using a combination of meteorological and CO measurements coupled with the gridded CARB CO emission inventory in the same manner applied for the GHGs.

Using the optimized transport model configurations for different regions of California, we then calculate predicted local GHG mixing ratio signals based on spatially resolved emission models for $ffCO_2$, CH_4 and N_2O, together with inflow boundary conditions (i.e., concentrations at the modeling domain boundary) from NOAA. The Bayesian inversion then estimates posterior (i.e., results after the relevant atmospheric observation is taken into account) emissions by comparing predictions with measurements and reducing the difference in the two quantities. In this study, the inverse modeling expands on the approach taken in Zhao et al. [2009] and Jeong et al. [2012a, 2012b, 2013]. In particular, to estimate CH_4 and N_2O emissions this study employs a hierarchical Bayesian inversion method which improves upon earlier work (which only estimated the posterior emission uncertainties; e.g., Jeong et al. [2013], Wecht et al. [2014]) by estimating not only posterior emissions, but also uncertainties for the prior emissions, the model-measurement differences, and the posterior emission estimates.

Results

This study has made a significant improvement beyond previous measurement work of GHGs in a network including major urban areas of Sacramento, the San Francisco Bay Area (SFBA), the South Coast Air Basin (SoCAB), and the Central Valley of California. In addition, the meteorological variables measurements critical for transport (winds and boundary layer depth) were obtained from radar wind profilers, balloon radiosondes, a doppler wind-lidar in San Jose, and numerous surface wind measurement stations.

Mesoscale meteorological models, such as WRF, are widely used to derive spatially continuous meteorological parameters at various temporal scales. In this study, the meteorological model development was driven by comparison between the WRF simulations and meteorological measurements. Comparisons of the optimized meteorological predictions from across California show that the seasonal mean biases in boundary layer wind speed (< ~0.5 m s^{-1}), wind direction (< ~15°), and boundary layer height (< ~200m) are not statistically significant compared to the random variation in these variables for most sites in most seasons. Complementing the direct meteorological evaluation, the WRF-STILT predictions of CO generally compare favorably with CO measured at four towers (two in the Central Valley and two in SoCAB during June 2013 – May 2014 period), yielding near-unity slopes (predicted vs. measured) for the majority of sites and seasons, with typical random errors for individual 3-hr averages ranging from 35% to 85% of the mean seasonal CO signals at the different sites. Averaging the slopes of WRF-STILT predictions relative to CO measurements over all sites and seasons, we find that the annual state-total CO signal is captured for the major regions of California to within 10% ± 10% at 95% confidence, noting that some part of the mean difference and variation may be due to errors in the spatial and temporal distribution of the CO emission model. In lieu of quantitative uncertainty estimates for the CO emission model, we then proceed to evaluate emissions of the GHGs under the conservative assumption that all errors can be attributed to the transport model.

In addition to the main GHG species, air samples from Walnut Grove has been analyzed for radiocarbon $^{14}CO_2$ which serves as an essential tracer of fossil fuel CO_2 added locally to the atmosphere. Using multi-year (2009 – 2012) observations of fossil fuel CO_2 derived from radiocarbon $^{14}CO_2$ measurements from samples collected at a central California site and the classical Bayesian inversion (with prescribed uncertainties), we estimate $ffCO_2$ emissions from central California are within 6% ± 20% (95% confidence level (CL)) of the prior estimate for that region and period. For a shorter period from June 2013 - May 2014, radiocarbon analysis for SoCAB suggests that $ffCO_2$ emissions are within 11% ± 20% of the prior estimate for that region. Combining results from the two regions and including transport model results above that showed a 10% ± 10% low bias, we conclude actual $ffCO_2$ emissions are essentially consistent with the CARB's prior statewide inventory estimates.

Using CH_4 measurements from 13 sites across California during June 2013 – May 2014, hierarchical Bayesian inversion suggests that state annual anthropogenic CH_4 emissions (2.42 ± 0.49 Tg CH_4/yr (95% CL including transport bias uncertainty; 1 Tg = 10^{12} g), higher (1.2 - 1.8 times) than the anthropogenic emission in CARB's current inventory (1.64 Tg CH_4/yr in 2013). We note that the estimated CH_4 emissions drop to 1.0 - 1.6 times the CARB inventory if we correct for the median CH_4 emissions assuming the 10% bias in the CO result above is applicable to CH_4. The CH_4 emissions from the Central Valley and urban regions (San Francisco Bay Area and SoCAB) account for ~ 58 and 26 % of the total posterior emissions, respectively. This study and other studies (e.g., analysis from volatile organic compound (VOC) measurements) suggest the livestock sector is likely the major contributor to the state total CH_4 emissions, in agreement with CARB's GHG inventory.

Finally, using N_2O measurements from six sites across California during the same period, hierarchical Bayesian inversion estimates state annual anthropogenic N_2O emissions to be 87± 22 Gg N_2O/yr (95% CL including transport bias uncertainty; 1 Gg = 10^9 g), higher (1.5 – 2.5 times) than the current CARB inventory (44 Gg N_2O/yr in 2013). As in CH_4, we note that the estimated N_2O emissions drop to 1.3 - 2.3 times the CARB inventory if we correct for the 10% median N_2O emissions assuming the bias in CO is applicable to N_2O. Results of this study reinforce the understanding that a large portion of the increase in global atmospheric N_2O can be attributed to the use of fertilizers, and agricultural activities are likely a significant source of anthropogenic N_2O emissions in California, as currently reflected in CARB's N_2O inventory. The results also indicate that seasonal variations in California's N_2O emissions relative to the annual average are likely smaller than for interior portions of the continental US, consistent with milder climate of California.

Conclusions and Recommendations

This project has not only implemented additional GHG measurements but also more critically, brought together a collaborative network of measurement sites that collectively provide the most comprehensive picture of atmospheric GHG measurements currently available for California. Utilizing those measurements, an inverse model approach was improved and applied to estimate GHG emissions from the majority of emitting regions in California. The research suggests that while fossil fuel CO_2 emissions, which accounts for the majority of the total GHG emission in California, are in close agreement with the statewide CO_2 inventory in central and southern California, the statewide inventory marginally underestimates CH_4 and N_2O emissions, with the majority of those emissions centered in the Central Valley. After correcting for a possible transport model bias, the median value of the inverse model results, this study suggests that the combined total of CH_4 and N_2O emissions from the inverse analysis would comprise ~17% of state total GHG emissions, which is larger than 12% estimated in the current state inventory, given the uncertainties.

Several areas of research are needed to improve estimation of GHG emissions for the purpose of inventory evaluation in California. First, bottom-up inventory methods could be expanded to include a first order uncertainty analysis as performed by the US Environmental Protection Agency (EPA) at the national scale [US-EPA, 2015]. In addition, comparison of bottom-up and top-down methods benefits from spatiotemporally disaggregated models for GHG emissions inventory. While this current study has employed either the CALGEM CH_4 maps from Lawrence Berkeley National Lab (LBNL) or the Emissions Database for Global Atmospheric Research (EDGAR) maps for N_2O, it would be extremely valuable for CARB to develop spatiotemporally explicit maps of the same sort (e.g., CO) that have been developed for air quality control.

Second, while CARB has made great strides to implement a GHG measurement network in selected regions of California, additional work to collaborate with and support more sites in the key areas (e.g., SoCAB, SFBA) would greatly improve the spatial coverage of the measurements and hence ability to infer emissions. As part of this effort, additional focus on key transport variables, wind profiles and boundary layer mixing height, would be of high value for refining and evaluating the transport model used for the GHG mixing ratio prediction.

Finally, additional work needs to be performed to improve and evaluate the atmospheric transport models used for the mixing ratio prediction. This effort should continue to include and expand the use of both meteorological and multi-gas data to form a more comprehensive understanding of regionally- and seasonally-specific transport model uncertainties. From the perspective of GHG inventory evaluation, the goal of these combined efforts should result in a quantitative expression of the probability that California is meeting the legislated GHG emission reduction targets.

PROJECT REPORT

1. Introduction

California has committed to an ambitious plan to reduce greenhouse gas (GHG) emissions to 1990 levels by 2020 through Assembly Bill 32 (AB-32), which requires accurate accounting of emissions for effective mitigation planning and verification of future emission reductions. This has led to efforts to measure, quantify, and mitigate emissions of a variety of key GHGs. The state official GHG inventory reports that California currently emits a total of 459.3 Tg (1 Tg = 10^{12} g) CO_2 equivalent GHGs in 2013 [California Air Resources Board (CARB), 2015]. However, as shown in previous studies (e.g., Jeong et al. [2012b, 2013, 2014]) emissions in California are uncertain due to lack of activity data and incomplete understanding of emission processes, complicated by California's diverse emission sources, complex topography and weather patterns (e.g., land-sea breeze).

A variety of methods have been applied to address the problem of accurately quantifying emissions of GHGs in California. For fossil fuel CO_2, there have been few estimates of state level emissions over full annual time scales. Although the bottom-up approach can be limited by incomplete knowledge of processes that contribute to fossil fuel CO_2 emissions, the State of California estimates emissions using bottom up activity data including fuel sales and other data to assess the local to regional to statewide emissions of fossil fuel CO_2 [CARB, 2015]. Newman et al. [2013] showed that fossil fuel combustion contributed up to ~100 % of the enhancement near midday in the Los Angeles megacity during May – June 2010 and the Vulcan fossil fuel CO_2 (ffCO_2) inventory [Gurney et al., 2009] is roughly consistent with the measurements.

Several recent studies have estimated CH_4 emissions in different regions of California using measurements from ground towers, aircrafts, and satellites. Zhao et al. [2009] and Jeong et al. [2012a, 2013] estimated CH_4 emissions using towers in the Central Valley. In particular, Jeong et al. [2013] conducted the first multi-site analysis of CH_4 emissions in California based on measurements from five ground sites and across seasons (ten months during 2010 - 2011), and estimated a state total of 2.03 – 2.71 Tg CH_4/yr. Wecht et al. [2014] used airborne measurements during the one-month California Research at the Nexus of Air Quality and Climate Change (CalNex) period (May – June 2010) and estimated a total of 2.65 – 3.07 Tg CH_4. At the sub-regional scale, most studies focused on the urban regions of southern California (e.g., Wunch et al. [2009]; Hsu et al. [2010]; Wennberg et al. [2012]; Peischl et al. [2013]). Also, there have been efforts to estimate statewide source-specific emissions. For example, Jeong et al. [2014] estimated statewide CH_4 emissions from petroleum production and the natural gas system, taking a unique approach of combining a bottom-up inventory with results from a field campaign.

While several studies have been conducted to estimate CH_4 emissions in California's rural and urban regions, only a few studies have attempted to estimate N_2O emissions with either temporally or spatially limited measurements. Jeong et al. [2012b] estimated

N_2O emissions in central California using two-year observations from a tall tower and showed actual N_2O emissions are significantly (> 2 times) higher than the state inventory. Xiang et al. [2013] reported the statewide emissions of N_2O during early summer (May – June 2010) were 3 – 4 times higher than the EDGAR (European Commission Joint Research Centre (JRC) and Netherlands Environmental Assessment Agency, Emission Database for Global Atmospheric Research, http://edgar.jrc.ec.europa.eu) inventory and other inventories (e.g., Global Emission Inventory Activity (GEIA), Bouwman et al. [1995]). When they scaled the estimated early summer emissions using the seasonality from the Midwestern region of US reported by Miller et al. [2012], the annual emissions were 1.0 – 1.7 times the 2009 CARB inventory.

Although there have been increased efforts to quantify GHG emissions, only few estimates of statewide emissions over full annual time scales that are necessary for evaluation of current state GHG inventories are available. A full annual analysis that allows for emission estimates for major urban and rural regions of California requires a dense network of measurements and a high resolution modeling approach due to the complexity of emission sources in California. This study builds on previous work (e.g., Jeong et al. [2012a; 2012b; 2013], Newman et al. [2013]) to quantify $ffCO_2$, CH_4, and N_2O emissions from California. This new effort includes a significant expansion of measurement sites, establishing a network of multiple tower sites for $ffCO_2$ (3 sites), CH_4 (13), and N_2O (6 sites) in California. In particular, we set up new measurement sites to constrain emissions in the southern California region that includes the San Bernardino County (SBC) site while continuing measurement activities in the Central Valley sites (e.g., Walnut Grove, WGC; Jeong et al. [2013]). In addition to expanding the measurement network for inverse modeling, in this study we assess the uncertainty in transport model predictions using a combination of meteorological and carbon monoxide (CO) measurements. CO has specific advantages that make it an ideal candidate to assess the accuracy of atmospheric inverse modeling and develop estimates of potential biases and errors in the modeling framework. For instance, total anthropogenic emissions of CO are tightly coupled to emissions from fuel combustion, which are inventoried by CARB. These advantageous properties lend themselves to bottom-up estimates of CO emissions with low uncertainty relative to bottom-up estimates of emissions for other GHGs.

Using atmospheric observations from multiple tower sites covering all major emitting regions of California, this study employs the hierarchical Bayesian inversion approach [Ganesan et al., 2014]. Using a hierarchical Bayesian method, this study illustrates how uncertainty in the inversion can be treated by a combination of our best a priori knowledge of error sources (e.g., transport error) and statistical inference, and how ground-based multi-tower measurements can be effectively used to constrain regional emissions. In Section 2, we describe the data and methods we used, including atmospheric measurements, prior emissions, transport modeling, and the hierarchical Bayesian inverse method. Section 3 presents results, including the inferred emissions from California for different regions and sources, and further discusses the results. In Section 4, we present conclusions, and recommendations for transport modeling, $ffCO_2$, CH_4 and N_2O emissions in California are made in Section 5.

2. Materials and Methods

2.1. Background on Inverse Modeling Framework

The inverse modeling framework employed in this multi-site study builds on the approach taken in Zhao et al. [2009] and Jeong et al. [2012a, 2012b, 2013]. The inverse modeling approach used in this study is illustrated in Figure 1. As shown in the figure, the Bayesian inverse model requires two direct inputs (two arrows are directed to the "Bayesian Inversion" box): 1) tower measurements (measured mixing ratios), and 2) predicted mixing ratios. Here we note that the chemical composition of the atmosphere is expressed as mixing ratio (also called the dry mole fraction), which is defined as the number of moles of a gas per mole of dry air, throughout the report. Mixing ratios of GHGs are usually given in units of parts per million volume (ppmv or ppm = 1×10^{-6} mol/mol), parts per billion volume (ppbv or ppb = 1×10^{-9} mol/mol), or parts per trillion volume (pptv or ppt = 1×10^{-12} mol/mol). By comparing measurements with predictions, the Bayesian inverse model estimates scaling factors for surface emissions (i.e., spatially/temporally resolved emission inventory) such that the scaled surface emissions yield predicted signals that are statistically consistent with measurements.

Predicted signals are calculated as a linear combination of 1) footprints, which represent the sensitivity of signals measured at different sites to emissions across the landscape (i.e., concentration change at the measurement site due to unit emission flux from each grid cell) and 2) surface emissions. In other words, predicted contributions to mixing ratios (i.e., concentration) from emissions within the modeling domain are calculated as **FE**, where **F** is footprint strength and **E** is the prior emissions. Footprints represent the sensitivity of the mixing ratio at the receptor location (i.e., measurement site) to surface sources, in units of ppb/(nmol m^{-2} s^{-1}) or ppm/(μmol m^{-2} s^{-1}). Note that we use units of ppm for CO_2 and ppb for the other gases due to the difference in the magnitude of the concentrations of those gases. Thus, the footprint provides information on how much the mixing ratio at the receptor location changes when the surface emission changes by one unit. As shown in Figure 1, footprints are calculated from particle trajectories simulated using the WRF-STILT model. The WRF-STILT model has been used to constrain GHG emissions in many studies including airborne measurement-based (e.g., Gerbig et al. [2003]; Kort et al. [2008]) and tower measurement-based inversions (e.g., Zhao et al. [2009]; Miller et al. [2013]; Jeong et al. [2012a; 2012b; 2013]).

Figure 2 shows particles moving from upwind locations to the measurement site (i.e., receptor) using the STILT model, which requires meteorological fields simulated by the WRF model. In the time-reverse sense, the STILT model transports ensembles (e.g., 500 particles) of particles (air parcels) backwards in time (e.g., 7 days) from a receptor point. The STILT model defines paths traveled by parcels of air, or trajectories, which are a basis for footprint estimates. By releasing particles backwards, we identify the origin of emission sources that contribute to the receptor. The identified contribution from each location (e.g., 10 km × 10 km grid cell) is combined to generate a map of the averaged (e.g., hourly) measurement sensitivity to emissions, or footprint. This footprint is then multiplied by the emissions (in flux units of nmol m^{-2} s^{-1} or µmol m^{-2} s^{-1}) to produce GHG mixing ratios (ppb or ppm) that account for upwind emission sources.

As shown in Figure 2, footprints are estimated by counting the time the particle spends in the surface-influenced region, defined as ½ of the planetary boundary layer height (PBLH), and inversely weighted by dilution into the height of the boundary layer. In Figure 2, the dark colored particles within ½ PBLH are assumed to contribute to the footprint, while particles colored in gray above ½ PBLH are not. The footprint for each grid cell (e.g., ~ 10 km × 10 km) is calculated by counting the number of particles that pass over the grid cell weighted by the amount of time the particles spend in the grid cell. Therefore, if more particles stay in a grid cell over a long period of time, the mixing ratio signal at the measurement site is more sensitive to the grid cell.

Because predicted mixing ratios represent local enhancements of emissions, upwind background mixing ratios entering the study domain are needed to compare predictions with measurements, which include both local and background mixing ratio signals. Boundary values are the initial mixing ratios that represent the upstream concentrations at the western domain boundary (130°W) and often called background concentrations.

The Bayesian inversion model optimizes a set of scaling factors, minimizing the difference between measurements and predictions given uncertainties in a priori emissions and model predictions. Uncertainties in modeling footprints due to errors in winds and planetary boundary layer (PBL) heights contribute to uncertainties in inversion results and confidence intervals associated with optimized emissions values. The result of the Bayesian inverse model is a set of optimized scaling factors for region or source emissions, which can be multiplied by a priori emissions to produce inferred (posterior) GHG emissions.

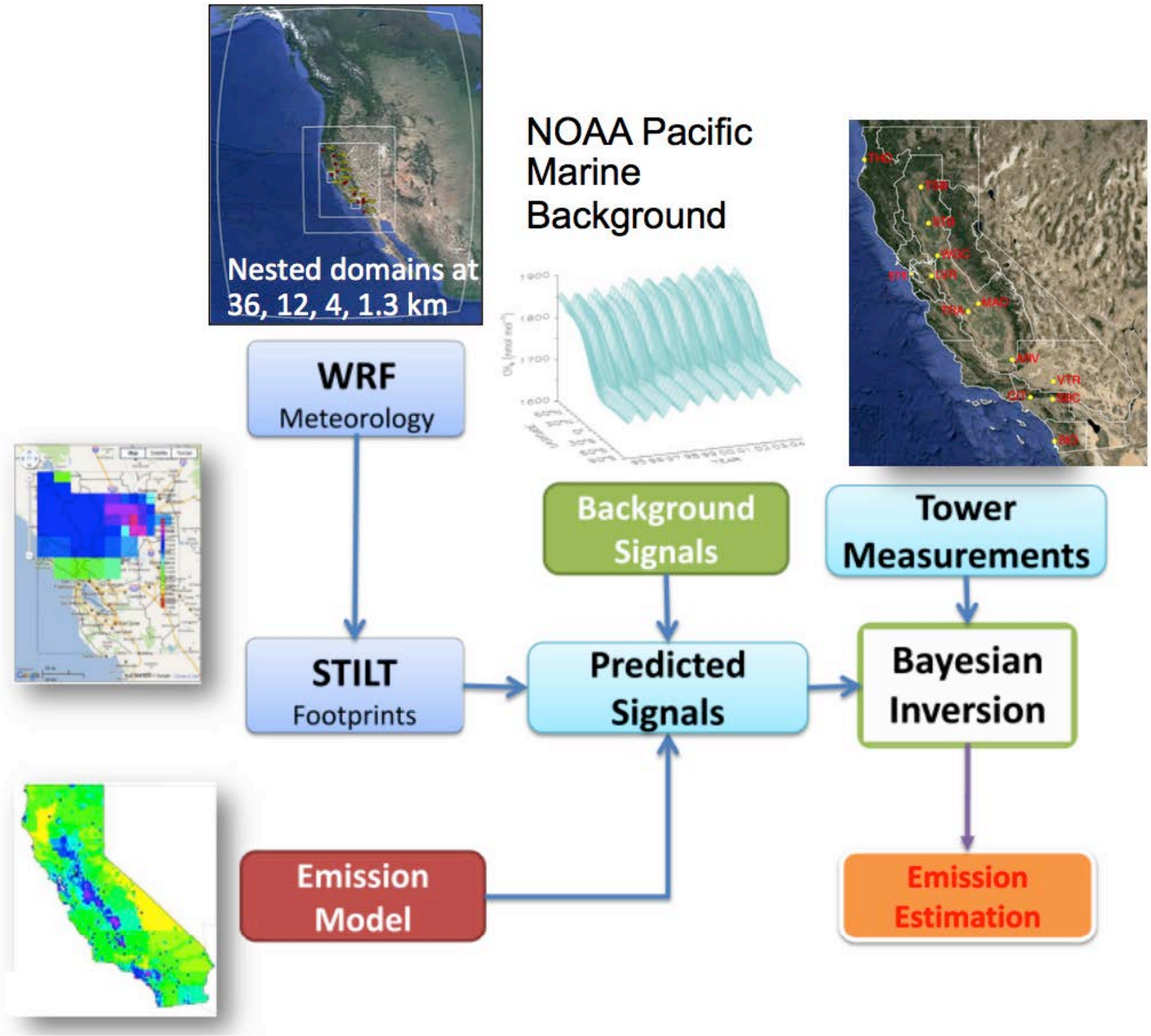

Figure 1. Inverse modeling approach used in the study.

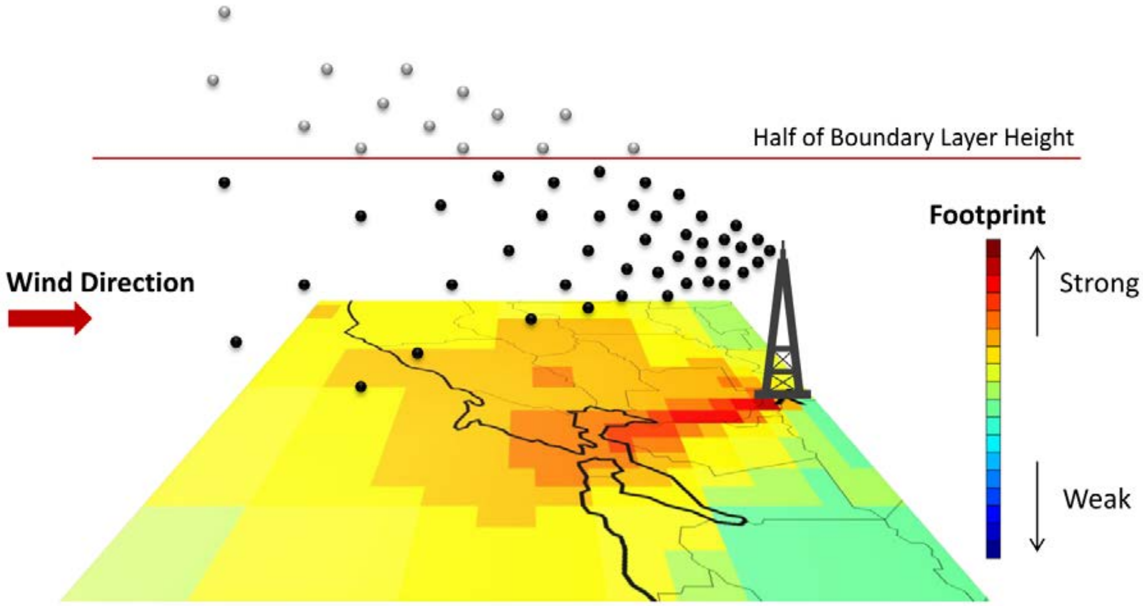

Figure 2. Schematic diagram showing simulations of backward (opposite to the wind direction) particle trajectories from a tower that are used for footprint calculations. Footprints at the grid cells near the receptor are strong because more particles pass over those grid cells before they are advected and dispersed into different places. The particles above ½ PBLH (colored in gray) do not contribute to the footprint strength.

2.2. Measurement Network

Fossil fuel CO_2 ($ffCO_2$), methane (CH_4), nitrous oxide (N_2O) and carbon monoxide (CO) measurements were made at a collaborative GHG network (a total of 13 sites) across California. Central to the collaborative GHG network, the CARB tower measurement network (six sites) provides a significant portion of measurements across California, covering both rural and urban major emitting regions. The measurement network is shown in Figure 3, and the site information is summarized in Table 1. The $ffCO_2$ mixing ratios were estimated from radiocarbon $^{14}CO_2$ measurements at a site (WGC) in central California during 2009 – 2012 and at two sites (CIT, SBC) in southern California during June 2013 – May 2014. CH_4 mixing ratios were measured at 13 sites during June 2013 – May 2014. Compared to the analysis presented by Jeong et al. [2013] where five sites in the Central Valley were used, four sites were added in southern California (CIT, SBC, SIO and VTR), two sites were added in the San Francisco Bay Area (SFBA; LVR and STR), and one site was added in the Sacramento Valley (TSB). For N_2O, a measurement network was commissioned to allow analysis greatly expanding on that described by Jeong et al. [2012b] where only WGC data were used. N_2O measurements were made from six sites during June 2013 – May 2014: ARV, CIT, SBC, STR, STB and WGC. Besides the major GHGs, CO mixing ratios were measured from 5 sites (ARV, CIT, SBC, STR and WGC; STR CO data are used only for background uncertainty evaluations, not for comparison with predictions) during June 2013 – May 2014 and were used to assess the uncertainty in WRF-STILT transport model predictions in combination with meteorological measurements. Information regarding CH_4 and CO_2 measurements at the Central Valley sites was presented in Jeong et al. [2012a, 2013] and Andrews et al. [2014]. Additional details on measurement methods implemented at WGC (N_2O) and SBC (CH_4, CO_2, CO, and N_2O, and radiocarbon) for this project are described in Sections 2.3 – 2.4 below.

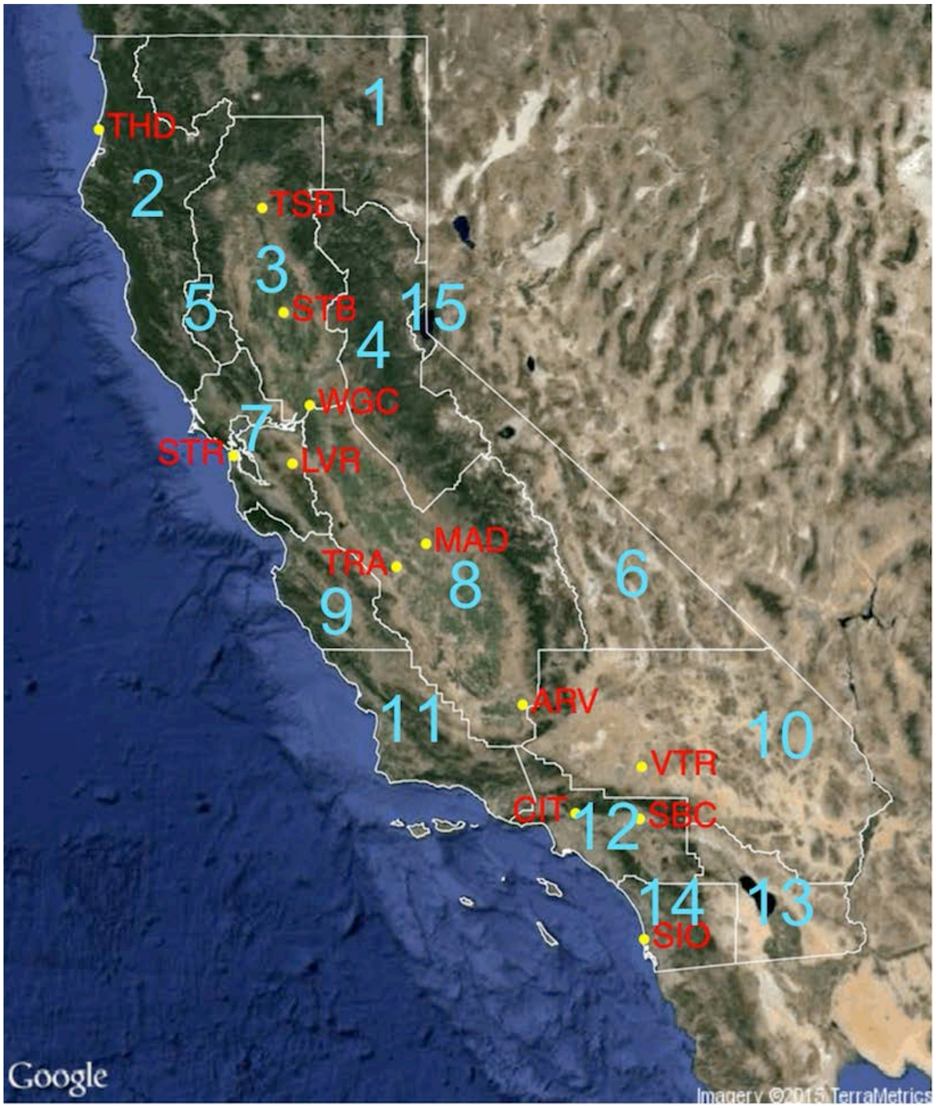

Figure 3. California GHG measurement network used in this study with California's Air Basins. For CH_4 analysis, all 13 sites were used. For $ffCO_2$, WGC, CIT and SBC were used. For N_2O, ARV, CIT, SBC, STR, STB and WGC data were used. The 1 – 15 regions correspond to California's air basins: Northeast Plateau (NEP, 1), North Coast (NC, 2), Sacramento Valley (SV, 3), Mountain Counties (MC, 4), Lake County (LC, 5), Great Basin Valleys (GBV, 6), San Francisco Bay Area (SF, 7), San Joaquin Valley (SJV, 8), North Central Coast (NCC, 9), Mojave Desert (MD, 10), South Central Coast (SCC, 11), South Coast (SC, 12), Salton Sea (SS, 13), San Diego (SD, 14) and Lake Tahoe (LT, 15), respectively.

Table 1. GHG Sites Information across California

Site	Location	Latitude	Longitude	Inlet Height (m, AGL)	Measurements Availability
ARV*	Arvin	35.24	-118.79	10	CH_4, N_2O, CO
CIT	Caltech, Pasadena	34.14	-118.12	10	$ffCO_2$, CH_4, N_2O, CO
LVR	Livermore	37.67	-121.71	27	CH_4
MAD*	Madera	36.87	-120.01	10	CH_4
STB*	Sutter Buttes	39.21	-121.82	10	CH_4, N_2O
STR	San Francisco	37.76	-122.45	232	CH_4, N_2O, $CO^\dagger$
THD	Trinidad Head	41.05	-124.15	20	CH_4
TRA*	Tranquility	36.63	-120.38	10	CH_4
TSB*	Tuscan Buttes	40.26	-122.09	10	CH_4
VTR	Victorville	34.61	-117.29	90	CH_4
WGC	Walnut Grove	38.27	-121.49	30, $91^\#$, 483	$ffCO_2$, CH_4, N_2O, CO
SBC*	San Bernardino	34.09	-117.31	27, $58^\#$	$ffCO_2$, CH_4, N_2O, CO
SIO	Scripps	32.87	-117.26	10	CH_4

*Indicates CARB's statewide GHG monitoring network sites.

$^\#$Inlet heights used in the inversion; AGL = above ground level

†STR CO data are used only for background uncertainty evaluations, not for comparison with predictions.

2.3. Measurement at WGC Tower

As one task in this project, we continued existing semi-continuous in-situ measurements of CO_2, CO, CH_4 at three heights (30, 91, and 483 m AGL) as described by Andrews et al. [2014], and continued flask sampling for the National Oceanic and Atmospheric Administration (NOAA). As a brief summary, air samples are drawn down from three heights on the tower by air pumps, pressurized to 10 psig (pounds per square inch gauge pressure), passed through 5 ºC water traps, and supplied to a valve manifold. Air exiting the manifold is directed to separate temperature controlled membrane (Nafion) driers (one for the CO_2 and CH_4, and a 2nd for CO), which maintain the sample air streams at near -30°C dew point. Output of the driers is directed to a set of gas analyzers (Picarro 1301, Picarro Inc., Sunnyvale, CA) for CO_2, and CH_4; a Licor 4000 (Licor Inc., Lincoln NB) for CO_2; and a Thermo-Electron 48TC for CO). Air samples are switched between the three levels on the tower every 300 s, and the last 120 seconds of each sample used for further analysis. These instruments are calibrated using standards supplied by NOAA. Performance of the system is described in detail in Andrews et al. [2014]. Flask samples are gathered from the 91 m level at 2200 UTC (Coordinated Universal Time) every other day and analyzed at NOAA for a suite of long-lived GHG (http://www.esrl.noaa.gov/gmd/ccgg/) including selected halocarbons (http://www.esrl.noaa.gov/gmd/hats/).

Supporting this project we also measured N_2O. Here, we used the existing preconditioned (5°C dew point, 10 psig) air streams from two of the three levels (91 and 483 m AGL). Air was multiplexed through a pressure controller (at 800 Torr) to a membrane drier (Nafion), which maintained the dew point near -20°C, and then supplied it to an ARB supplied off-axis Integrated Cavity Output Spectrometer (LGR Model 907-0015; Los

Gatos Research Inc., Los Gatos, CA). The multiplexer switched the sample air between the two heights on the tower every 400 s. Measurements were allowed to settle for 280 s, with only the last 120 s used for the measurement. The LGR instrument offset and gain were measured periodically and corrected using two methods. First, two working standards (tied to standards supplied by NOAA) were used to correct changes in gain and offset, while a third working standard was used to check the result. The offset and gain of the LGR instrument were measured every 3 hours with “high” and “low” working standards. The third “target” standard was used to check the calibration at times midway between the “high-low” calibrations. At WGC target check measurements showed root-mean-square (RMS) variations less than 0.1 ppb. In addition, we compared in-situ N_2O measurements with results from the periodic flask measurements, with the in-situ measurements interpolated to the time of the flask sample varied from ~ 0.3 - 0.5 ppb, consistent with the expected variation in flask measurements (www.esrl.noaa.gov/gmd/ccgg/flask.html).

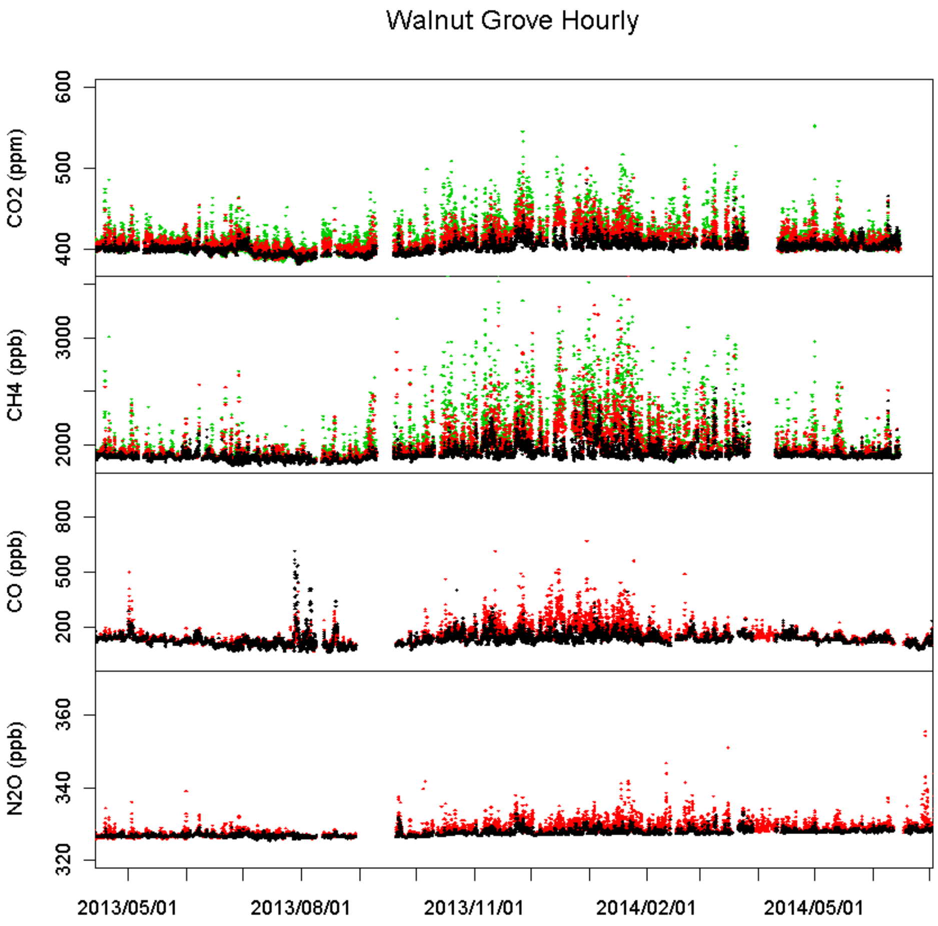

Figure 4. Hourly averaged measurements of CO_2, CH_4, CO, and N_2O at the Walnut Grove (WGC) tower at 30 (green), 91 (red), and 483 (black) m AGL for the June 2013 to June 2014 period. Periods with data gaps indicate when different subsystems or instrument required maintenance. In general, the highest measurements are observed at lowest level at night.

Measured dry-mole mixing ratios of CO_2, CH_4, CO, and N_2O are shown as a function of time during the June 2013 to May 2014 period in Figure 4. In general, measurements are higher at night when planetary boundary layers (PBL) are lower than during the day, trapping surface emissions. In particular, this effect is more pronounced in winter when PBL are lower than during the summer. These measurements are applied to inverse model analyses as described in the sections below.

2.4. Measurement at SBC Tower

As another task in this project, we also implemented GHG measurements at a new tower site in San Bernardino, CA (SBC). The system was substantially similar to that used at WGC with the following differences.

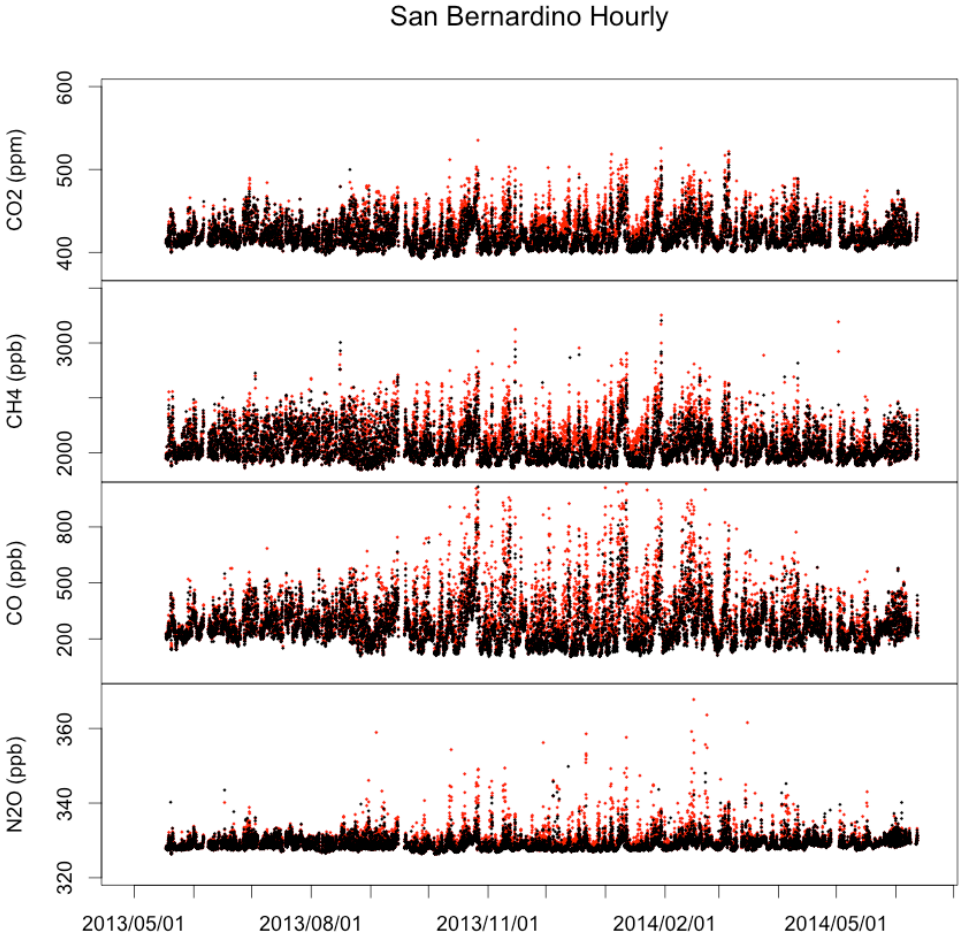

Figure 5. Hourly averaged measurements of CO_2, CH_4, CO, and N_2O at the San Bernardino (SBC) tower at 27 (red), 58 m (black) for the June 2013 to June 2014 period. In general, the higher measurements are observed at the lower level at night but because the levels are closely spaced compared with WGC, the effect is less evident. In addition the SBC tower is located in a more urbanized area relative to WGC, resulting in generally higher GHG enhancements.

Specific to the SBC tower, we implemented a complete rack of equipment that included pumps, water traps, multiport sampling value, a temperature and pressure controlled membrane drier that supplied air to a Picarro (G2301 CH_4/CO_2) and LGR (907-0015, N_2O/CO) analyzers, a data logger system and calibration gas standards. Here, the switching interval was set to 400 s, and the calibration interval was 4 hr. In addition, air samples were collected into flasks from the 58 m level on the tower at 2200 - 2300 UTC for subsequent $^{14}CO_2$ analysis at the University of California, Irvine (UCI).

Calibrated dry-mole mixing ratios of CO_2, CH_4, CO, and N_2O are shown as a function to time during the June 2013 to May 2014 period in Figure 5. Similar to WGC, higher mixing ratios are observed at the lower level (27 m) than the higher level (58 m) at night, but because the levels are closely spaced compared with WGC, the effect is less evident. In addition the SBC tower is located in a more urbanized area relative to WGC, resulting in generally higher GHG enhancements. We also noticed that winds from the east in fall and winter sometimes coincided with large mixing ratio enhancements, particularly at low wind speeds. This is discussed in the following section on atmospheric transport modeling.

2.5. Data and Method for Transport Model Assessment

2.5.1. CO and Meteorological Observation Sites

The uncertainty in the WRF-STILT transport model predictions is evaluated using a combination of meteorological and carbon monoxide (CO) measurements. Mixing ratio measurements of CO were available during June 2013 to May 2014 at the CIT, SBC, and WGC and STR sites, and October 2013-May 2014 for ARV (Figure 6b). Note that the STR data are used only for background (i.e., upstream boundary conditions) evaluation and not used for comparison with model predictions. The CO measurements are made using sampling and analysis systems that combine pumps, membrane (Nafion) air driers, and gas analyzers following methods described by Andrews et al. [2014] for WGC, or adapted for use at the other sites (SBC, CIT, ARV). In particular, while WGC employed a gas correlation spectrometer (Thermo Electron TE48-TC), the SBC, CIT, and ARV sites employed off-axis Integrated Cavity Output Spectroscopy (ICOS) (LGR Model 907-0015; Los Gatos Research Inc., CA). In addition, air handling and calibration methods differed across the sites. At two sites (WGC and SBC), air sampling is switched between the multiple heights (WGC: 30, 91, 483 m AGL, every 300 s; SBC: 27 and 58 m AGL, every 400 s) with measurements allowed to settle, and the last 120 seconds of each cycle used to quantify CO mixing ratios of the ambient air. For the analysis described below, we applied the 91m (WGC), and 58m (SBC) measurements for measurement model comparison. For the other sites, measurements were made from single heights on those towers and switching was only applied for calibration.

The instrument offset and gain were measured periodically and corrected using different methods. At WGC, three NOAA primary standards were applied every six hours with separate target check measurements [Andrews et al., 2014]. At SBC, the calibrations used three secondary gas standards tied to NOAA primary standards, with the offset and gain of the LGR instrument measured four hours using the “high and low” secondary standards and then checked with the third “target” standard at times midway between the “high-low” calibrations. At CIT, offset and gain were calibrated every three months using NOAA primaries and offset was calibrated using a secondary standard every 4.5 hours and checked for consistency using every other measurement. For the other two in-situ sites (ARV and STB), a “precision check” was performed every 23 hours using an un-calibrated secondary gas cylinder. For two sites (WGC and STR), CO was also measured in flask samples collected at 2200 GMT (1400 PST) and analyzed by NOAA’s cooperative air sampling network. For SBC and CIT, target check measurements typically showed root-mean-square (RMS) variations less than 1 ppb. For sites with infrequent (23-hour) precision checks (ARV) which do not facilitate correction of diurnal variations in instrument offset due to temperature, the residual observed RMS variation was ~ 3 ppb, depending on the time period.

For this study, we used observations from four radiosonde locations, seven radar wind profiler stations, and a doppler-wind lidar (at San Jose State University) to assess WRF meteorology and generate error statistics for propagation in STILT. These observations were chosen since they are capable of sampling both planetary boundary layer winds and heights. Additionally, wind measurements from surface stations across California and several GHG towers were used to test local WRF meteorology and filter analysis periods as described below. The locations of these measurements are shown in Figure 6a.

When available, wind profiler observations from July 2013 - May 2014 were used to assess errors in boundary layer height (z_i) and planetary boundary layer (PBL) winds. These observations sampled winds throughout the boundary layer at an hourly time step. Estimates of daytime z_i were derived using a combination of automated algorithms and qualitative analysis from wind velocity observations of subhourly vertical velocity and returned signal strength [Wyngaard and LeMone, 1980; Bianco and Wilczak, 2002; Bianco et al., 2008]. This was a manually intensive exercise that required subjective expert judgment. As such, availability of wind profiler z_i data were limited relative to wind data, which were derived using an established automated algorithm. Additionally, the availability of wind profiler boundary layer height observations was restricted to periods when a clear convective boundary layer exists.

The wind profiler network in California has been in a continual state of flux, with profilers only operating for limited periods of time or experiencing extended periods of downtime. In order to retain spatial coverage of profiler observations across California we accounted for wind profiler sites that were not operating from June 2013 – May 2014, or were missing months during that period, by filling in monthly data gaps with observations from prior years and prior corresponding WRF simulations from Jeong et al. [2012a; 2013]. We assumed that monthly random error statistics were approximately invariant across years, but note this can be a potential source of error for assessing meteorological uncertainty in GHG predictions. In order to focus on winds within the PBL, we limited our analysis of profiler winds to those observations that were below 2000 m AGL. Finally, we removed outliers in PBL winds and z_i by identifying those observations that were greater than three standard deviations from the mean daytime values.

At radiosonde sites within California observations were generally taken either one or two times a day. These observations extended throughout the troposphere, but as with wind profiler measurements above we limited our analysis of wind speed and direction to the portion of observations below 2000 m. This is because the monthly-averaged diurnal convective boundary layer depths are lower than 2000 m in California [Bianco et al., 2011].

In addition to the meteorological measurements described above that sampled the entire PBL, observations of surface wind speed and direction were extracted from the Integrated Surface Database (ISD; [Smith et al., 2011]), California Irrigation Management Information System (CIMIS; http://www.cimis.water.ca.gov/), and Bay Area Air Quality Management District databases (BAAQMD; http://www.baaqmd.gov/). Although these measurements were limited to only winds near the surface, they provided excellent temporal and spatial coverage across California, with hourly observations available at most sites (Figure 6a).

One element of uncertainty was determining the portion of the model-observation error that should be assigned to observational inaccuracy. For the purposes of this study, we assumed the magnitude of observational uncertainty for wind measurements to be $1\ \mathrm{m\ s^{-1}}$ [Strach et al., 1987], the uncertainty of z_i measurements to be 200 m [Dye et al., 1995], and the uncertainty of CO measurements to be 3ppb [Andrews et al., 2014].

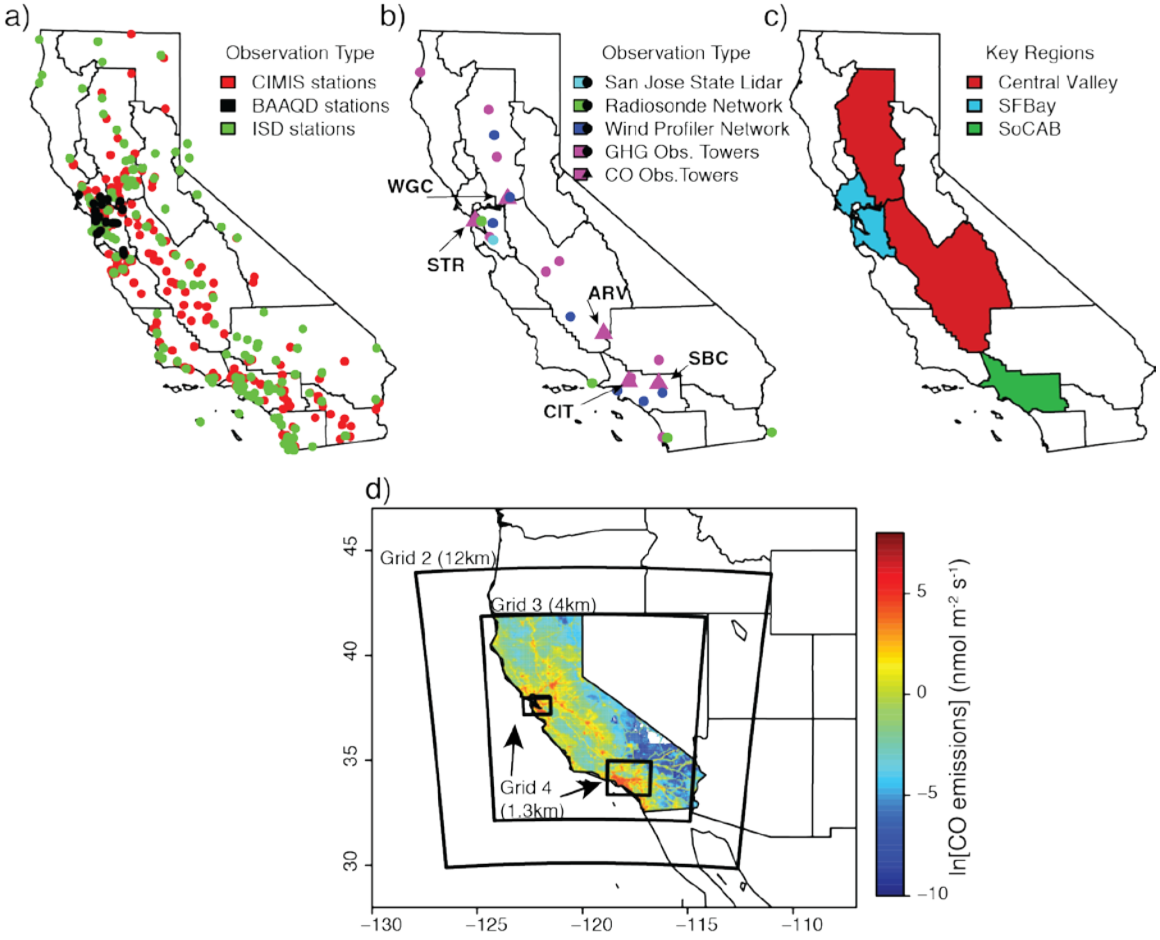

Figure 6. (a) Locations of surface wind observations, (b) locations of tower observations (purple), radiosondes (green), and wind profilers (blue), (c) key emitting regions, and (d) annual mean CO emissions (log scale) used in this study along with computational domains for the WRF-STILT model. The entire outer 36 km grid (not shown) extends from ~150°W - 90°W and ~17°N - 63°N.

2.5.2. Prior Emission Model and Background Atmospheric CO Mixing Ratios

To calculate model predictions of CO at the observational sites, a priori estimates of surface emission rates of CO and atmospheric background mixing ratios of CO are required. In this study we used hourly data provided by CARB and the Emission Database for Global Atmospheric Research (EDGAR, European Commission Joint

Research Centre (JRC) and Netherlands Environmental Assessment Agency, release version 4.2, http://edgar.jrc.ec.europa.eu; accessed in January 2015; hereafter EDGAR). The CARB data were provided hourly for 2012 with high spatial resolution (~4 km × 4 km) and cover the entire region of California and its coastal waters, while EDGAR provided annual mean CO emission data for 2008 with global coverage at ~10 km resolution. Since urban CO emissions in California vary between weekdays and weekends we retained these variations for the June 2013 – May 2014 period of interest using the 2012 CARB data and a simple selection process. For each month from June 2013 – May 2014 we constructed a pseudo-timeseries of California emissions by first determining the day of the week each day falls on. Then, if the day was Monday-Friday we selected a random weekday from the corresponding month in 2012 to represent it. Likewise, if the day was Saturday or Sunday we selected a random weekend day from the corresponding month in 2012. Repeating this for all months from June 2013 – May 2014 ensured that all weekday emission estimates corresponded to weekday emissions in the original 2012 data, and similar for weekends.

The annual mean map of prior emission estimates for California is shown in Figure 6d. Major metropolitan areas and highways are clearly evident. Outside of California emissions were set to values from the EDGAR dataset (~10 km resolution) which were interpolated to ~4 km resolution. This interpolation was done using a nearest-neighbor approach to retain sharp gradients that exist in the dataset.

In a recent study focused on the Los Angeles Basin, Brioude et al. [2013] compared top-down inversion estimates of CO emissions from an intensive aircraft campaign with earlier bottom-up CARB estimates of surface emission rates for SoCAB. They found that CARB estimates were accurate to ~15% relative to their top-down estimates, with biases dependent on differences between weekday and weekend emissions. Based on this we make the assumption that the a priori emissions within each footprint calculation have a 15% uncertainty associated with them. This is likely a conservative assumption given the high accuracy to which CO emissions are known in Los Angeles relative to other portions of the state due to its importance for assessing air quality in the region.

2.5.3. WRF-STILT Transport Error Analysis

In the WRF-STILT model, Eulerian fields from WRF are used to drive Lagrangian particle transport in STILT. For this study we used a series of two-way nested grids in WRF to improve simulation accuracy in key regions of California (Figures 6c, 6d). The horizontal resolutions of these grids were 36, 12, 4, and 1.3 km respectively. The outer 36-km grid simulated a region that included much of the western part of North America and the Northeast Pacific Ocean (not shown; grid extended from ~150°W - 90°W and ~17°N - 63°N). The 4-km grid encompassed the majority of California, and two 1.3-km grids were centered on regions surrounding SFBA and the metropolitan area of Los Angeles (including SoCAB) to improve simulation accuracy in these key regions (Figures 6c, 6d).

Version 3.5.1 of the WRF model was used for all simulations. The boundary and initial conditions were extracted from the North American Regional Reanalysis data set (NARR; [Mesinger et al., 2006]). The primary WRF simulations were run from June 2013 – May 2014 using a series of 30-h runs that covered the entire simulation period. For each of the 30-h runs, data from the initial 6 hours were considered to be spin-up and were discarded in the final analysis [Pillai et al., 2011; Jeong et al., 2013]. The remaining data was saved hourly.

Due in part to extensive topography generating unique meteorological conditions in California, there have been multiple studies in recent years that have assessed the ability of a variety of WRF parameterizations to reproduce observed conditions in the region [Bao et al., 2008; Michelson and Bao, 2008; Angevine et al., 2012; Jeong et al., 2012a; 2012b; 2013]. Here we largely follow the WRF setup described in Jeong et al. [2013]. We parameterized WRF to use 50 vertical levels to minimize errors in boundary layer meteorology over California's complex terrain. Radiative transfer used the RRTM scheme for longwave radiation, and the Goddard scheme for shortwave. The Purdue-Lin parameterization was used for microphysics, and the Grell-Devenyi ensemble mass flux scheme for convection. Finally, as described in more detail below, we tested several combinations of parameterizations for the land surface and planetary boundary layer. For the land surface scheme, we used both the five-layer thermal diffusion (5-L LSM, Ruiz et al. [2010]) and unified Noah (NOAH, Chen and Dudhia [2001]) models. We used the Mellor–Yamada Nakanishi Niino Level 2.5 (MYNN2, Nakanishi and Niino [2006]) and Yonsei University (YSU, Hong et al. [2006]) parameterizations for boundary layer physics. The YSU parameterization was selected to use an improved representation of topographic influences on boundary layer meteorology enabled [Jiménez and Dudhia, 2012].

In this study, each day at each site 500 particles were initialized hourly from 1900 - 0300 UTC (1100 - 1900 LST) in WRF-STILT. Following the work of Jeong et al. [2012a] the trajectories of these particles were calculated and tracked backward in time using WRF-STILT until either the particles were transported outside the computational domain or seven days had passed. For each time step when the trajectory of a given particle remained within the domain and within the atmospheric boundary layer, the time the particle spent over a given location and the local boundary layer height was calculated. By aggregating this information for all particles, footprints were calculated [Lin et al., 2003] (see Section 2.1 for footprint calculation). During each hour that particles were released, the footprint strength at each grid point was combined with a priori estimates of surface CO emissions to predict local (without the addition of background CO) CO mixing ratios at observational locations due to emissions within the computational domain.

In addition to providing time for particles to move away from observational locations and sample remote regions, tracking the particles for up to seven days provided sufficient time for a significant fraction of them to reach 130°W where they were assigned an observationally-based CO mixing ratio representing the background mixing ratio of CO for each particle. Following Jeong et al. [2013], a temporally and spatially varying mixing ratio "curtain" of CO was estimated at 130°W using vertical profiles of CO mixing ratios from aircraft along the West Coast US and Hawaii, as well as marine boundary layer data from the Cooperative Air Sampling Network (http://www.esrl.noaa.gov/gmd/ccgg/flask.html). For background observations along the West Coast, particle trajectories were tracked backward in time to 130°W where they were binned by latitude (10° resolution) and altitude between 3000 – 7000 m (1000 m resolution). Below 1000 m, time and space-varying values for the Pacific Ocean from the Cooperative Air Sampling Network were used. Bins between 1000 – 3000 m were calculated by vertical interpolation. Finally, the background CO signal was estimated for each time step by taking the mean background value across all particles. The background CO was added to the local mixing ratio calculated using footprints and prior emissions estimates to predict the total CO at each observational site for each hour from 1900 - 0300 UTC.

Biases and errors in the WRF representation of atmospheric properties can lead to transport errors in the STILT prediction of CO at observational sites. Note that in the coupled WRF-STILT model, STILT is driven by WRF-simulated meteorology. If these errors are under-diagnosed and not accounted for, they can contribute to unrealistic posterior estimates of surface emissions from atmospheric inversions with unrepresentative uncertainty estimates. Two WRF variables that were of particular importance to our application of the coupled WRF-STILT model included z_i [Gerbig et al., 2008], and winds within the PBL [Lin and Gerbig, 2005]. The PBL winds influence both the path that STILT calculates Lagrangian particles take and the fraction of a particle's final CO contributed by a given grid point. The fraction is directly proportional to the length of time a particle spends in the PBL over a given grid point (i.e. horizontal wind speed). Finally, z_i is inversely proportional to the atmospheric mixing ratio of boundary layer CO due to underlying surface emissions, and thus the CO mixing ratio that Lagrangian particles in the PBL incorporate.

Due to the importance of z_i and PBL winds, errors in WRF's representation of these fields must be accounted for in the Lagrangian transport model. WRF-STILT has been constructed to account for transport errors in the U and V components of PBL winds by assuming that WRF wind errors have insignificant mean error and can be represented by a Gaussian centered at zero with standard deviation equal to the standard deviation of WRF error relative to observations (σ_u, i.e., σ_u = sd (WRF – observation); sd = standard deviation) [Lin and Gerbig, 2005].

Previously, errors were assimilated into the STILT framework by adding an error component (ε) that is representative of PBL wind uncertainty:

$$\mathbf{u} = \overline{\mathbf{u}} + \mathbf{u'} + \varepsilon \qquad (1)$$

where $\mathbf{u}$ is the overall particle velocity vector, $\overline{\mathbf{u}}$ is the mean component, and $\mathbf{u'}$ is the turbulent component of particle velocity. ε was drawn from a Gaussian distribution with mean 0 and standard deviation equal to the observed standard deviation of boundary layer wind error (σ_u), and de-correlated exponentially as a particle moved in space or time based on horizontal (l_x), vertical(l_z), or temporal (l_t) length scales determined using observed correlation statistics from variogram analysis [Lin and Gerbig, 2005]. This formulation increased the spread of particles in STILT, and allowed estimation of uncertainty from random WRF transport error.

For our application, error statistics were generated from monthly timeseries. Application of Equation 1 presented problems at urban sites that occasionally observed large CO concentrations due to stagnant conditions with very small velocities. Estimating transport error using Equation 1 led to systematic biases during these periods, as slow particles with low wind speed would almost certainly increase in wind speed due to the addition of ε. This artificially moved particles outside of the local urban area, and when using STILT with this uncertainty resulted in CO predictions systematically biased lower than control simulations during periods of low wind speeds and high CO predictions, and hence unrealistic estimates of transport error, which are assumed to be unbiased. To reduce this bias we adopted the approach that Gerbig et al. [2008] introduced in STILT for accounting for z_i errors in WRF to use with boundary layer winds. Similar to Lin and Gerbig [2005], Gerbig et al. [2008] assumed a Gaussian error distribution for z_i, and neglected the mean error component by assuming it to be small relative to random error, and the standard deviation of the Gaussian random error (σ_{zi}) was set equal to the standard deviation of WRF z_i errors relative to observations. However in Gerbig et al. [2008] σ_{zi} was scaled by the mean observed z_i, and then introduced as a multiplicative factor directly influencing particle mixing ratio, instead of an additive term as in Equation 1. We adopted this for estimating transport error by boundary layer winds by scaling σ_u by the monthly mean wind speed for each site and applying this value as a multiplicative factor on particle velocity in both the U and V directions. This procedure removed the artificial CO bias at low wind speeds. Finally, following the approach of Lin and Gerbig [2005] we assessed the fraction of uncertainty in CO prediction that can be attributed to simulated meteorological errors by calculating the mean difference in variance of the 500 particle CO mixing ratios between a control run with neither boundary layer nor wind error applied, and separate simulations with uncertainty in boundary layer height and wind velocity included.

2.5.4. Data Filtering for CO Analysis

WRF-STILT is a state-of-the-art atmospheric transport model that has been successfully used to estimate surface emissions in a variety of studies (e.g., Jeong et al. [2013], Miller et al. [2013]). Additionally, the CARB CO inventory potentially represents the most accurate and detailed spatially explicit bottom-up prior estimate of surface emissions available. However, limitations remained that required periods to be excluded from the analysis. In this study, the key limitations included meteorological conditions that violated our assumption that particle trajectories originate from the Pacific Ocean and sample background mixing ratios of CO at 130°W, the representation of wildfires in prior surface emissions, and limitations due to periods of WRF meteorology and transport deviating significantly from observed conditions.

To reduce the impact of particle trajectories not reaching 130°W we excluded CO predictions during periods when low fractions of the particles' trajectories reached 130°W during the seven-day period. During October 2013-May 2014 we removed results from hours when this fraction was less than 0.8. During June 2013-September 2013 we relaxed this slightly to 0.7 in order to retain significantly more CO prediction periods due to seasonal shifts in meteorology reducing the fraction of particles reaching the 130°W boundary.

Wildfires represent very distinct periods of emissions from relatively small areas. Moreover, the location and timing of wildfires changes each year. Since the CARB CO prior emission inventory used in this study was developed for 2012, emissions from wildfires would not be valid for the 2013-2014 period of this study and were not used. To mitigate the influence of wildfires on our comparison of CO predictions and observations we excluded periods when observations appeared to have been influenced by wildfires. The location and duration of major wildfires were identified using the CALFIRE database for 2013 and 2014 (http://www.fire.ca.gov/general/firemaps.php). Hourly footprints for each site were inspected to determine the likelihood that an identified fire could be influencing CO observations. Periods when it was likely that wildfires were influencing observations were excluded from the analysis. However it should be noted that this analysis was limited to relatively large fires, and the potential impact of small-localized burns may not have been accounted for.

Regional WRF meteorological errors were identified using observations of wind speed and direction from ISD, CIMIS, and BAAQMD surface stations near GHG observation towers (within 50 km). Periods when the wind speed error normalized by observed wind speed exceeded 0.5 or the mean difference in wind direction between observed and simulated surface winds exceeded 90 degrees were excluded from the analysis. Additionally, at the ARV GHG measurement site we identified model deficiencies in transport for southeasterly winds (70-190° East of North) from November 2013 – January 2014, which led to periods of large underestimates in predicted CO that persisted across all tested boundary layer – land surface model combinations. These periods were excluded from the CO analysis. We hypothesize that this deficiency may be due to excessive boundary layer venting of air parcels during these periods due to difficulties in the representation of complex local topography.

2.6. Data and Method for Fossil Fuel CO_2

2.6.1 Air Sampling and $^{14}CO_2$ Measurements

Air was collected at three sites in central (WGC; 38.27°N, 121.49°W) and southern California (CIT; 34.14°N, 118.12°W and SBC; 34.09°N, 117.31°W) (see Figure 3 for site locations). Data from these sites have been used for previous estimates of CH_4 [Jeong et al., 2012a; 2013], N_2O [Jeong et al., 2012b], and ffCO_2 [Newman et al., 2013] emissions from regions of California. In the current study, air sampling methods and analysis differed slightly between the different sites. For WGC, air samples were collected using automated flask packages as part of the NOAA cooperative flask sampling network. Air was collected into flow-through flasks for approximately 2 minutes at 1400 PST (2200 UTC) approximately every 2-3 days from 91 m above the ground after passing through a water trap at 5°C. At CIT, air was collected on alternate days at ~10-m elevation above ground for approximately 1 minute at 1400 PST into evacuated one-liter Pyrex flasks after passing through $Mg(ClO_4)_2$ to dry the samples. At SBC, air samples were collected every three days from 1400-1500 PST to approximate a 1-hr average by varying the flow through 2-liter flasks after passing through a water trap at 5°C.

Air samples from WGC were sent to NOAA Earth System Research Laboratory for measurement of total CO_2, and $^{13}CO_2$. CO_2 was then cryogenically extracted from the air samples and analyzed for $^{14}CO_2$ as described below. For the CIT and SBC samples, CO_2 was extracted from the air samples cryogenically, and analyzed following the methods described in Newman et al. [2008]. For WGC individual flask samples were analyzed for $\Delta^{14}C$, while samples were composited to weekly for SBC and bi-weekly for CIT. $\Delta^{14}C$ was analyzed by accelerator mass spectrometer at the Keck-CCMAS facility at the University of California, Irvine, using the methods described in Newman et al. [2013] and Xu et al. [2007]. For CIT and SBC, CO_2 variations average ± 1.4 ppm and □^{13}C varies by ± 0.15 per mil (‰), including effects of extraction, manometry, and mass spectrometry. Typical errors for $\Delta^{14}C$ average 2‰, based on long-term reproducibility of secondary standards [Newman et al., 2013].

2.6.2. Estimation of Atmospheric Fossil Fuel CO_2

Local enhancements (above background) of atmospheric fossil fuel CO_2 were computed using a mass balance between local and background measurements CO_2 using $\Delta^{14}C$ (e.g., Miller et al. [2012]; Turnbull et al. [2006]) as

$$C_{obs} = C_{bg} + C_{ff} + C_r \tag{2}$$

$$\Delta_{obs}C_{obs} = \Delta_{bg}C_{bg} + \Delta_{ff}C_{ff} + \Delta_r C_r \tag{3}$$

where C is the mixing ratio of CO_2, Δ is the $\Delta^{14}CO_2$, obs is a local observation, bg is background, ff is fossil fuel component, and r is ecosystem respiration. Here, we assume biomass burning emissions are negligible in this regional scale analysis. To remove sensitivity to large fires, however, we specifically excluded periods flagged as having fires based on the California Department of Forestry and Fire Protection (CALFIRE) database (http://www.fire.ca.gov/general/firemaps.php) and CO measurements.

Solving the above for C_{ff}, yields

$$C_{ff} = \frac{C_{obs}(\Delta_{obs}-\Delta_{bg})}{\Delta_{ff}-\Delta_{bg}} - \frac{C_r(\Delta_r-\Delta_{bg})}{\Delta_{ff}-\Delta_{bg}} \tag{4}$$

In the following work, we estimate background from a smoothed record of C_{bg} and Δ_{bg} from Pt. Barrow, AK (X. Xu, unpublished data), which we note is similar to clean air sampled at La Jolla, CA [S. Newman, private communication]. Δ_{ff} is near -1000 per mil for pure fossil fuel and near -980 per mil for WGC and -930 per mil for CIT, where small amounts of biomass derived ethanol are added to gasoline. Because Δr is similar to Δbg as compared with Δff, the 2nd term in Equation 4 can be adequately captured as a sinusoid with a small amplitude that varies with site (0.3 ppm for WGC and 0.05 ppm for CIT). As shown in the top panel of Figure 7, the $\Delta^{14}CO_2$ variations observed at WGC are consistently lower than Δ_{bg} but show a substantially similar inter-annual trend. The observed downward trend in background $\Delta^{14}CO_2$ is primarily due to global emissions of fossil fuel CO_2 which dilute the $^{14}CO_2$ content of the Earth's atmosphere. Following the approach described by Turnbull et al. [2006], we approximated the respiration term, the second term in Equation 4, as seasonal variations of -0.2 (winter) to -0.5 ppm (summer) for WGC. For CIT and SBC, where respiration is smaller and fossil fuel ^{14}C depletion of respired biomass CO_2 is likely greater, we used 0.06 (winter) to 0.11 ppm (summer) for CIT and SBC [Newman et al., 2013]. Here, we note that in both cases, these terms are small compared to variations in estimated local $ffCO_2$ and will hence have a negligible effect on estimates of $ffCO_2$ emissions. The bottom panel of Figure 7 shows the $ffCO_2$ mixing ratio estimated for WGC as a function of the date from 2009 to 2012, with estimated uncertainties including estimated variations in total CO_2 (from separate in-situ CO_2 measurements) and $^{14}CO_2$ determinations. Generally speaking, enhancements of the $ffCO_2$ mixing ratios are larger in winter than in summer, corresponding to a mixture of seasonally varying atmospheric mixing (winds and boundary layer depths) and $ffCO_2$ emissions.

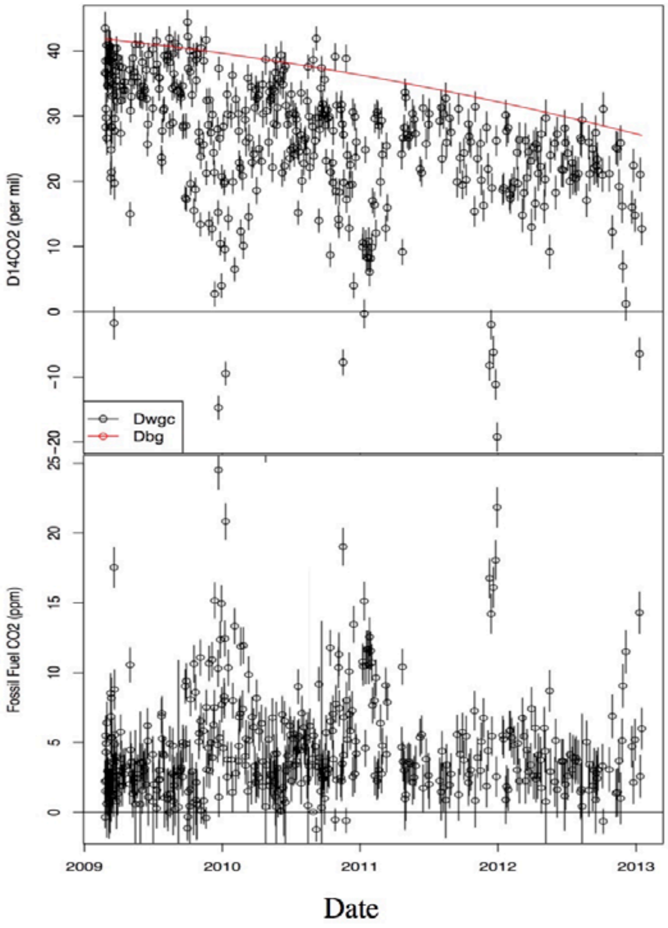

Figure 7. Measured $\Delta^{14}CO_2$ of CO_2 observed at WGC (Dwgc in black) and the smoothed background (Dbg in red) obtained from Barrow, AK (top panel), and estimated fossil fuel CO_2 for WGC (bottom panel).

2.6.3. Prior Emission Map

A prior $ffCO_2$ emission map is prepared using the spatial distribution of hourly Vulcan V2.2 emission map [Gurney et al., 2009; http://vulcan.project.asu.edu/] for 2002 and scaling to the bottom-up $ffCO_2$ estimates from the CARB inventory for 2012 [CARB, 2014] by sector. For the region outside California (e.g., part of Mexico, Canada) where the Vulcan emissions are not available, the global EDGAR emission (EDGAR4.2) was used. The source sector definitions and the annual emissions from these sectors are listed in Table 2. The difference for the annual emission is small (~2%) between Vulcan and the CARB inventory for the cement production (CEM), industrial (IND), on-road mobile (MOB) and residential (RES) sectors while the aircraft (AIR), commercial (COM), non-road mobile (NOM) and power production (UTL) sectors show a relatively large difference (see Table 2). The scaling of the original Vulcan emission to that of CARB leads to different spatial distributions of $ffCO_2$ emissions for some sub-regions. The state total of the scaled Vulcan emission map is similar to the CARB inventory within ~0.03%.

The final annual average total emission map (summing from all source sectors) used for computing the predicted mixing ratios is shown in Figure 8. From the figure, it can be seen that $ffCO_2$ emissions are dominant in the Central Valley, SFBA and SoCAB. In addition, in order to retain variations in $ffCO_2$ emissions for weekdays relative to weekends we matched the weekday and weekend emission patterns of the scaled emission map to those of the original 2002 Vulcan data, using a similar method to the CO emission map.

Table 2. Annual Fossil Fuel CO_2 Emissions by Sector for Original and Scaled Vulcan Emissions and CARB 2012 Inventory (unit = Tg CO_2/yr).

Source Sectors	Vulcan V2.2 Original	Vulcan V2.2 Scaled	CARB GHG Inventory
AIR (aircraft)	7.08	2.80	2.80
CEM (cement production)	6.38	6.89	6.89
COM (commercial)	24.18	14.13	14.12
IND (industrial)	68.36	75.88	75.87
MOB (on-road mobile)	145.55	152.22	152.19
NOM (non-road mobile)	16.65	9.58	9.58
RES (residential)	28.26	27.81	27.74
UTL (power production)	38.24	53.73	53.74
State Total	**335.70**	**343.03**	**342.93**

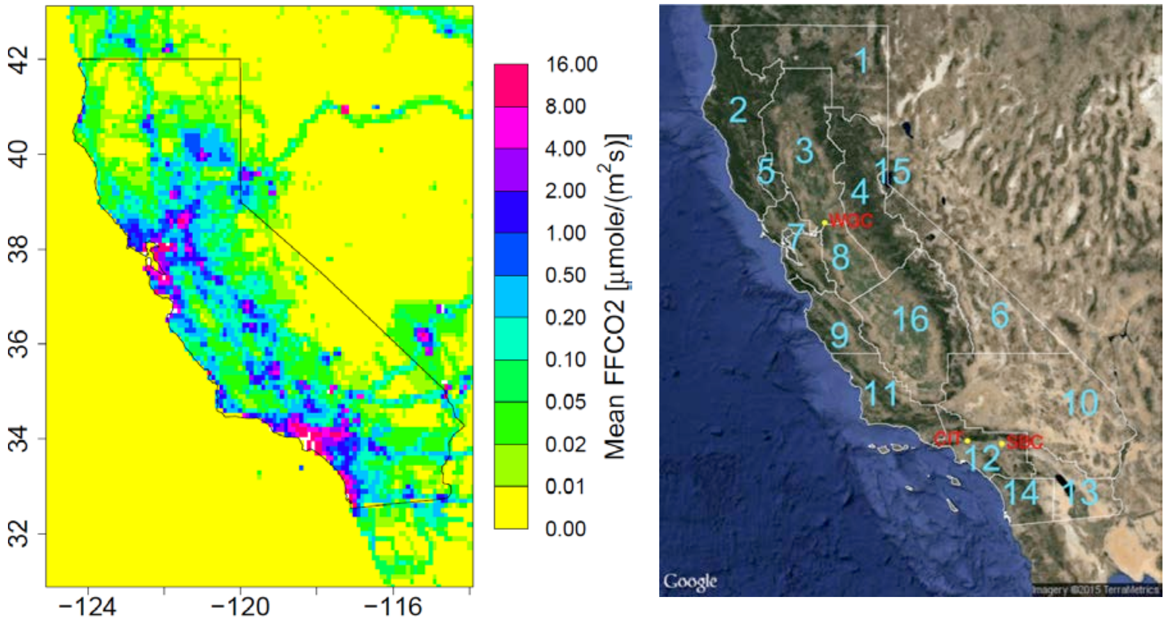

Figure 8. Scaled prior $ffCO_2$ emission map from Vulcan V2.2, combined with EDGAR4.2 for the region where the Vulcan map is not available (left) and region classification for $ffCO_2$ inversion. The San Joaquin Valley was divided into two regions (Region 8 and Region 16).

2.6.4. Atmospheric Transport Modeling

The WRF-STILT model [Lin et al., 2003; Skamarock et al., 2008; Nehrkorn et al., 2010] is used for particle trajectory simulations. For June 2013 – May 2014, WRF3.5.1 is used to simulate meteorology for the domains with 36, 12, 4 (d01, d02 and d03) and two 1.3 (d04 and d05) km resolutions. The details for the WRF model configurations are described in Section 2.5. For the inter-annual analysis for WGC during March 2009 – December 2012, we use the WRF simulations from Jeong et al. [2012a, 2012b, 2013]. The basic WRF set-up for this inter-annual analysis is summarized in Table 3 (for details see Jeong et al. [2012a, 2012b, 2013]). As in Jeong et al. [2013], we use the five-layer thermal diffusion land surface (5-L LSM) model for the April - September period and the Noah land surface model (NOAH) for the other months.

Using hourly WRF outputs, an ensemble of 500 STILT particles are released from WGC (91 m above ground), CIT (10 m), and SBC (58 m) during 12 – 17 PST. These parcels are run backward for 7 days driven with meteorology from WRF output within the d01, d02, and d03 domains for WGC and d01, d02, d03 and d04 for CIT and SBC. As in Jeong et al. [2012a; 2012b; 2013], in the inversion we use data points for which the majority of the particles (80%) reach the western boundary near 130°W.

Table 3. WRF Model Set-up for Different Modeling Periods

Period	WRF Version	Number of Domains	PBL Scheme	Land Surface Scheme	Nesting
201309-201405	V3.5.1	5	MYNN2[a]	5-L LSM[b] (April-September) NOAH[c] (other months)	2 ways
201107-201308	V3.5.1	5	MYJ[d]	5-L LSM (April-September) NOAH (other months)	2 ways
201011-201106	V3.2.1	5	MYJ	5-L LSM (April-September) NOAH (other months)	2 ways
201005-201010	V3.2.1	5	YSU	5-L LSM	2 ways
201003-201004	V3.5.1	5	MYJ	5-L LSM (April-September) NOAH (other months)	2 ways
200909-201002	V2.2	5	MYJ	NOAH	1 way
200903-200908	V3.5.1	5	MYJ	5-L LSM (April-August) NOAH (other months)	2 ways
200901-200902	V2.2	5	MYJ	NOAH	1 way

[a] Nakanishi and Niino [2006]
[b] Ruiz et al. [2010]
[c] Chen and Dudhia [2001]
[d] Mellor and Yamada [1982]; Janjić [1990]

2.6.5. Bayesian Inverse Model

We use the scaling factor Bayesian inversion (SFBI) method used in previous studies (e.g., Jeong et al. [2012a; 2012b; 2013], Wecht et al. [2014]), which relates model predictions to measurements as,

$$\mathbf{y} = \mathbf{K}\boldsymbol{\lambda} + \mathbf{v} \qquad (5)$$

where **y** is the background-subtracted measurement vector, **K** is the predicted mixing ratio which results from footprint **F** and prior emission **E** (i.e., **K** = **FE**), $\boldsymbol{\lambda}$ is a set of scaling factors to scale prior emissions, and **v** is a model-data mismatch vector with covariance matrix **R**. **R** is a diagonal matrix representing the total uncertainty contributed by all error sources such as the measurement error and the transport error. Under the Gaussian assumptions, the posterior estimate for $\boldsymbol{\lambda}$ is solved as

$$\boldsymbol{\lambda_{post}} = (\boldsymbol{K^T R^{-1} K} + \boldsymbol{Q^{-1}})^{-1}(\boldsymbol{K^T R^{-1} y} + \boldsymbol{Q^{-1} \lambda_{prior}}) \qquad (6)$$

where $\boldsymbol{\lambda}_{\text{prior}}$ is the prior estimate for $\boldsymbol{\lambda}$, and **Q** is the error covariance associated with $\boldsymbol{\lambda}_{\text{prior}}$. The posterior error covariance for $\boldsymbol{\lambda}$ can be given as

$$\boldsymbol{V_{post}} = (\boldsymbol{K^T R^{-1} K} + \boldsymbol{Q^{-1}})^{-1} \qquad (7)$$

The SFBI method is used to estimate optimal emissions at both seasonal and annual temporal scales for the WGC site and the combined CIT and SBC sites (i.e., data from both CIT and SBC are used together in the inversion). The inverse modeling is implemented in two steps (first and final) as in Bergamaschi et al. [2005], and Jeong et al. [2012a, 2012b, 2013]. This process is similar to that of McKain et al. [2015] who excluded data points with model-data residuals > 3 σ from the emission calculations. After the first inversion, the second/final inversion is conducted using data selected by another set of criteria, $|\mathbf{y}_i - (\mathbf{K}\boldsymbol{\lambda})_i|^2 < \alpha \mathbf{R}_i$ where α is a factor applied to $\mathbf{R}_i$. The values of α are determined optimizing the chi-square statistics to 1 (α ranges from 2 – 3). Both the first and second inversions use the original prior emission maps, which means that the first inversion can be recognized as a data selection tool for the atmospheric observations. In the final inversion, the outliers, which might produce biases in the inversion, are removed.

2.6.6. Uncertainty Covariance Matrix

In SFBI, the error covariance matrix, **R**, represents the expected model-measurement mismatch error for each observation. Here, **R** is expressed as a diagonal matrix assuming uncorrelated errors, where each element is computed as a quadrature sum of uncertainties from different error sources including the number of particles released, flux aggregation, errors in modeled atmospheric transport, and estimated background mixing ratio [Jeong et al., 2012a; 2012b; 2013]. In particular, uncertainty due to the atmospheric transport model are evaluated by propagating determining biases and random errors in WRF predictions of wind velocities and PBL through the STILT model to estimate mixing ratio signals [Jeong et al., 2013]. Here, we express the transport contributing to the elements of the **R** matrix as fractions of the mean background-subtracted measurement for each season, because the uncertainty dominated by transport errors tends to be proportional to the mean mixing ratio for a given period as shown in Jeong et al. [2012a; 2012b; 2013]. The average measured mixing ratio for each season is shown in Table 4 for different sites. To examine the sensitivity to the assumed uncertainty, three different factors of 0.3, 0.5 and 0.7 are used to obtain the model-data mismatch uncertainty as a fraction of the mean measurement for each season. For example, with a factor of 0.3 we prescribe 30% of the mean measured mixing ratio to the diagonal elements of the **R** matrix for a given season. We will mainly provide the result using the factor of 0.5 and discuss the sensitivity test results depending on different assumptions.

Similarly, **Q** is used to specify the expected fractional uncertainty in emissions relative to the prior model estimates. Under the assumption that uncertainties are uncorrelated, the prior model uncertainty is expressed in the diagonal terms of **Q**. For this work we assume that the uncertainty in the ffCO_2 emissions at the air basin level is estimated at 25%, based on a county level comparison with an independent California-specific bottom-up fuel use estimates for counties in California [de al Rue du Can et al., 2008]. Under the assumption that the uncertainties between regions are uncorrelated, summing 25% emission uncertainties in quadrature yields a ~10% uncertainty in state-total ffCO_2 emissions, similar to earlier assessments of likely uncertainty in annual ffCO_2 emissions for countries with detailed accounting standards [NRC, 2010]. We then also test the sensitivity of the results to varying the prior uncertainty from 25% to 50% and 75%.

Table 4. Mean Measured Mixing Ratios after Subtracting Background at WGC during 2009-2012 and at CIT and SBC during 2013 - 2014 (unit = ppm).

Site	Year	Winter	Spring	Summer	Fall
WGC	2009	NA	3.7	2.8	4
WGC	2010	8.3	3.7	4.2	4.7
WGC	2011	7.6	4.2	2.9	4
WGC	2012	7.1	4	2.9	3
CIT	2013-2014	26.7	23.9	26.6	22.1
SBC	2013-2014	8.8	5.8	11.1	10.2

2.7. Data and Method for CH_4

2.7.1. CH_4 Measurements and Background

The details of instrumentation and measurements for CH_4 are presented in Section 2.2 – 2.4. Also, detailed information regarding measurement methods for the Central Valley sites are summarized in Jeong et al. [2012a, 2013], and Andrews et al. [2014]. Here, we briefly describe measurements as a component of the inverse modeling framework. CH_4 measurements were made at the collaborative 13 GHG sites across California during June 2013 – May 2014. The information of data availability is summarized in Table 5 (see

Figure 1 for site locations). All sites are operated with temperature and pressure controlled cavity ring-down CH_4 gas analyzers (Picarro Inc.), permeation-tube gas sample driers, and periodic calibrations using either primary NOAA CH_4 gas standards or secondary gas standards.

For this study, we added four new sites in the Southern California: CIT, SBC, SIO and VTR, and two sites for SFBA: LVR and STR. All new sites except STR had similar instrumentation to existing sites, while STR employed daily flask samples collected for approximately 2 minutes near 1400 PST for subsequent analysis at NOAA Earth System Research Laboratory. For continuous measurement sites, calibrated data were averaged to hourly intervals. All sites are expected to provide measurement precision that is smaller than the CH_4 synoptic variations typically observed in the ambient air, and with absolute accuracy sufficient to provide negligible bias in estimating the scaling relationship between observed and predicted CH_4 signals.

Following previous work (e.g., Jeong et al. [2013]), we selected measurements that coincided with periods where the atmospheric boundary layer was well-mixed. For the Walnut Grove tower (WGC) we explicitly evaluated atmospheric mixing using measured vertical CH_4 profiles. As in Jeong et al. [2012a, 2013], WGC data from 91 m were selected in the time window between 1200 and 1700 local standard time (LST), subject to the requirement that the CH_4 mixing ratio difference $([CH_4]_{91m} - [CH_4]_{483m})$ between 91 and 483 m fell within the range -1 sd < $([CH_4]_{91m} - [CH_4]_{483m})$ < 3 sd, where sd is the standard deviation of the 91 - 483 m difference. This additional requirement retained approximately 80% of data in the 1200 – 1700 LST window. Following this approach for other sites without profile information, we also selected data in the afternoon time window (1200 – 1700 LST).

Table 5. CH_4 Measurement Data Availability for Each GHG Site across California

Site	Location	Data Availability
ARV*	Arvin	June 2013 – May 2014
CIT	Caltech, Pasadena	June 2013 – May 2014
LVR	Livermore	June 2013 – May 2014
MAD*	Madera	June 2013 – May 2014
STB*	Sutter Buttes	June 2013 – May 2014
STR	San Francisco	June 2013 – May 2014
THD	Trinidad Head	June 2013 – August 2013
TRA*	Tranquility	June 2013 – May 2014
TSB*	Tuscan Buttes	June 2013 – May 2014
VTR	Victorville	June 2013 – August 2013
WGC	Walnut Grove	June 2013 – May 2014
SBC*	San Bernardino	June 2013 – May 2014
SIO	Scripps	June 2013 – May 2014

*Indicates CARB's statewide GHG monitoring network sites.

The predicted CH_4 upstream boundary values were estimated using a similar method to the one used in Jeong et al. [2012b, 2013]. The details for estimating the boundary values are described in Jeong et al. [2013] and only a summary is provided here. CH_4 boundary values were estimated using data from the Pacific coast aircraft network CH_4 profiles (http://www.esrl.noaa.gov/gmd/ccgg/aircraft/) and remote Pacific marine boundary layer sampling sites (http://www.esrl.noaa.gov/gmd/ccgg/flask.html) within the NOAA Earth System Research Laboratory (ESRL) Cooperative Air Sampling Network. The data were smoothed and interpolated to create a three-dimensional (3-D) curtain, varying with latitude, height and time. To quantify the errors associated with the 3-D curtain, we fit a smooth curve through the data and computed the seasonal cycle of the root mean square of the residuals from the curve. Predicted background values were computed for each hourly footprint simulation by sampling the curtain at each of the 500 particle trajectory endpoints (near the domain boundary at 130°W) and calculating the average value.

2.7.2. CH_4 Prior Emission Model

This work used the California Greenhouse Gas Emission Measurements (CALGEM) project prior CH_4 emission model (henceforth CALGEM model, available at calgem.lbl.gov) described by Jeong et al. [2012a, 2013, 2014] with some modifications. The CALGEM emission model provides emissions by sector at a high spatial resolution ($0.1^{\circ} \times 0.1^{\circ}$) for California. The CALGEM model has seasonal components for wetlands and crop agriculture only, and these seasonal emissions are combined with non-seasonal emissions to construct monthly emission maps for inversions. The inversion approach using non-seasonal prior emissions is widely used (e.g., Zhao et al. [2009], Jeong et al. [2012a; 2012b; 2013], Wecht et al. [2014], Cui et al. [2015]). In particular, Jeong et al. [2012a; 2012b; 2013] showed non-seasonal priors can provide information on seasonality in the posterior emission.

In this study, the CALGEM prior emissions distributions are scaled to match 2012 CARB state totals for anthropogenic emission sectors [CARB, 2014; March 2014 version], with small (< 50 Gg CH_4/yr) adjustments for some regions and sectors (per ARB staff private communication). The spatial distribution of the dairy livestock emissions was revised by incorporating the 2012 county-level dairy statistics from USDA (http://www.nass.usda.gov/Statistics_by_State/California/Publications/County_Estimates/2013lvsceF.pdf) using the spatial distribution from Jeong et al. [2013]. This revision changed the dairy livestock emissions for each region due to recent changes in the number of dairy cows, in particular for SoCAB. The current dairy livestock emissions in SoCAB (Table 6) decreased by ~50% compared to those (~80 Gg CH_4/yr) of Jeong et al. [2013], which was based on the 2004 statistics reported in Salas et al. [2009], reflecting the decrease in the number of dairy cows in the region (see Appendix A for the trend of dairy cows in SoCAB). In addition, we used the prior emission map for natural wetlands from Jeong et al. [2013].

Table 6 provides annual CALGEM prior emissions used in this study by source and region, and Figure 9 shows the annual total emission maps for the CALGEM prior emission model along with the sub-region classification by which the CALGEM model was scaled to CARB's inventory. The regions in this study are different from those in Jeong et al. [2013] and follow the California Air Basins (http://www.arb.ca.gov/ei/maps/statemap/abmap.htm). Inversion results are summarized by region to be compared with the prior emissions. Based on the prior emission estimates, the Central Valley (Regions 3 and 8) accounts for 55% of the total statewide CH_4 emissions and the two major urban regions (Regions 7 and 12) account for 29% of the total. In terms of source sectors, livestock emissions represent 52% of the state total emission followed by landfills (20%) and natural gas (17%; petroleum production included). Livestock emissions are concentrated in Region 8 (San Joaquin Valley) where 86% (667 Gg CH_4 / 775 Gg CH_4) of the region's total emissions are from livestock. This is consistent with a recent study by Gentner et al. [2014] that suggests the majority of CH_4 emissions in the San Joaquin Valley are from dairy operations. Since the CALGEM prior emissions were scaled by the CARB inventory by both region and sector, the two bottom-up emissions will be used interchangeably for the remainder of this study unless otherwise specified.

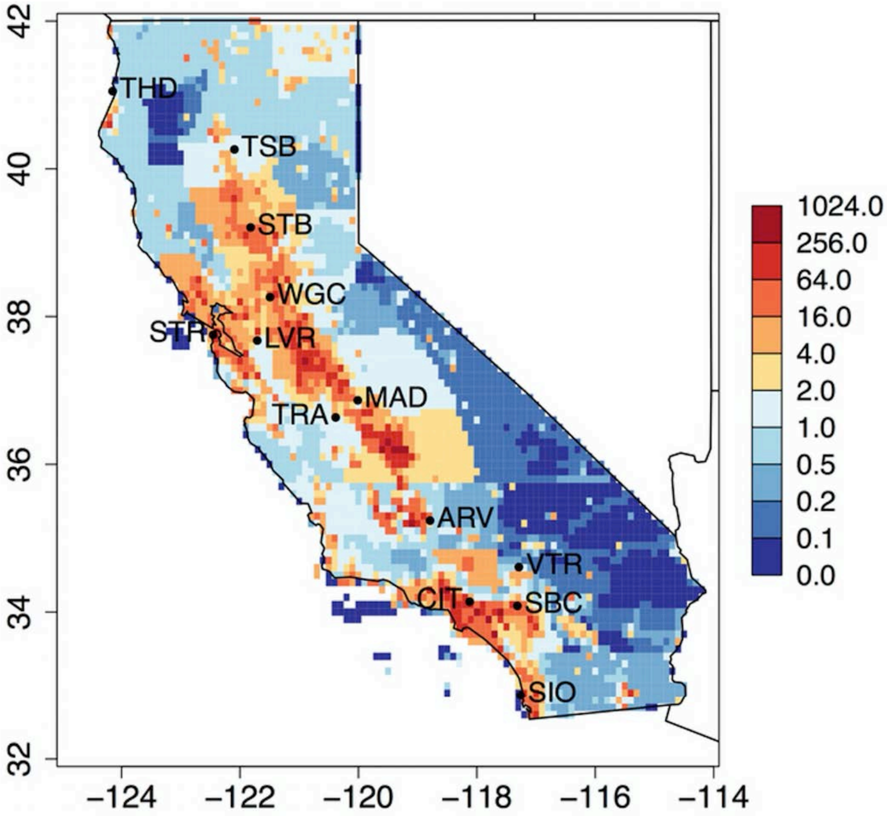

Figure 9. CALGEM total (1.7 Tg CH_4/yr, 1 Tg = 10^{12} g) prior emissions (nmol/m^2/s) with locations of measurement sites across California

Table 6. Annual CARB-Scaled CALGEM CH_4 Emissions by Region and Sector (Gg CH_4)

Source[a]\Region[b]	GBV (6)	LC (5)	LT (15)	MC (4)	MD (10)	NC (2)	NCC (9)	NEP (1)	SC (12)	SCC (11)	SD (14)	SF (7)	SJV (8)	SS (13)	SV (3)	Total
DLS	0.1	0.0	0.1	2.5	21.1	21.7	2.8	2.2	37.9	1.0	2.6	14.3	598.1	3.8	30.1	**738.3**
LF	1.1	1.5	0.0	2.6	8.2	2.3	9.0	1.1	157.0	14.3	26.3	53.9	28.7	3.1	26.4	**335.4**
NDLS	2.0	0.4	0.1	8.3	3.5	8.2	5.2	13.3	5.8	8.3	1.9	10.5	68.5	1.6	19.8	**157.4**
NG	0.2	0.4	0.2	2.3	5.5	1.7	4.0	0.4	112.2	17.4	16.2	38.8	51.1	3.1	29.8	**283.3**[c]
RM	0.1	0.1	0.0	2.1	2.5	0.4	0.9	0.1	12.0	1.2	2.2	10.0	4.3	0.5	3.3	**39.7**
WW	0.0	0.1	0.0	0.5	1.0	0.3	1.6	0.4	23.6	13.1	2.8	11.0	9.0	0.9	2.8	**67.1**
WL	0.3	0.0	0.0	0.5	0.1	0.2	0.2	9.9	0.9	0.5	0.2	4.1	14.0	0.1	7.1	**38.1**
CP	0.0	0.0	0.0	0.0	0.0	0.0	0.0	0.0	0.0	0.0	0.0	0.0	1.5	0.0	47.8	**49.2**
Total	**3.8**	**2.4**	**0.5**	**18.8**	**41.8**	**34.8**	**23.7**	**27.5**	**349.3**	**55.8**	**52.2**	**142.5**	**775.2**	**13.2**	**167.0**	**1708.6**

[a] Source sectors include dairy livestock (DLS), landfill (LF), non-dairy livestock (NDLS), natural gas including petroleum production (NG), petroleum refining and mobile sources (RM), wastewater (WW), wetland (WL), and crop (CP, largely rice).

[b] The number in the parentheses shows the region number shown in Figure 3.

[c] includes 24 Gg CH_4/yr from petroleum seeps (per ARB staff private communication).

2.7.3. Hierarchical Bayesian Inverse Method

We used a hierarchical Bayesian inversion (HBI) method to estimate regional CH_4 emissions in California. The HBI approach for GHG inversion work was initially introduced by Ganesan et al. [2014], and the potential advantages of HBI are well described in the study. In this work we develop an HBI method with more complex structure in representing the model-data mismatch matrix than Ganesan et al. [2014] for regional CH_4 emission quantification.

We start with Bayes' rule and describe each probability distribution in the hierarchical structure of parameters that include the scaling factor (a set of factors used to adjust prior emissions, denoted as $\boldsymbol{\lambda}$). Generally, Bayes' rule can be applied to multiple parameters at different levels as

$$p(\boldsymbol{\phi},\boldsymbol{\theta}|\boldsymbol{D}) \propto p(\boldsymbol{D}|\boldsymbol{\phi},\boldsymbol{\theta})p(\boldsymbol{\phi},\boldsymbol{\theta}) \qquad (8)$$

$$= p(\boldsymbol{D}|\boldsymbol{\phi})p(\boldsymbol{\phi}|\boldsymbol{\theta})p(\boldsymbol{\theta})$$

where $\boldsymbol{\Phi}$ and $\boldsymbol{\theta}$ represent the generic parameters in vector form and **D** is data used to estimate the parameters. The first line in Equation 8 simply states the posterior probability is proportional to the likelihood function and prior distribution. The re-factorization in the second line of Equation 8 holds because the data **D** depend only on the parameter $\boldsymbol{\phi}$ (thus $\boldsymbol{\theta}$ is factored out) and the values of $\boldsymbol{\phi}$ depend on the values of $\boldsymbol{\theta}$, constructing a hierarchical structure. The transition of $p(\boldsymbol{\phi},\boldsymbol{\theta})$ to $p(\boldsymbol{\phi}|\boldsymbol{\theta})p(\boldsymbol{\theta})$ is by the property of a conditional probability, given the dependence of $\boldsymbol{\phi}$ on $\boldsymbol{\theta}$. Any probabilistic model that can be factorized in chains as shown in Equation 8 is a hierarchical model [Kruschke, 2015, p. 223].

The general model in Equation 8 can be applied to estimate surface emissions and their uncertainties. For GHG applications, the parameter vector $\boldsymbol{\phi}$ can be scaling factors for emission adjustment (or surface emission itself). The vector $\boldsymbol{\theta}$ can be a set of parameters including the hyper-parameters (e.g., mean) that determine the distribution for the scaling factor or surface emissions.

We use the following linear model for estimating scaling factors for regional emissions [Zhao et al., 2009; Jeong et al., 2012a; 2012b; 2013; Wecht et al., 2014]

$$\mathbf{y} = \mathbf{K}\boldsymbol{\lambda} + \mathbf{v} \qquad (9)$$

where $\mathbf{y}$ is the measurement vector ($n \times 1$), which represents 3-hourly local mixing ratio time series after subtracting background values, $\mathbf{K} = \mathbf{FE}$ (an $n \times k$ matrix), $\mathbf{F}$ is the footprint ($n \times m$), $\mathbf{E}$ is prior emissions ($m \times k$), $\boldsymbol{\lambda}$ is a $k \times 1$ vector for scaling factors with a covariance matrix $\mathbf{Q}$ ($k \times k$), and $\mathbf{v}$ is a vector representing the model-measurement mismatch with a covariance matrix $\mathbf{R}$ ($n \times n$). In this study we solve for a vector of 195 for $\boldsymbol{\lambda}$ which includes 0.3°×0.3° grid cells (a total of 183) for the major regions (i.e., SV, SJV, SFBA, SC). We aggregated grid cells from other 12 regions at the sub-region scale so that the number of parameters can be reduced for those regions with low prior emissions and low sensitivity. Thus, after solving $\boldsymbol{\lambda}$ using the HBI method and multiplying it by $\mathbf{E}$, we can obtain posterior emissions (a vector of m).

For the model in Equation 9, the joint parameters we need to estimate are

$$\boldsymbol{\Theta} = \{\boldsymbol{\lambda}, \boldsymbol{\mu_\lambda}, \boldsymbol{\sigma_\lambda}, \boldsymbol{\sigma_R}, \eta, \tau\} \qquad (10)$$

where $\boldsymbol{\lambda}$ is the scaling factor, $\boldsymbol{\mu_\lambda}$ is the prior mean for $\boldsymbol{\lambda}$**,** $\boldsymbol{\sigma}_{\lambda}$ is the uncertainty for $\boldsymbol{\lambda}$ (i.e., square root of diagonal elements of $\mathbf{Q}$), $\boldsymbol{\sigma}_{\mathbf{R}}$, η and τ are the parameters used to construct the model-measurement mismatch matrix $\mathbf{R}$ (see below for the representation of $\mathbf{R}$). The diagonal elements of $\mathbf{R}$ represent the total model-measurement mismatch errors that are propagated through the inversion while $\mathbf{Q}$ is used to define the uncertainty level for the prior emission. These two quantities need to be either prescribed with known values or estimated. In HBI we estimate the joint parameter set simultaneously, using the measurements only once. This joint estimation is different from previous approaches (e.g., Jeong et al. [2013]) where the covariance matrix $\mathbf{R}$ was prescribed via explicit estimation without using atmospheric measurements or other methods where atmospheric measurements were used to optimized $\mathbf{R}$ (then measurements are also used for inversions, e.g., Michalak et al., [2005]).

With the parameter set identified, we need to write out the posterior probability up to the likelihood function and prior densities (not including the evidence in the denominator in

Bayes' rule). We apply the identified joint parameter (i.e., **Θ**) to the general formulation of a hierarchical model in Equation 8 to get the posterior probability as

$$p(\boldsymbol{\lambda}, \boldsymbol{\sigma_\lambda}, \boldsymbol{\sigma_R}, \eta, \tau | \boldsymbol{y}) \propto p(\boldsymbol{y}|\boldsymbol{\lambda}, \boldsymbol{\sigma_R}, \eta, \tau) p(\boldsymbol{\lambda}|\boldsymbol{\mu_\lambda}, \boldsymbol{\sigma_\lambda}) p(\boldsymbol{\mu_\lambda}) p(\boldsymbol{\sigma_\lambda}) p(\boldsymbol{\sigma_R}) p(\eta) p(\tau) \quad (11)$$

where the right-hand side shows the likelihood function and the prior distribution for each parameter. Note that in Equation 11 all variables are in vector form except for η and τ. To build Markov chain Monte Carlo (MCMC) samplers for the posterior distribution in Equation 11, the JAGS system (just another Gibbs sampler, Plummer [2003]) is used together with the R statistical language (https://cran.r-project.org/). JAGS has been widely used for statistical inference studies in many fields including ecology and genetics [Korner-Nievergelt et al., 2015; McKeigue et al., 2010]. The individual distributions in Equation 11 require explicit consideration and are described below.

First, for the likelihood function we use

$$p(y|\boldsymbol{\lambda}, \boldsymbol{\sigma_R}, \eta, \tau) \sim N(\boldsymbol{K\lambda}, \boldsymbol{R}) \quad (12)$$

where *N* is the normal distribution(here multivariate truncated normal) with mean **Kλ** (*n* × 1) and covariance **R** (n × n). Note that **y** is conditionally independent of all other parameters given **λ**, $\boldsymbol{\sigma_R}$, η and τ.

In order to estimate parameter values with Bayesian inference, prior uncertainty needs to be specified in a hierarchical fashion. In other words, the hierarchical model needs to be expanded to include prior uncertainty for the joint parameter set **Θ** using a series of distributions. The scaling factor **λ** is sampled from a normal distribution instead of a fixed value (e.g., Jeong et al. [2013], Wecht et al., [2014]) as

$$p(\boldsymbol{\lambda}) \sim N(\boldsymbol{\mu_\lambda}, \boldsymbol{\sigma}_\lambda) \quad (13)$$

where $\boldsymbol{\mu_\lambda}$ itself is sampled from a truncated normal distribution with a mean of 1 and a standard deviation of 0.5 so that 68% of the samples are within 50 ~ 150% from the mean, which is a similar set-up to that of Ganesan et al. [2014]. $\boldsymbol{\sigma}_\lambda$ is modeled using a half Cauchy distribution, which is one of the recommended distributions for model variances [Gelman and Hill, 2007; Gelman et al., 2014; Korner-Nievergelt et al., 2015]. The hyper-parameterization ("hyper" meaning the upper level in the hierarchy) for $\boldsymbol{\sigma}_\lambda$ can formally be expressed as

$$\boldsymbol{\sigma_\lambda} \sim hCauchy\ (0,1) \quad (14)$$

where *hCauchy* is the half-Cauchy distribution. Note we take the absolute value from the Cauchy distribution so that we consider the positive values only (i.e., half Cauchy). The use of 1 for the half Cauchy scale parameter (the larger the scale parameter, the more spread out the distribution) is similar to assuming the uncertainty for $\boldsymbol{\lambda}$ is 100% in the classical Bayesian inversion (e.g., Jeong et al., [2013], Wecht et al. [2014]). The difference is that in this study $\boldsymbol{\sigma}_\lambda$ is sampled from a distribution with a heavy tail (see

Appendix C for an example half Cauchy distribution) so that $\boldsymbol{\sigma}_{\lambda}$ can be optimized from a broad distribution (instead of being a fixed value).

For the model-measurement covariance matrix **R**, we use a popular exponential covariance function, which can be written in general form as [Rasmussen and Williams, 2006]

$$R_{i,j} = \eta^2 \exp\left(-\frac{1}{\tau}|t_i - t_j|\right) + \delta_{i,j}\sigma_{R_s}^2 \quad (15)$$

where η, τ, and σ_{R_s} are parameters that define the covariance function, *t* is the measurement time, and δ is the Kronecker delta function (value of 1 if i = j, otherwise zero). Note that here we use the L_1 norm (i.e., $|t_i - t_j|$) as in Ganesan et al. [2014]. The subscript *s* in σ_{R_s} indicates that σ_R is estimated for each site as was done in Jeong et al. [2013] for their multi-tower analysis. This set of multiple parameters for σ_R adds more complexity to the model (than estimating a single value for σ_R) but reflects the fact that model-measurement errors are not uniform across California.

We modeled σ_{R_S} using the half Cauchy distribution as in σ_{λ} as recommended by [Gelman and Hill, 2007; Gelman et al., 2014; Korner-Nievergelt et al., 2015]. The scale parameter (in the hyper-parameter sense) for the half Cauchy distribution for σ_{R_S} is calculated using the first order approximation method in Jeong et al. [2012a, 2012b, 2013] and used as

$$p(\sigma_{R_s}) \sim hCauchy(0, \sigma_{R_{p|s}}) \quad (16)$$

where $\sigma_{R_{p|s}}$ is the first-order estimate for σ_{R_S} and includes errors from several sources (e.g., transport and background errors) combined in quadrature. More details for $\sigma_{R_{p|s}}$ are described in the following section. Also, we list the error sources and describe the estimation method in Appendix G.

For η, we use non-informative prior as

$$\eta \sim unif(0, L) \quad (17)$$

where η is allowed to vary from 0 to L with an equal probability of $1/L$. Since η is generally estimated to be smaller than $\sigma_{R_{p|s}}$ we use $\sigma_{R_{p|s}}$ as an upper limit for L for efficient sampling.

Following Ganesan et al. [2014], we use the exponential distribution for τ as

$$\tau \sim \exp\left(\frac{1}{\tau_p}\right) \quad (18)$$

where τ_p is the hyper parameter for τ, which is assumed to be 7 days (typical synoptic time scale for transport, Ganesan et al. [2014]).

2.7.4. Uncertainty Covariance Matrix

The posterior distribution in Equation 11 is used to generate Markov chain Monte Carlo (MCMC) samples for the parameters (i.e., $\boldsymbol{\Theta}$) in Equation 10, which include the components of the error covariance matrices **R** and **Q**. In other words, we estimate the model-measurement mismatch covariance matrix (i.e., **R**) simultaneously with $\boldsymbol{\lambda}$ and other parameters (using the measurements just once) instead of using fixed values. The **R** matrix can be estimated without prior knowledge (e.g., uniform distribution) or use a simple assumption for the hyper-parameter as in Ganesan et al. [2014] where for the hyper-parameter of the variance component of **R** they used the sum of the fixed instrument uncertainty and the uncertainty associated with propagating the calibration scale (0.05 pmol/mol, respectively). Here we take a more informed approach by using a combination of reported values for **R** from Jeong et al. [2013] and new estimates from this study for those sites not included in Jeong et al. [2013]. Jeong et al. [2013] reported the model-measurement mismatch uncertainties for the five sites in the Central Valley, which include ARV, MAD, TRA, WGC and STB. For other sites, we estimated the model-measurement uncertainty for summer of 2013 following the method from Jeong et al. [2012a, 2012b, 2013] (see Appendix G for details). For other seasons, we scaled the summer uncertainty estimates in proportion to the monthly background-subtracted mean signal. We use these uncertainty values (i.e., $\sigma_{R_{p|s}}$) as the hyper-parameter for σ_{R_s} in the covariance function for **R**. More specifically, $\sigma_{R_{p|s}}$ is used as the scale parameter in the half Cauchy distribution in Equation 16 (see Appendix F for $\sigma_{R_{p|s}}$). The diagonal elements of **R** were then calculated as the sum of squares of σ_{R_s} and η for each month. An example of the half Cauchy distribution is provided in Appendix C, which shows a long tailed distribution with a relatively large mass for more likely values [Gelman and Hill, 2007; Korner-Nievergelt et al., 2015].

Figure 10 shows the (optimized) posterior model-measurement mismatch uncertainty (i.e., square root of the diagonal elements of **R**) given the atmospheric measurements for several measurements sites that constrain the major emission regions (SV, SJV and SC regions) (see Appendix D for correlation between posterior (σ_{R_s}) and prior ($\sigma_{R_{p|s}}$)). Recall that the **R** matrix is also estimated because all the parameters in the set $\boldsymbol{\Theta}$ in Equation 10 are optimized simultaneously by HBI. The HBI approach allows for estimation of model-measurement mismatch uncertainty values while inferring posterior emissions, using the measurements only once. This means that the model-measurement mismatch uncertainty has posterior estimates given the prior ($\sigma_{R_{p|s}}$) and data. Overall, the posterior values follow the trend of the prior in seasonality and magnitude (Figure 10). In most sites, both the prior and posterior uncertainties are large during the winter season when boundary layer heights are low and predicted mixing ratios are very sensitive to the simulated boundary layer.

The uncertainty for the scaling factor (i.e., $\boldsymbol{\sigma}_{\boldsymbol{\lambda}}$, diagonal terms in **Q**), which represents the confidence of the prior emission, is also estimated (instead of being prescribed). As in $\boldsymbol{\sigma}_{\mathbf{R}}$, the posterior values of $\boldsymbol{\sigma}_{\boldsymbol{\lambda}}$ are estimated given the prior as a hyper-parameter (1 for the scale parameter or 100%, Equation 14). For the major emitting regions (3, 7, 8 and 12), the region average of the prior uncertainties for individual pixels is estimated to be

~150% (see Appendix E), which is higher than the prescribed 70% in Jeong et al. [2013]. Because in this study we conduct pixel-based inversions for the major emitting regions, we expect the prior uncertainties for individual pixels are higher than the subregion-level prior uncertainty in Jeong et al. [2013].

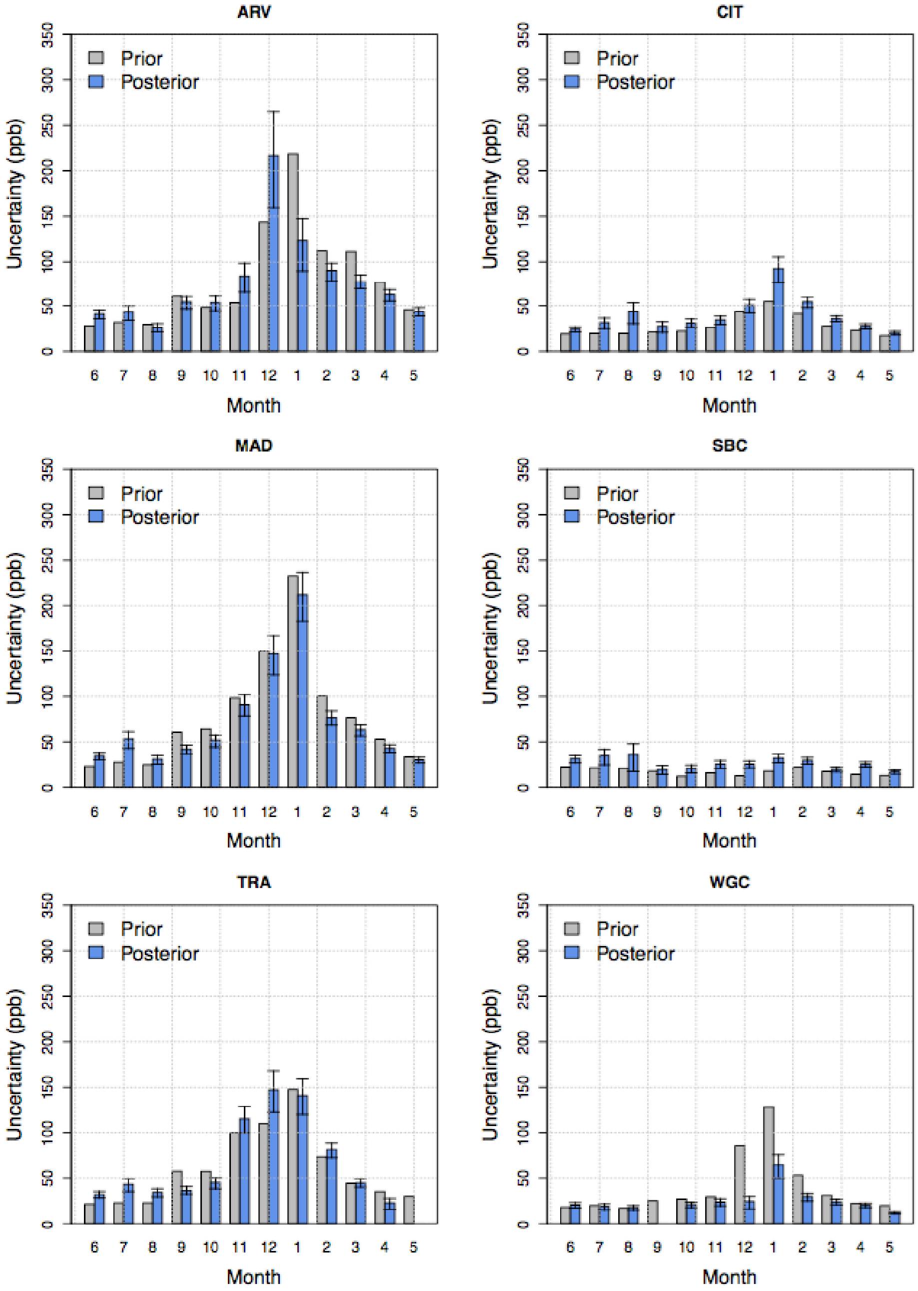

Figure 10. Estimated diagonal elements of the model-measurement mismatch matrix R for CH$_4$ inversions. The posterior values were estimated using 25000 MCMC samples and the error bar represents the 68% confidence interval. The prior values were estimated using the method described in Jeong et al. [2012a, 2012b, 2013] (also see Appendix G). For May at TRA and September at WGC, the posterior values were not estimated because most of the measurements were not available.

2.8. Inverse Method for N_2O

2.8.1. N_2O Measurements and Background

The details of instrumentation and measurements for N_2O are presented in Section 2.2 – 2.4. Here, we briefly describe measurements as a component of the inverse modeling framework.

Dry mole N_2O mixing ratios were measured at six tower sites across California (Table 7). Among them, measurements from the ARV, STB, and WGC sites mainly constrain emissions from California's Central Valley, while the CIT, SBC and STR sites are used to infer emissions from the major urban regions in California.

Briefly, the measurements are made using a sampling and analysis system that combines pumps, membrane (Nafion) air driers, and gas analyzers. While all sites utilized off-axis Integrated Cavity Output Spectroscopy (ICOS) (LGR Model 907-0015; Los Gatos Research Inc., CA), air handling and calibration methods differed across the sites (Table 7). At a subset of sites (WGC, SBC) air sampling is switched between the multiple heights (WGC: 30, 91, 483 m AGL, every 300 s; SBC: 27, and 58 m AGL, every 400 s) with measurements allowed to settle, with only the last 120 seconds used as for the ambient air measurement. Only 91m (WGC), and 58m (SBC) measurements were used for the following inverse model analysis. For the other sites, measurements were made at a single height on those towers and switching was on only necessary for calibrations.

The instrument offset and gain were measured periodically and corrected using two methods. For a subset of sites (SBC, WGC) calibrations employed three secondary gas standards tied to NOAA primary standards. The offset and gain of the LGR instrument were measured every 3 (WGC) and 4 (SBC) hours using two "high-low" secondary standards and then checked with the third "target" standard at times midway between the "high-low" calibrations. At CIT, offset and gain were calibrated every 3 months using NOAA primaries and offset was calibrated using a secondary standard every 4.5 hours and checked for consistency using every other measurement. For the other two in-situ sites (ARV and STB), a "precision check" was performed every 23 hours using an un-calibrated secondary gas cylinder. For two sites (WGC and STR), N_2O was also measured in flask samples collected at 2200 GMT (1400 PST) and analyzed by NOAA's cooperative air sampling network. For WGC, SBC, and CIT, target check measurements showed root-mean-square (RMS) variations less than less than 0.1 ppb. For WGC, the observed RMS difference between flask measurements and in-situ measurements interpolated to the time of the flask sample varied from ~ 0.3 - 0.5 ppb, consistent with the expected variation in flask measurements (www.esrl.noaa. gov/gmd/ccgg/flask.html). For sites with infrequent (23 hr) precision checks (ARV, STB) which do not facilitate correction of diurnal variations in instrument offset due to temperature, the residual observed RMS variation was ~ 0.5 to 1 ppb, depending on the time period.

Following calibration, N_2O measurements were averaged to 3-hour time intervals (with the exception of flask samples) and are expected to have precision limited by the combination of instrument noise (typically 0.05 ppb RMS for ~100 s average) and atmospheric variability (typically > 0.05 ppb and as large as 0.5 ppb for sites in regions with large N_2O emissions), with total random variation due to accuracy that is assumed to vary from 0.2 ppb for well calibrated sites (e.g., CIT, WGC), 0.4 ppb for sites with flask measurement (STR), and 1 ppb for sites with infrequent calibration (STB, ARV).

Table 7. GHG Site Information across California

Site	Location	Measurement Data Availability	Instrument Calibration Comments
ARV*	Arvin	October 2013 – May 2014	Precision check, 23 hr
CIT	Caltech, Pasadena	June 2013 – May 2014	Offset calibration, 4.5 hr
STB*	Sutter Buttes	April 2014 – May 2014	Precision check, 23 hr
STR	San Francisco	June 2013 – May 2014	NOAA flasks 2200 GMT
WGC	Walnut Grove	June 2013 – May 2014	Offset & gain calibration + target check, 3 hr NOAA flasks 2200 GMT
SBC*	San Bernardino	June 2013 – May 2014	Offset & gain calibration + target check, 4 hr

* Indicates CARB's statewide GHG monitoring network sites

The predicted N_2O upstream boundary values were estimated using a similar method to the one used in Jeong et al. [2012b, 2013]. The details for estimating the boundary values are described in Jeong et al. [2013] and only a summary is provided here. N_2O boundary values were estimated using data from the Pacific coast aircraft network N_2O profiles (http://www.esrl.noaa.gov/gmd/ccgg/aircraft/) and remote Pacific marine boundary layer sampling sites (http://www.esrl.noaa.gov/gmd/ccgg/flask.html) within the NOAA Earth System Research Laboratory (ESRL) Cooperative Air Sampling Network. The data were smoothed and interpolated to create a three-dimensional (3-D) curtain, varying with latitude, height and time. To quantify the errors associated with the 3-D curtain, we fit a smooth curve through the data and computed the seasonal cycle of the root mean square of the residuals from the curve. Predicted background values were computed for each hourly footprint simulation by sampling the curtain at each of the 500 particle trajectory endpoints (near the domain boundary at 130°W) and calculating the average value.

2.8.2. Prior N_2O Emissions

We use the spatial distribution of EDGAR 42FT2010 (European Commission Joint Research Centre (JRC) and Netherlands Environmental Assessment Agency, Emission Database for Global Atmospheric Research (EDGAR), release version 4.2 Fast Track, 2013, http://edgar.jrc.ec.europa.eu; accessed in January 2015; hereafter EDGAR) prior emission maps. To obtain California-specific prior emission maps, we scale EDGAR emissions to the CARB 2012 N_2O inventory [CARB, 2014], which provides an annual total emission for each sector without spatial information. The CARB inventory does not include an estimate for personal product use, which is included in the industrial processes and product use (IPU) sector of the EDGAR inventory. For the IPU sector, we use the estimate from EDGAR for inverse modeling, which accounts for 22% of the EDGAR total. The IPU sector in EDGAR includes emissions from chemical and solvents (e.g., nitric acid, adipic acid and caprolactam; http://edgar.jrc.ec.europa.eu/ingos/JRC-INGOS-report.pdf). Thus, the prior emissions used here consist of a hybrid of emission estimates from the CARB and EDGAR N_2O inventories (state total = 48.3 Gg N_2O/yr).

Emissions from both EDGAR and CARB are constant in time, without seasonality. Table 8 provides annual CARB-scaled EDGAR N_2O prior emissions used in this study by source and region. Figure 11 shows the CARB-scaled EDGAR emission map, which combines emissions from all anthropogenic source sectors. This scaled emission map represents our prior anthropogenic emission in the inverse analysis. The sub-regions are the same as California Air Basins (http://www.arb.ca.gov/ei/maps/statemap/abmap.htm), and inversion results are summarized by sub-region to be compared with the prior emissions. As shown in Figure 11 and Table 8, the Central Valley (Regions 3 and 8) emissions accounts for 46% of the total statewide N_2O emissions and the two major urban regions (Regions 7 and 12) account for 26% of the total. In terms of source sectors, direct (AGS) and indirect (N2O) N_2O from agricultural soils represent 41% of the state total emission followed by industrial processes and product use (IPU) (20%) and manure management (MNM) (20%). The AGS, N2O and MNM emissions are concentrated in the Central Valley, which accounts for 63% of the state total agricultural soil and manure emissions. For the IPU sector, the South Coast (SoCAB, Region 12) and San Francisco (SF, Region 7) Air Basins account for 57% and 15% of the state total, respectively.

Kort et al. [2008] and Jeong et al. [2012b] assumed that N_2O emissions from unfertilized natural soils are small compared to emissions from agricultural soils and other anthropogenic sources. In this study, we derived an emission map for natural forest based on the Global Emissions InitiAtive (GEIA) emission model [Bouwman et al., 1995] and included it in the inversion. Because the GEIA emissions are available at a coarse resolution of 1° × 1°, we used the Moderate Resolution Imaging Spectroradiometer (MODIS) land cover type data product (MCD12Q1, year 2012, available at http://e4ftl01.cr.usgs.gov/MOTA/MCD12Q1.051/2012.01.01/, accessed February 2015) to identify natural forest pixels at 0.1° (~ 10 km) resolution (see Appendix I). To minimize attribution of managed soils to natural forests, we included only the pixels with the forest ratio greater than 80%. We note that the EDGAR model estimates non-zero anthropogenic N_2O emissions in most of California except for the desert area and part of the northern forest region. Using a nearest neighborhood method, we regridded the 1°×1° GEIA emissions from soils under natural vegetation and fertilized agricultural fields to generate 0.1° natural forest emissions, including only natural forest pixels based on the MODIS-derived natural forest map (see Appendix J). The prior N_2O emission from natural forest is 2.2 Gg N_2O/yr, which is 4.6% of the state total anthropogenic N_2O from our prior emission inventory. Similarly, US EPA estimates forest soil emissions are less than 1% [US EPA, 2015]. We also used ocean N_2O emissions from the GEIA model [Bouwman et al., 1995] to incorporate emissions from the ocean (e.g., upwelling) along the California coast to the inversion system. The total ocean N_2O emission from the GEIA model within our entire modeling domain over the large region in the Pacific Ocean (see Appendix K) is 60 Gg N_2O/yr, which is 1.2 times the prior anthropogenic emission used in this study (48.3 Gg N_2O/yr).

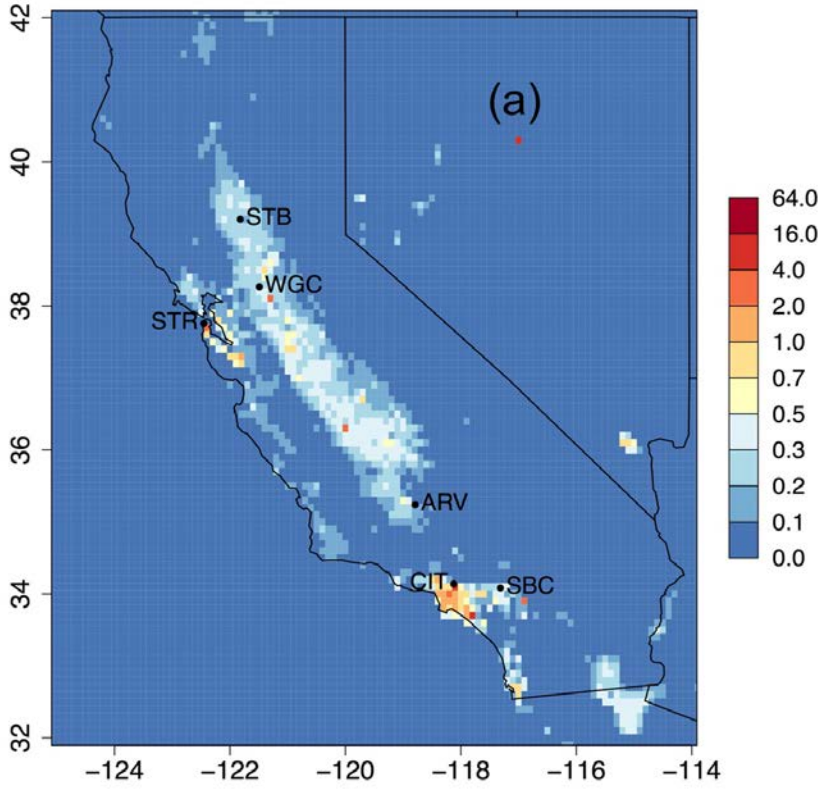

Figure 11. The total anthropogenic prior N_2O emissions (nmol/m^2/s) used for inverse modeling (state total = 48.3 Gg N_2O/yr) with locations of measurement sites across California.

Table 8. Annual Anthropogenic Prior N_2O Emissions by Region and Sector (Gg N_2O/yr)

Sector[a]\ Region[b]	SD (14)	SS (13)	SC (12)	MD (10)	SCC (11)	SJV (8)	NCC (9)	GBV (6)	SF (7)	MC (4)	SV (3)	NC (2)	LC (5)	LT (15)	NEP (1)	Sector Total
AGS	0.14	0.58	0.21	0.36	0.96	6.70	0.67	0.25	0.77	0.46	3.11	0.37	0.06	0.00	0.65	15.30
MNM	0.06	0.62	0.17	0.82	0.36	4.97	0.32	0.05	0.33	0.42	0.68	0.27	0.02	0.00	0.42	9.53
AWB	0.00	0.01	0.00	0.00	0.01	0.07	0.01	0.00	0.01	0.01	0.03	0.00	0.00	0.00	0.01	0.17
IPU	0.63	0.03	5.57	0.06	0.18	1.30	0.06	0.00	1.48	0.01	0.40	0.00	0.00	0.00	0.00	9.73
EMT	0.02	0.00	0.11	0.01	0.01	0.07	0.01	0.00	0.05	0.00	0.02	0.00	0.00	0.00	0.00	0.30
IDE	0.01	0.01	0.01	0.03	0.01	0.03	0.01	0.01	0.01	0.01	0.02	0.01	0.00	0.00	0.01	0.18
N2O	0.04	0.17	0.06	0.10	0.28	1.92	0.19	0.07	0.22	0.13	0.89	0.11	0.02	0.00	0.19	4.40
OPR	0.00	0.00	0.00	0.00	0.00	0.00	0.00	0.00	0.00	0.00	0.00	0.00	0.00	0.00	0.00	0.00
RCO	0.01	0.00	0.04	0.01	0.01	0.02	0.00	0.00	0.03	0.01	0.01	0.00	0.00	0.00	0.00	0.15
WST	0.25	0.01	1.54	0.02	0.06	0.18	0.03	0.00	0.59	0.00	0.16	0.00	0.00	0.00	0.00	2.85
TNR	0.01	0.01	0.02	0.03	0.01	0.03	0.00	0.00	0.01	0.01	0.02	0.00	0.00	0.00	0.01	0.17
TRO	0.28	0.15	0.83	0.44	0.26	0.87	0.18	0.14	0.57	0.42	0.75	0.28	0.05	0.01	0.28	5.50
Region Total	1.44	1.59	8.58	1.89	2.15	16.18	1.48	0.54	4.08	1.47	6.08	1.06	0.15	0.02	1.58	48.29

[a] Sectors include agricultural soils (AGS), manure management (MNM), agricultural waste burning (AWB), industrial processes and product use (IPU), energy manufacturing transformation (EMT), indirect emissions from NOx & NH_3 (IDE), indirect N_2O emissions from agriculture (N2O), oil production & refineries (OPR), buildings (residential & others) (RCO), waste (solid & wastewater) (WST), non-road transportation (TNR), road transportation (TRO).

[b] The number in the parentheses shows the region number shown in Figure 3.

2.8.3. Hierarchical Bayesian Inversion

We use a similar hierarchical Bayesian inversion method to that of CH_4 to estimate regional N_2O emissions in California. As in the inversion for CH_4, we use the following linear model for estimating scaling factors for regional emissions

$$\mathbf{y} = \mathbf{K}\boldsymbol{\lambda} + \mathbf{v} \qquad (19)$$

where **y** is the measurement vector ($n \times 1$), which represents 3-hourly local mixing ratio time series after subtracting background values, $\mathbf{K} = \mathbf{FE}$ (an $n \times k$ matrix), **F** is the footprint ($n \times m$), **E** is the prior emission ($m \times k$), **λ** is a $k \times 1$ vector for scaling factors with a covariance matrix **Q** ($k \times k$), and **v** is a vector representing the model-measurement mismatch with a covariance matrix **R** ($n \times n$). Note that the original **K** matrix was prepared at 0.1° resolution, which is the same as that of the prior emission map and was aggregated into 0.3° resolution for inversion. We solve for **λ** with a dimension of 197×1 which includes 183 pixels (at 0.3°×0.3°) for the major regions (i.e., SV, SJV, SF and SC), 11 non-major regions inside California, outside California for non-ocean anthropogenic emissions, natural forest and ocean regions. Here, we combined all 0.3° pixels for each non-major region (e.g., Region 1) into one region as in Jeong et al. [2013] to reduce the number of parameters. Given the data (i.e., measured N_2O mixing ratios), solving for **λ** based on the HBI method and multiplying it by **E**, we obtain posterior (optimized) emissions.

As in the inversion for CH_4, we estimate the following joint parameters with the same definition and the details are described in Section 2.7.3.

$$\boldsymbol{\Theta} = \{\boldsymbol{\lambda}, \boldsymbol{\mu_\lambda}, \boldsymbol{\sigma_\lambda}, \boldsymbol{\sigma_R}, \eta, \tau\} \qquad (20)$$

Figure 12 shows the estimated model-data mismatch uncertainty (square root of the diagonal components of **R**) for the four sites which have continuous measurements during most of the study period. Recall that the model-data mismatch uncertainty is also estimated because all the parameters in the set **Θ** in Equation 20 including the scaling factor ($\boldsymbol{\lambda}$) are optimized simultaneously by HBI. Jeong et al. [2012b] estimated the model-data mismatch uncertainty for the WGC site by explicitly calculating errors due to transport, background and other sources (see Appendix G and Jeong et al. [2012b] for details). This estimate for **R** from Jeong et al. [2012b] is used as our existing "prior" information to estimate posterior **R** in this study. The prior values for WGC in the figure are taken from Jeong et al. [2012b]. The prior values for the other sites are assigned in proportion to the relative background-subtracted mean mixing ratio to that of WGC. The posterior uncertainty values (sampled from the posterior distribution using HBI) are generally similar to the prior values although there are some variations depending on season and site. The result at WGC suggests that the explicit estimates of the model-data mismatch uncertainty in Jeong et al. [2012b] are comparable to our posterior estimates. We note that the prior is different from the posterior for some cases (e.g., August at CIT). This is because we use a vague (long-tailed) distribution for the hyper-parameter for the model-data mismatch uncertainty parameter (i.e., $\boldsymbol{\sigma_R}$) and the data derive different values from the prior (see Appendix L for posterior distributions for $\boldsymbol{\sigma_R}$). Also, the uncertainty for the prior (i.e., diagonal terms in **Q**) is estimated and presented in Appendix L. For the major emitting regions (3, 7, 8 and 12), the region average of the prior uncertainties for individual pixels is estimated to be ~150%, which is higher than the prescribed 100% in Jeong et al. [2012b] (see Appendix L). We note that by conducting pixel-based inversions that allow adjustment of emissions for individual pixels within major emitting regions, prior uncertainties for individual pixels are likely higher than those for entire regions used in Jeong et al. [2012b].

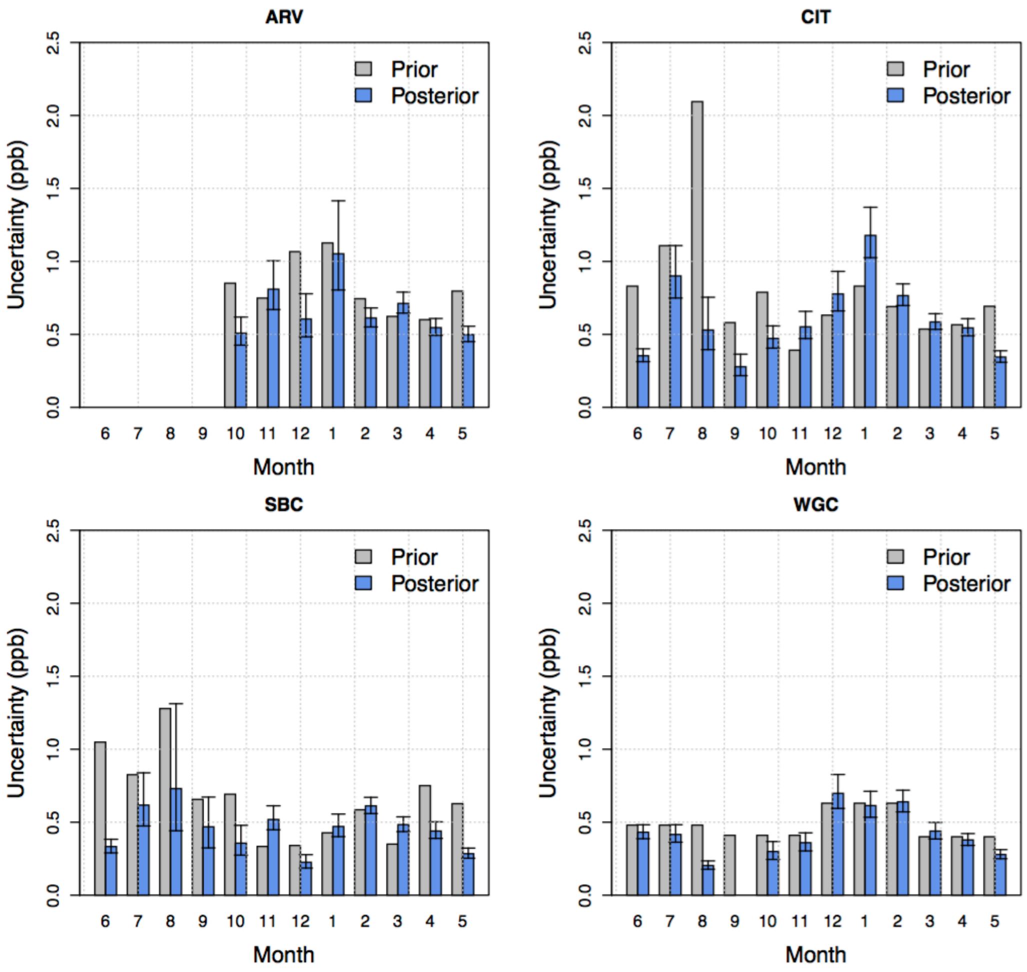

Figure 12. Estimated (posterior) model-data mismatch uncertainty for N_2O inversions at four major sites with continuous measurements during most of the study period. The posterior values were estimated using 50000 MCMC samples and the error bar represents the 68% confidence interval. The uncertainty value for September at WGC was not estimated because measurements were missing during most of the month.

3. Results and Discussion

3.1. Assessment of Transport Model

Atmospheric inverse estimates of gas emissions from the land surface typically depend on transport model predictions, hence driving a need to assessment of uncertainties in the transport model. In this section we assess the uncertainty in WRF-STILT transport model predictions using a combination of meteorological and carbon monoxide (CO) measurements.

3.1.1. Evaluation of Meteorology Errors

There are several regions of California that are of particular importance in terms of magnitude of GHG emissions. These include California's largest urban areas of the San Francisco Bay Area (SFBA), and the Southern California air basin (SoCAB; which encompasses Los Angeles). Also, extensive agriculture in the Central Valley (CV) has been shown to generate significant emissions of GHGs associated with livestock and fertilizer (e.g. CH_4, NO_2; [Jeong et al., 2012a; 2012b; 2013]). Therefore, it is of particular importance to model these regions accurately, and account for errors in boundary layer meteorology. The first column of Figure 13a shows 0 - 2000 m daytime mean monthly values of σ_u (i.e., random error for boundary layer wind, see Section 2.5.3), and the monthly mean errors of WRF wind speed relative to observations (i.e., WRF – observation) using data from the Sacramento profiler in the CV, the Irvine profiler in SoCAB, and the Oakland radiosonde station in the SFBA (see Figure 6 for the wind profiler sites associated with individual GHG sites). We note that some sites (e.g., Arvin) may not be well-represented by the closest available wind profiler, potentially resulting in undiagnosed transport errors. For this reason, we compare measured and predicted CO signals as a further diagnostic to help quantify errors. These stations were selected based on their location and data availability from June 2013 – May 2014. Additionally, Table 9 presents the seasonal mean and random error (represented by the standard deviation of model − observation error) of wind speed, wind direction, and boundary layer height representative of each GHG site. These error statistics were calculated using data from WRF-STILT meteorology and observations from the profiler or radiosonde site nearest to the associated GHG site. There are several inferences that could be made from Figure 13. First, the magnitude of the random error (σ_u) was considerably larger than the magnitude of the mean error. The only exception to this was July in SFBA, which was likely partially due to limited numbers of daytime radiosondes launched during this month and WRF not properly capturing a synoptic event early in the month. The fact that the magnitude of random error was considerably larger than the mean error reiterates a similar result obtained by Lin and Gerbig [2005] using radiosonde observations across the Continental United States. Also, for the majority of sites and months the magnitude of the mean error was less than the assumed 1 m s^{-1} accuracy of observational winds in the boundary layer. Mean model errors smaller than 1 m s^{-1} were considered to be undetectable. Additionally, the random error, σ_u, tended to be smallest during the summer. This was due to relatively strong and stable zonal winds during these months.

Finally, inspection of histograms confirmed that the wind errors were approximately Gaussian about the mean.

One limitation of using wind speed as an assessment of meteorology is that its scalar nature does not account for errors in wind direction. Errors in WRF wind direction can lead to erroneous STILT particle trajectories, and hence unrealistic emission footprints that may not properly sample prior emissions in the presence of sharp gradients in GHG emissions (such as near edges of urban areas or along major highways). The second column of Figure 13b shows the mean directional error (in degrees) and the standard deviation of wind direction error (σ_{dir}) for the three stations described above. Unlike the CV and SFBA area sites, σ_{dir} at the SoCAB site did not exhibit clear seasonality. Instead it had consistent values of 60~80°, whereas σ_{dir} of the CV and SFBA sites ranged from ~50-60° during the winter to ~10-30° during the summer. At all sites the mean directional error was small relative to the random error.

For z_i (boundary layer depth) the discrepancy between the magnitude of the mean error and the random error was not as clear as for wind speed (Figure 13, third column). In this case, the mean error was comparable in magnitude to the random error (σ_{zi}), and in some cases such as February and March 2014 for the Sacramento profiler, the mean error exceeded σ_{zi}. Also, similar to the model-data errors in wind speed discussed above, errors in z_i did have some seasonality associated with them. February – May commonly exhibited the greatest mean and random errors across observational sites, while during July-August mean and random errors in z_i were at a minimum. However, due to the relatively low number of boundary layer height observations available the significance of this difference was difficult to assess. Seasonally similar results were obtained at other sites as well (Table 9). Finally, it was not uncommon for the mean errors to be greater than the assumed 200 m accuracy of z_i measurements. For our study, this brings into question the validity of the assumption in Gerbig et al. [2008] that the mean error can be neglected, and is a potential source of error.

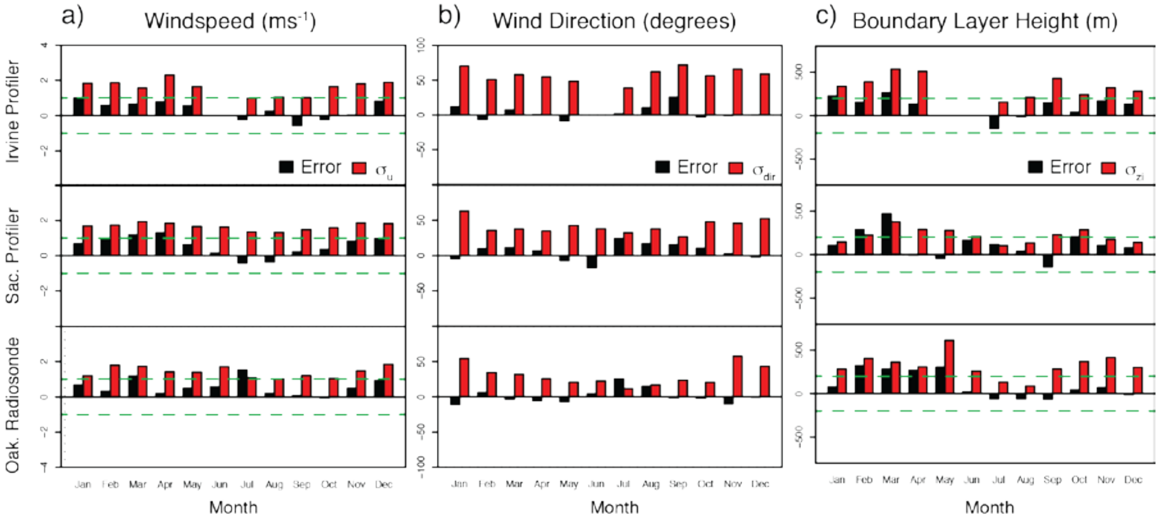

Figure 13. Monthly mean (black bars) and random (red bars) error for wind speed (a; ms-1), wind direction (b; degrees), and afternoon (1200-1700 LST) boundary layer height (c; m) for Irvine, Sacramento, and Oakland stations. Wind speed and wind direction errors are calculated from 0-2000m. The green dashed line indicates the assumed measurement uncertainty.

Table 9. Mean Seasonal Meteorological Model Error (WRF - observation) for Wind Speed, Wind Direction, and Boundary Layer Height (z_i) for Each GHG Tower

	DJF			MAM			JJA			SON		
GHG Tower	Windspeed	Wind Direction	z_i	Windspeed	Wind Direction	z_i	Windspeed	Wind Direction	z_i	Windspeed	Wind Direction	z_i
Arvin (ARV)	.02 (2.48)*	-4.9 (60.1)	31 (346)	-.12 (2.18)	0.9 (45.4)	38 (444)	.28 (1.44)	0.5 (44.6)	-103 (355)	-.18 (1.75)	3.8 (56.7)	176 (374)
Pasadena (CIT)	.07 (2.16)	-5.7 (75.7)	-282 (327)	.44 (2.00)	-5.4 (51.5)	-239 (346)	0.45 (1.07)	-9.7 (81.7)	-85 (142)	-.34 (1.89)	-3.8 (84.2)	-149 (289)
Madera (MAD)	.02 (2.48)	-4.9 (60.1)	31 (346)	.34 (1.94)	-3.7 (31.6)	224 (366)	-.20 (1.35)	1.9 (37.3)	160 (260)	-.44 (1.97)	9.4 (41.3)	95 (294)
Mt. Wilson (MTW)	.07 (2.16)	-5.7 (75.7)	-282 (327)	.44 (2.00)	-5.4 (51.5)	-239 (346)	0.45 (1.07)	-9.7 (81.7)	-85 (142)	-.34 (1.89)	-3.8 (84.2)	-149 (289)
Scripps, La Jolla (SIO)	-.28 (1.36)	-8.6 (46.4)		-.22 (1.74)	4.6 (34.3)		-.12 (1.25)	18.7 (34.0)		-.51 (1.13)	-.8 (52.9)	
Sutter Buttes (STB)	.45 (2.84)	8.3 (60.3)	196 (262)	.58 (2.39)	.7 (41.5)	382 (528)	-.63 (2.38)	9.3 (51.4)	263 (225)	-.02 (2.42)	8.3 (56.1)	208 (337)
San Francisco (STR)	.64 (1.62)	-13.0 (44.0)	128 (330.3)	1.05 (1.56)	-4.6 (22.7)	122 (322)	.77 (1.27)	14.8 (17.1)	-34 (161)	.17 (1.24)	-4.1 (34.0)	16 (356)
Sunnyvale (SVL)	.64 (1.62)	-13.0 (44.0)	128 (330.3)	1.05 (1.56)	-4.6 (22.7)	122 (322)	.77 (1.27)	14.8 (17.1)	-34 (161)	.17 (1.24)	-4.1 (34.0)	16 (356)
Trinidad (THD)	-.19 (2.23)	-11.3 (73.9)		-1.93 (2.92)	-3.4 (48.8)		-.96 (2.73)	2.7 (48.2)		-.78 (2.11)	-.8 (61.9)	
Tranquility (TRA)	.02 (2.48)	-4.9 (60.1)	31 (346)	.34 (1.94)	-3.7 (31.6)	224 (366)	-.20 (1.35)	1.9 (37.3)	160 (260)	-.44 (1.97)	9.4 (41.3)	95 (294)
Tuscan Buttes (TSB)	-.45 (2.64)	-11.8 (61.0)		-.60 (2.44)	-10.9 (40.2)		-.77 (1.70)	-2.2 (51.5)		-.44 (2.44)	-4.2 (41.2)	
Victorville (VTR)	1.23 (2.34)	-7.0 (47.0)	-16.8 (359)	.61 (1.75)	-2.3 (35.4)	84 (500)	.05 (1.29)	4.0 (48.7)	64. (281)	.32 (1.98)	-5.3 (57.8)	195 (529)
Walnut Grove (WGC)	.86 (1.75)	1.1 (50.6)	155 (170)	1.0 (1.8)	3.6 (38.7)	140 (232)	-.21 (1.4)	8.0 (36.3)	105 (156)	.46 (1.65)	9.3 (40.3)	56 (230)
San Bernardino (SBC)	1.23 (2.34)	-7.0 (47.0)	-16.8 (359)	.61 (1.75)	-2.3 (35.4)	84 (500)	.05 (1.29)	4.0 (48.7)	64. (281)	.32 (1.98)	-5.3 (57.8)	195 (529)

*Values in parentheses are the seasonal standard deviation of the error and represent its random component. Sufficient representative z_i observations were not available for SIO, THD, and TSB.

For CO, emissions are dominated by the major urban centers in SoCAB and SFBA, and relatively small amounts of CO are emitted by agriculturally dominated portions of the state such as the Central Valley. Therefore, ensuring that the WRF-STILT model is accurately simulating the dynamic shifts in meteorological conditions in these regions is vital. Figure 14 shows June 2013 - May 2014 timeseries of surface wind speed and direction for SoCAB and SFBA, and scatterplots of simulated versus observed boundary layer heights using WRF-STILT parameterized with MYNN2-NOAH. For both SoCAB and SFBA regression analysis indicates slopes of simulated versus observed z_i are within 0.1 of unity (0.94 ± 0.04 for SoCAB; 0.90 ± 0.03 for SFBA) with relatively small positive offsets ~130 m and R^2 values of 0.28 and 0.45, respectively. Additionally, inspection of simulated wind speed and direction relative to surface station observations revealed that WRF-STILT was capturing both seasonal changes and synoptic shifts in surface winds. Combined, these results give confidence that WRF-STILT was sufficiently simulating meteorological transport of emissions in these key regions.

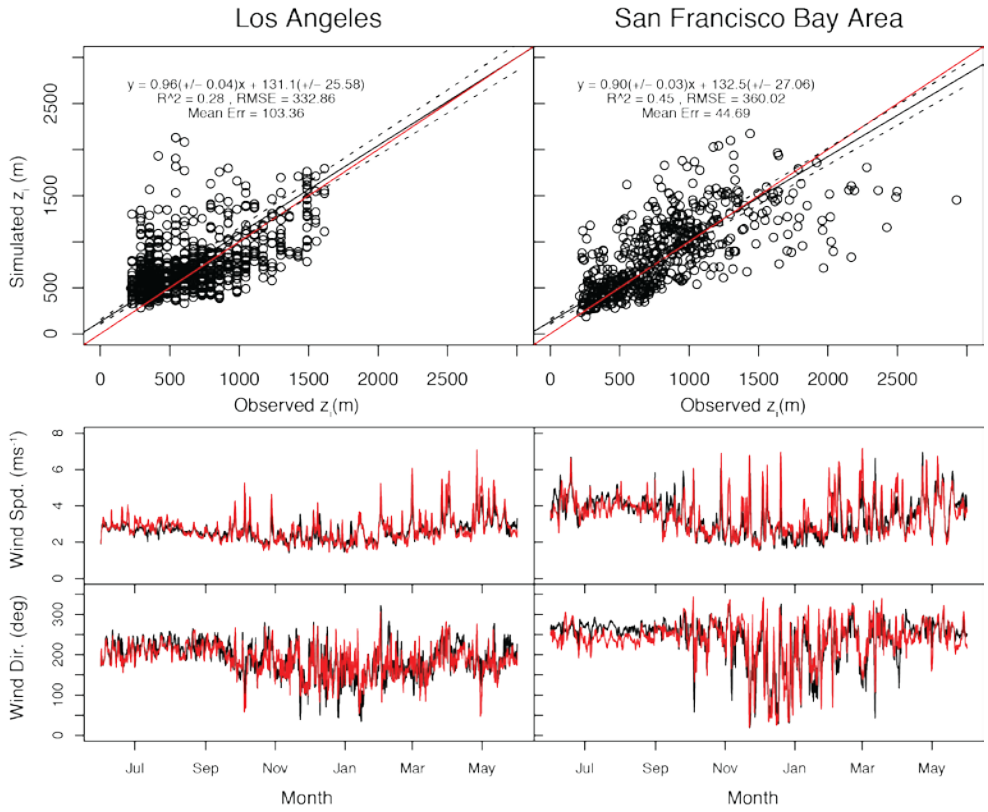

Figure 14. (Top) Simulated and observed z_i (1200-1700 LST) scatterplot for Los Angeles (left) and San Francisco Bay Area (right) using Irvine profiler and San Jose State University (SJSU) lidar, respectively. z_i from Irvine was available intermittently from June 2013 – April 2014. SJSU z_i data was available from December 2013 - May 2014. The red line indicates the 1:1 line. (Bottom) June 2013 - May 2014 timeseries of simulated (red line) and observed (black line) surface wind speed and direction at surface stations within 50 km of CIT (left) and STR (right).

Following the variogram method of Lin and Gerbig [2005] and Gerbig et al. [2008] we estimated daytime wind error correlation statistics for California using available wind profiler and radiosonde observations between 2010 - 2014. We derived annual mean estimates of temporal and horizontal error correlation length scales for boundary layer winds across California by fitting exponential variograms to boundary layer wind error residuals over time and space. We found the mean spatial correlation length scale to be approximately 120 km, which is similar to that reported by Lin and Gerbig [2005]. However, the error correlation timescale of horizontal boundary layer winds was calculated to be ~3.5 hours, longer than the ~2.6 hours reported by Lin and Gerbig [2005]. The spatial and temporal coverage of available concurrent z_i observations was insufficient to adequately estimate z_i error characteristics. In the absence of sufficient z_i observations we assumed z_i temporal and spatial correlation to be represented by statistics previously derived from continental-scale radiosonde data reported in Gerbig et al. [2008].

3.1.2 Seasonal WRF-STILT CO Predictions and Optimization of WRF Parameterization

At ARV, CIT, SBC, and WGC we assessed the accuracy by which WRF-STILT reproduced the observed hourly CO mixing ratios, surface winds, and boundary layer heights (where available) for June 2013 – May 2014. As described in Section 2.5, this was done with a combination of WRF parameterizations for the atmospheric boundary layer (MYNN2 and YSU) and land surface (NOAH and 5-L LSM) that differed by month. During April – September irrigation is prevalent in large portions of California's agricultural regions such as the Central Valley. Multiple studies have shown that the presence of irrigation can significantly alter the surface energy balance and influence boundary layer properties including the height of the boundary layer [Kueppers and Snyder, 2007; Sacks et al., 2009; Sorooshian et al., 2011; Bagley and Miller, 2015]. However, irrigation was absent in the version of the NOAH land surface model used in this study, which likely led to unrealistic representations of boundary layer height in central California during the growing season (approximately April – September). This necessitated the use of the 5-L LSM (which simulates irrigation) at ARV where the observational CO footprint was strongly influenced by irrigated agricultural regions throughout California's Central Valley. WGC is also located in the Central Valley in a region of extensive irrigation. As shown in Figure 15, using NOAH at this site led to higher than observed local boundary layer heights during the start of the growing season. However, the combination of CO having limited emissions from agricultural areas such as the Central Valley (see Figure 6 for regions), and surface winds at WGC being typically strong (~4 – 6 m/s) and zonal during the growing season relative to other portions of the year, likely led to the CO footprint of the tower extending outside the region of primary irrigation, and hence be better represented by WRF using the NOAH land surface parameterization for WGC. This suggests that future work in the Central Valley using the NOAH land surface model would benefit by the addition of an irrigation scheme similar to methods used in several prior studies [Sorooshian et al., 2011; Harding and Snyder, 2012].

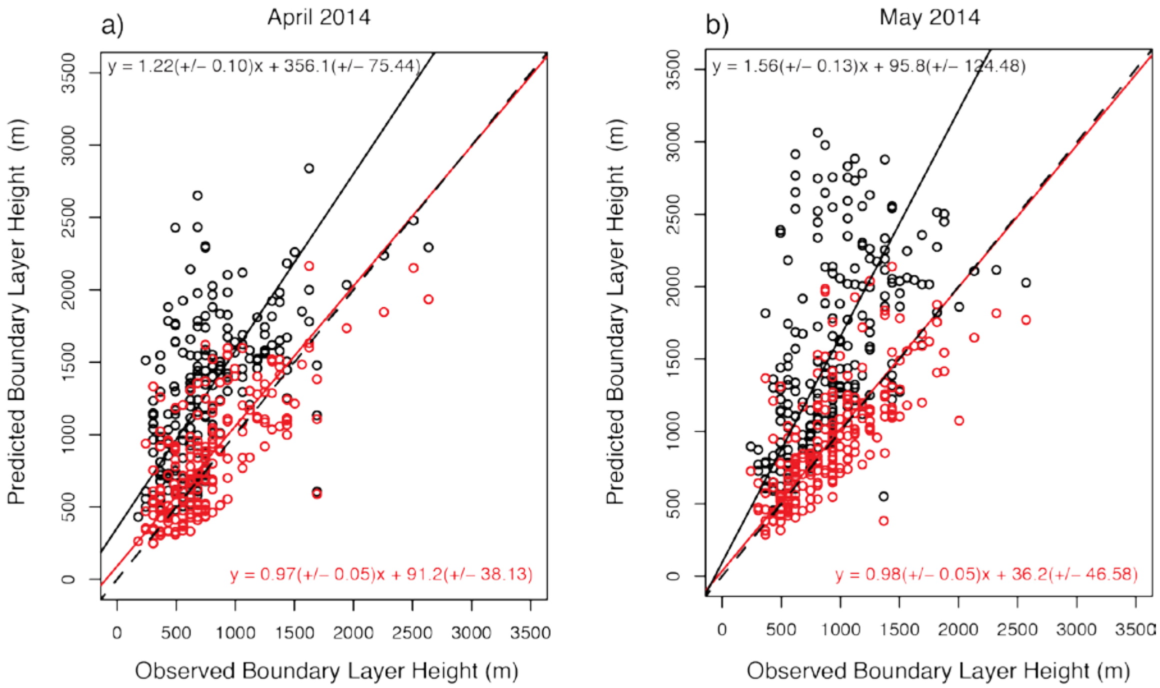

Figure 15. Scatterplot of predicted and observed boundary layer height at Sacramento profiler near WGC for April (left) and May (right). Red points represent results using the 5-L LSM land surface parameterization in WRF, and black points represent results from the NOAH land surface parameterization in WRF. The dashed line indicates 1:1 correlation.

WRF-STILT simulations using the MYNN2 boundary layer scheme strongly underestimated CO at ARV and SBC sites during October – January (now shown). This period tended to be when WRF simulations had the largest errors in boundary layer winds and boundary layer height relative to observed meteorological conditions. Additionally, SBC and ARV are located in regions with extensive topography, with ARV being located at the southern end of a valley with topography that may have had a weak representation in WRF. Near SBC the MYNN2 boundary layer parameterization overpredicted surface wind speed, which led to an under-prediction of CO at the tower (Figure 16). This was likely due to air parcels moving too quickly over regions of high CO emissions to sample them realistically. Replacing MYNN2 with the YSU boundary layer scheme enabled a WRF parameterization designed to improve the representation of topographic effects. Using the YSU scheme with topographic effects at ARV and SBC improved the model representation of near surface wind speed, and correspondingly improved predictions of CO for ARV and SBC during November - January. Figure 16 shows the comparison between MYNN2 and YSU CO and surface wind speed for November – January at SBC. However, the YSU boundary layer scheme performed poorly relative to MYNN2 for CIT and WGC. This indicated that for regions with large heterogeneity such as California, a single model configuration is unlikely to be ideal for all seasons and locations. Table 10 gives the WRF boundary layer and land surface schemes found to best reproduce meteorological conditions and CO signals at each tower for each month, and were used for the remainder of this study.

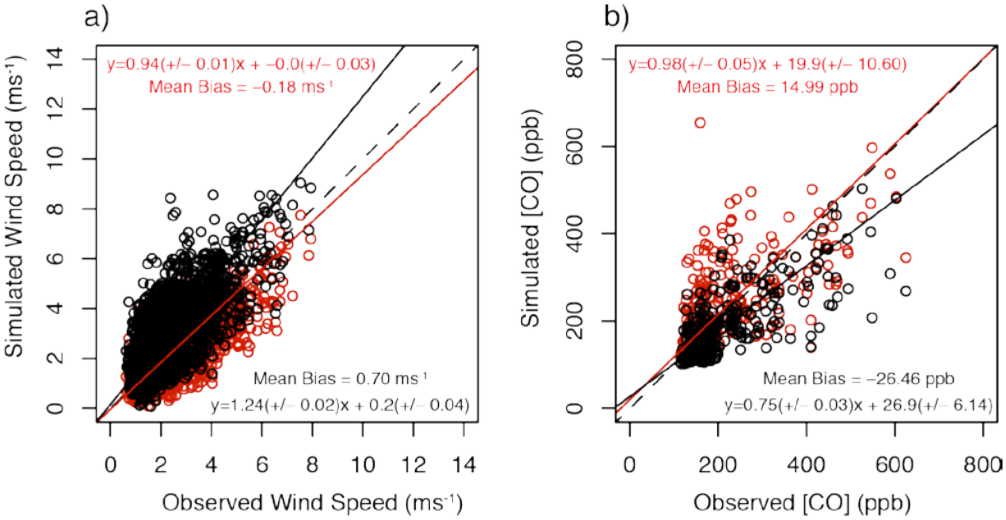

Figure 16. Daytime comparison at SBC between surface wind speeds (left) and CO (right) for November – January YSU (red) vs. MYNN2 (black) near the SBC tower.

Table 10. WRF PBL and Surface Scheme Combination for CO Predictions at ARV, CIT, SBC, and WGC during June 2013 - May 2014

	ARV	CIT	SBC	WGC
June	NA*	MYNN2-NOAH	MYNN2-NOAH	MYNN2-NOAH
Jul	NA	MYNN2-NOAH	MYNN2-NOAH	MYNN2-NOAH
Aug	NA	MYNN2-NOAH	MYNN2-NOAH	MYNN2-NOAH
Sep	NA	MYNN2-NOAH	MYNN2-NOAH	NA
Oct	MYNN2[a]-NOAH[b]	MYNN2-NOAH	MYNN2-NOAH	MYNN2-NOAH
Nov	YSU[c]-NOAH	MYNN2-NOAH	YSU-NOAH	MYNN2-NOAH
Dec	YSU-NOAH	MYNN2-NOAH	YSU-NOAH	MYNN2-NOAH
Jan	YSU-NOAH	MYNN2-NOAH	YSU-NOAH	MYNN2-NOAH
Feb	MYNN2-NOAH	MYNN2-NOAH	MYNN2-NOAH	MYNN2-NOAH
Mar	MYNN2-NOAH	MYNN2-NOAH	MYNN2-NOAH	MYNN2-NOAH
Apr	MYNN2-5-L LSM[d]	MYNN2-NOAH	MYNN2-NOAH	MYNN2-NOAH
May	MYNN2-5-L LSM	MYNN2-NOAH	MYNN2-NOAH	MYNN2-NOAH

*"NA" indicates that CO observations were not available during that month.

[a] Nakanishi and Niino [2006]

[b] Chen and Dudhia [2001]

[c] Hong et al. [2006]

[d] Ruiz et al. [2010]

Using the model configurations in Table 10 we seasonally analyzed the predicted CO mixing ratio at ARV, CIT, SBC, and WGC for Summer 2013 - Spring 2014. We used a seasonal timescale to minimize the impacts of potential modeling biases of individual synoptic meteorological events that can negatively influence CO predictions for several days and dominate error statistics over shorter time periods. This was particularly relevant for CO as its sources were primarily constrained to relatively small regions of large anthropogenic influence such as cities and roads. Therefore small errors in footprint estimation due to short-term meteorological errors can easily underestimate emission sources contributing to observed CO at a tower. The mean error of WRF-STILT predicted CO normalized by mean observed CO is summarized for all sites and seasons in Table 11. During all seasons the mean CO mixing ratios at SBC and CIT were typically large relative to WGC and ARV due to their close proximity to the Greater Los Angeles metropolitan area.

Table 11. Mean Seasonal CO Prediction Error (ppb) at ARV, CIT, SBC and WGC

Month \ Site	ARV	CIT	SBC	WGC
JJA	NA	17.8 (9.7) (± 6.6)	-22.0 (15.1) (± 6.0)	9.5 (45.9) (± 2.3)
SON	-22.6 (41.8) (± 5.3)	22.4 (13.8) (± 10.4)	-17.5 (12.0) (± 11.2)	-12.5 (25.3) (± 3.6)
DJF	-0.5 (1.1) (± 5.0)	-9.7 (3.9) (± 17.9)	-3.4 (2.8) (± 8.9)	1.6 (2.7) (± 5.6)
MAM	3.9 (17.8) (± 2.0)	5.4 (3.8) (± 7.9)	-16.4 (19.0) (± 5.4)	4.7 (37.9) (± 1.9)

*Values in parentheses (top row in each season) represent the mean error as a percentage of the seasonal mean background subtracted CO mixing ratio. The 68% confidence level uncertainty of the mean error is also reported (in parentheses; bottom row).

At CIT, SBC, and WGC during June-August of 2013 (ARV CO observations were unavailable during this period) the predicted and observed CO signals (Figure 17) were small relative to fall and winter (Figures 18 and 19). In June and July there were multiple periods of potential wildfire influence at the southern-most sites (SBC and CIT), which were excluded from the analysis (magenta triangles in Figure 17). However, with the exception of July and late August for SBC only small fractions of these months failed to satisfy our criteria for parcels sampling background conditions at 130°W. In the periods when predictions of CO were retained (open green circles in Figures 17 - 20), the magnitudes of mean error of predicted CO at CIT, SBC, and WGC were 10 - 22 ppb (Table 11). However, the sign of the errors in CO were not consistent across sites, with simulations overpredicting CO at CIT and WGC, and underpredicting CO at SBC. As shown below, the underprediction of CO at SBC was consistent across all seasons. At CIT and SBC, removing background CO and normalizing the prediction error of CO by the mean observed CO led to errors in predicted CO between 9 - 15% of the background-subtracted observed CO during summer of 2013. However at WGC, the fractional prediction error was much larger. Strong zonal winds and tall boundary layer heights contributed to CO mixing ratios that were typically small (~20 ppb) when background contributions to CO were removed. Therefore, the mean prediction error of CO at WGC (9.5 ppb) represented a 46% prediction error when background CO was removed.

However, regression analysis of WRF-STILT CO predictions revealed that they were generally consistent with observations based on the slope of the line of best fit between predicted and observed CO. The slopes (predicted/observed CO) were close to 1 (within 0.2) with values of 0.82 at SBC, 0.89 at CIT, and 0.96 WGC. The uncertainties associated with these slopes were ±0.12 at SBC, ±0.04 at CIT, and ±0.06 at WGC. At WGC and CIT, regression slopes near unity, small mean bias, and small slope uncertainty indicated that WRF-STILT accurately captured both the dynamics and mean mixing ratio of CO for these sites during summer of 2013. However, at SBC the combination of small mean error in CO, relatively large uncertainty of the regression slope, and a small R^2 value of 0.08 led to the conclusion that although WRF-STILT was reproducing the mean seasonal CO mixing ratio at SBC, the seasonal variations may not have been sufficiently captured by our simulations.

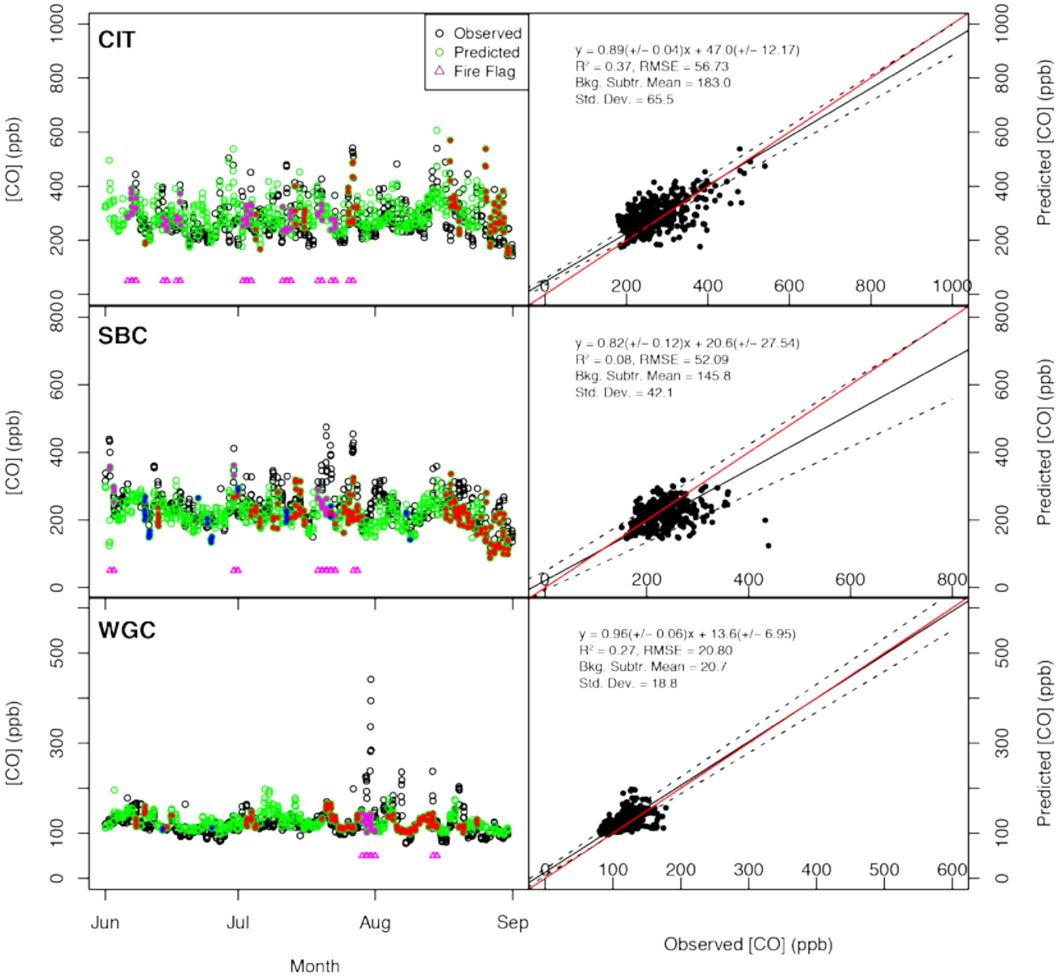

Figure 17. June 2013 – August 2013 timeseries and regression for CIT (top), SBC (middle), and WGC (bottom). Green circles represented predicted CO mixing ratios and black circles represent observations. Filled circles indicate that the data was excluded from the regression analysis due to insufficient particle trajectories reaching 130°W (red fill), poor WRF representation of meteorology (blue fill), or wildfire (magenta fill, and triangles).

Figure 18 compares the predicted and observed CO mixing ratios at ARV, CIT, SBC, and WGC for September - November (SON) of 2013. During the fall, a combination of changes in wind direction, intermittently low wind speeds, and small daytime boundary layer depths produced mean CO mixing ratios significantly larger than those found during the summer of 2013. However, the periods of highest CO also tended to be during periods when the background sampling criteria were not met, typically due to either very stagnant air masses over California, or meteorological conditions transporting continental instead of Pacific air to the GHG towers. This was particularly prevalent at CIT and SBC. Wildfires were not factors during the fall at any sites, with the exception of short periods at SBC and WGC during October. Analysis of regression between observed and predicted CO revealed strong relationships during SON of 2013. At CIT and SBC the regression slopes were close to one with small uncertainty (1.05 ± 0.07 for CIT; 0.99 ± 0.08 for SBC). However, at WGC and ARV the slopes and mean prediction errors (Table 11) indicated WRF-STILT underpredicted CO mixing ratios at these sites. This was particularly noticeable at ARV where complex topography likely contributed to a mean prediction error of CO which was 23 ppb lower than observed and the slope of the regression line was 0.71 (± 0.06).

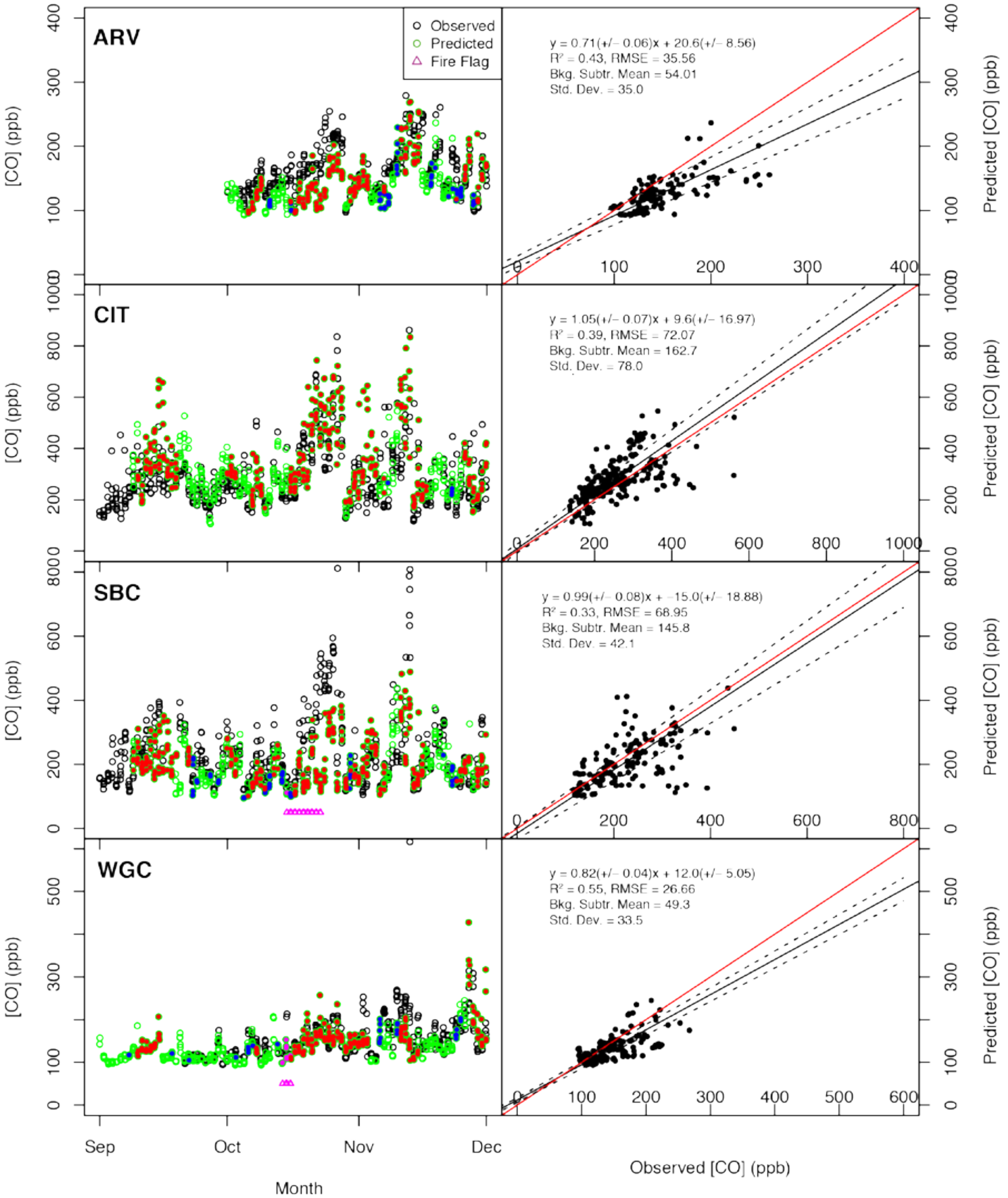

Figure 18. Same as Figure 15, but for September 2013 – November 2013. Additionally, ARV is included in the top row.

Similar to fall, the winter months of December 2013-February 2014 (DJF) had large predicted and observed CO relative to spring and summer (Figure 19). Despite the large CO mixing ratios, the mean prediction error was small at all sites and ranged from -9.7 at CIT to 1.6 ppb at WGC. When normalized by the mean background-subtracted observed

CO, these represented mean errors of only 1-4%. However, inspection of the CO timeseries and regression (slope of 0.81 ± 0.09 partially offset by high intercept of 27.7ppb ± 14.89ppb) at ARV indicated that there remained some difficulties in properly simulating CO and transport at this site during this season. We excluded periods of southeasterly winds at ARV between November 2013 and January 2014 as these were identified as periods which strongly underpredicted CO regardless of the WRF boundary layer or land surface model used. This exclusion occurred during a significant fraction of the winter season (blue-filled circles in Figure 19). The source of this underprediction remains undiagnosed as errors in regional surface wind speed and direction were not obviously biased during these periods, although these periods did typically correspond to times with slow moving stagnant air in the region. This requires further analysis, and it is possible that this issue may be influencing periods that were not identified by our crude exclusion of southeasterly winds from November - January at ARV. SBC exhibited a similarly low regression slope (0.82 ± 0.03), but this result did not include the extensive exclusion of data as at ARV. At CIT, SBC, and WGC this was not an issue as evidenced by inspection of the timeseries, small mean error in CO predictions, regression slopes close to one with small uncertainties (~ ±0.05), and relatively large R^2 values for the regression (0.35 at CIT, 0.47 at SBC, and 0.45 at WGC).

During spring (March – May) tall boundary layer heights and strong zonal winds contributed to small CO mixing ratios at all sites relative to previous months (Figure 20). Additionally, shifts in prevailing winds and the absence of wildfires contributed to only a small fraction of the CO predictions requiring exclusion. With the exception of SBC, seasonal mean CO was overpredicted by 4 - 5ppb across all sites. At SBC seasonal mean CO was again underpredicted (-16.4ppb). Also, at all sites the regression slopes were less than unity and ranged from 0.75 (± 0.04) at WGC to 0.90 (± 0.05) at CIT. However, as discussed in the following section, small CO mixing ratios at ARV and WGC during these months may have led to small errors in background estimates of CO exerting relatively large influences on regression results.

Although problematic periods remain, the combination of seasonal biases in predicted CO typically smaller than 15 ppb, and slopes of regression lines within 0.20 of unity (with uncertainty) for most sites and seasons lends confidence to WRF-STILT’s ability to accurately predict CO and hence other GHG’s at our observational towers. However, several sources of potential uncertainty remain in the predictions of CO including random error in the transport model, uncertainty in the background curtain, and potential limitations in the bottom-up estimates of CO emissions.

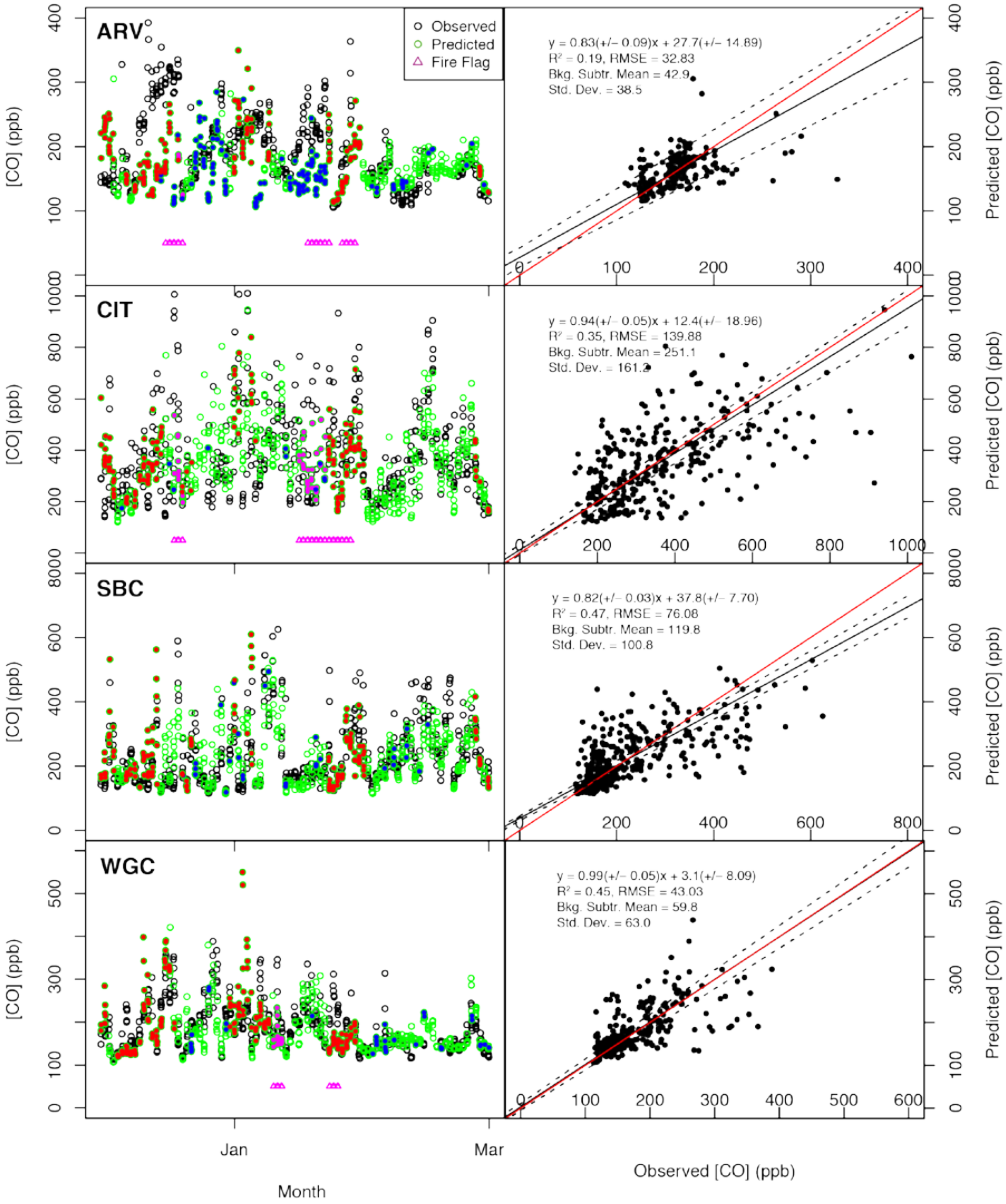

Figure 19. Same as Figure 16, but for December 2013 – February 2014. Note that blue filled circles in timeseries also include periods of southeasterly winds at ARV.

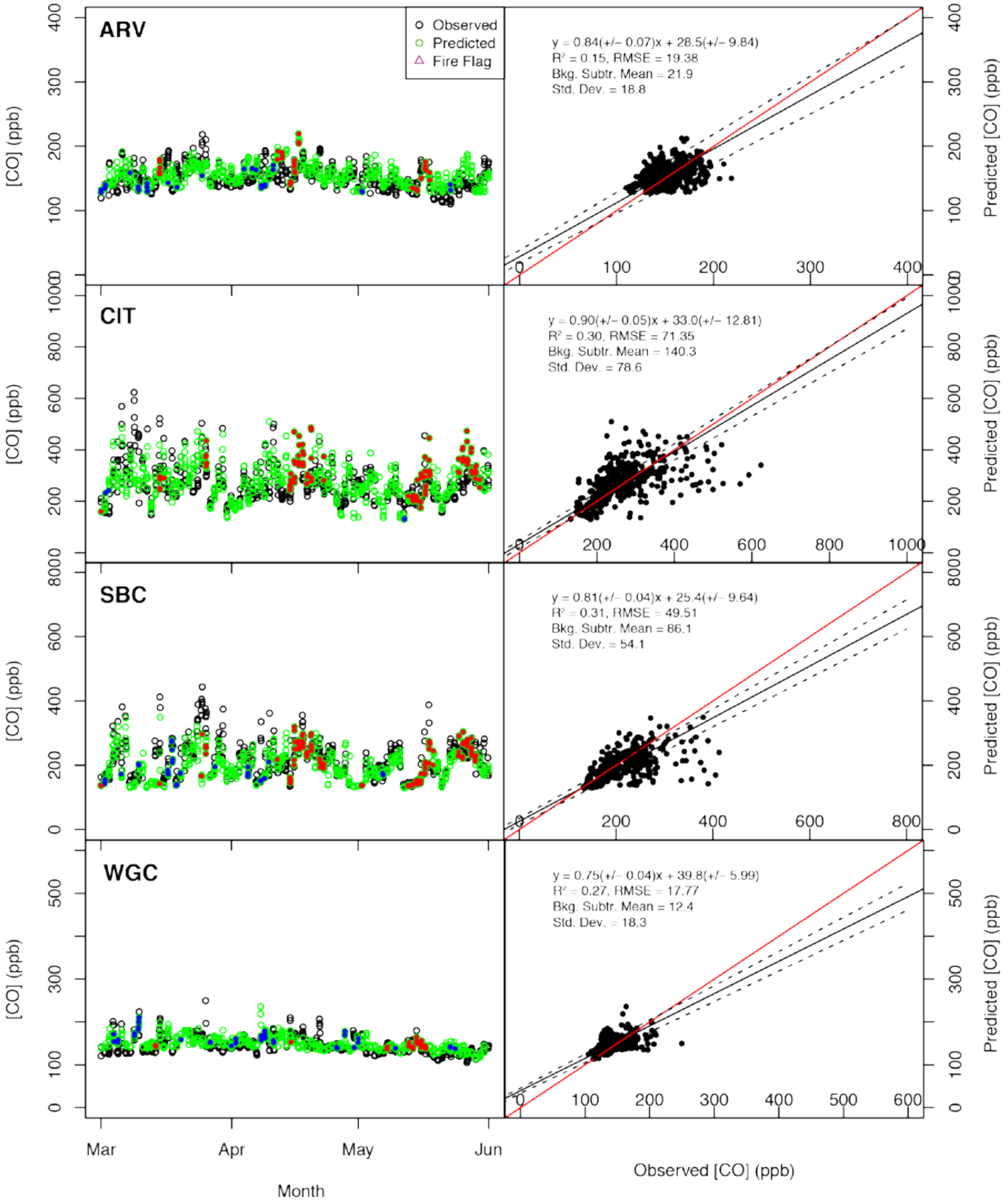

Figure 20. Same as Figure 17, but for March 2014 – May 2014.

3.1.3. Background and Random Meteorological Error Analysis

We estimated the potential impact of uncertainty in background estimates of CO using observations and WRF-STILT CO predictions at the STR tower site (Figure 6b). STR is a tall (sample stream intake at 232m) coastal site in San Francisco, and its observational footprint commonly samples relatively clean oceanic air, with minimal local influence on observed CO. As a result, STR was suitable for estimating potential uncertainty in background CO. We restricted the observational periods used for this analysis to those times when two requirements were met: (1) The surface wind measured at several coastal and off-shore buoy stations near STR had to be consistently westerly for eight hours preceding an observation, and (2) The difference between the total simulated CO and background CO at STR was required be less than 5 ppb (indicating minimal continental influence). Unlike ARV, CIT, SBC, and WGC where hourly CO data exists, CO observations were only taken once a day at STR for most days from June 2013 - May 2014 (October 2013 excluded). After filtering the data based on the above requirements, 35% of the available observations were retained (74 individual days), with the majority of the days retained being during non-winter months due to seasonal shifts in prevailing wind direction.

Comparing the filtered STR CO observational data with corresponding WRF-STILT simulated CO revealed a mean bias in simulated background CO of +4.5 ppb (± 1.4 ppb) with an RMSE (between predicted and measured CO) of 13.1 ppb. At sites during seasons with small observed mixing ratios of CO such as WGC during JJA, and both ARV and WGC during MAM the estimated RMSE of background CO was comparable to the total RMSE of simulated CO (20.8 ppb at WGC for JJA; 19.5 ppb at ARV for MAM; 17.7 ppb at WGC for JJA). Although the mean error in background CO was less than 5 ppb, the relatively large RMSE indicated that a large fraction of the random CO error at sites during seasons with small observed CO may be attributed to uncertainty in background CO mixing ratios.

Table 12 presents the RMSE of CO as a percentage of the mean CO mixing ratio associated with propagating random wind and boundary layer height errors using the error statistics given in Table 9. We found that the random errors associated with uncertainty in wind and boundary layer height ranged from 0 – 70 ppb depending on the site and season. These errors corresponded to 0 - 77% of the observed RMSE with mean biases removed (Table 12). The largest errors associated with meteorological uncertainties were during the winter months. Additionally, the largest fraction of error associated with meteorological errors was almost always at CIT. (30 - 50% of RMSE). Considering CIT's urban location this was reasonable. Since the influence of imposed random z_i and wind errors reduces with distance from the towers sites with footprints that are influenced by remote regions will be less influenced by local uncertainty in meteorology. It is also interesting to note the large influence of meteorological errors on ARV during DJF (77% of total RMSE). This strong sensitivity during DJF may provide some insight into the difficulties of simulating CO at this site during winter months. Finally, the influence of meteorological uncertainty at WGC is minimal during summer and fall. This was likely due to strong zonal winds during these seasons causing the SFBA region to be the primary influence on CO at WGC. Since the SFBA region is sufficiently distant from WGC and the CO mixing ratio has small variability, the application of local random errors on the effective footprint of WGC yields small uncertainty.

Table 12. Uncertainty due to Random Error of Boundary Layer Height and Boundary Layer Winds

Site \ Month	JJA	SON	DJF	MAM
ARV	NA	3.2 (12)	25.3 (77)	2.9 (15)
CIT	16.1 (30)	28.1 (41)	69.4 (50)	33.6 (47)
SBC	9.6 (21)	8.4 (13)	35.6 (47)	10.9 (24)
WGC	0.2 (1)	1.7 (8)	12.6 (29)	2.0 (13)

*The errors were added in quadrature, and uncertainty is presented as a percentage of seasonal RMSE of CO prediction (in parentheses)

When we combined the random meteorological uncertainty with uncertainty associated with estimated background CO (RMSE = 13.1 ppb) and estimated measurement uncertainty (3 ppb, Andrews et al. [2014]), these uncertainties accounted for between 43 - 87% of the total RMSE at ARV and WGC, but only 25 - 51% of the total RMSE at CIT and SBC (Table 13). The remaining uncertainty was likely due to a combination of sources. These sources can include undiagnosed systematic deficiencies in WRF-STILT transport that led to mean biases, limitations in our assumption that *a priori* CO emissions have minimal error for emission footprints, short-term variability of intermittent emission sources, and errors associated with sub-grid scale processes (aggregation error). There is also a possibility that the error statistics derived for each GHG site (Table 9) were not sufficiently representative of meteorological uncertainty. This could be due to error statistics for each GHG site (Table 9) being calculated from atmospheric profiler or radiosonde measurements that may be a significant distance from the GHG site (see Figure 6b), and may be derived from prior years for cases where observations were not available for 2013 - 2014.

Table 13. Uncertainty in Boundary Layer Height and Winds Combined with Measurement Uncertainty (assumed ~ 3 ppb) and Background Uncertainty (~13.1 ppb)

Site \ Month	JJA	SON	DJF	MAM
ARV	NA	0.51	0.87	0.71
CIT	0.39	0.45	0.51	0.51
SBC	0.35	0.25	0.50	0.38
WGC	0.71	0.65	0.43	0.87

*The combined uncertainty is presented as fraction of seasonal RMSE for CO prediction

3.1.4. Discussion

In this study we have assessed the magnitude of meteorological errors in WRF by region and season using a comprehensive set of surface and boundary layer observations, investigated the influence of varying land and boundary layer parameterizations on WRF-STILT estimates of predicted CO, estimated CO biases and random errors at four sampling sites in California (STR data were used only for background value evaluations, not for comparison with WRF-STILT predictions), and constrained the influence of errors in background CO and transport by propagating random errors in WRF-STILT. This was motivated by the assumption that error in *a priori* estimates of CO emissions were small relative to other GHGs such as CO_2, CH_4, and N_2O, and could hence be used to constrain the influence of background and transport model errors on predicted emissions that encompass key regions of California. In this section we discuss the implications of this work for atmospheric inverse modeling of other GHGs in California, and the limitations of our results.

First, our analysis of boundary layer meteorology for GHG sites across California showed that the mean errors (i.e., mean bias) associated with wind speed, wind direction, and boundary layer height were small relative to the random error component. Additionally, the mean errors associated with boundary layer wind speed and heights ($< \sim 0.5$ m s^{-1} and < 200 m, respectively) were generally less than the assumed observational accuracy of our instruments. There was some seasonality and spatial variability in the results that should be taken into account in studies of other GHGs. In particular, random errors in boundary layer meteorology tended to be minimized during summer months and largest during the winter when intermittent synoptic events were dominant.

Next, we found that the optimal parameterizations for key WRF-STILT boundary layer and land surface representations were not constant, and changed by season and site across California. In particular, changes in these parameterizations were necessary to capture influences of complex topography at southern California sites, and address the impact of irrigation on boundary layer heights in irrigated agricultural regions like the Central Valley.

Using the WRF-STILT parameterizations that best represented local meteorology, we found the mean bias of predicted CO relative to observations to be within 15 ppb for most sites and seasons across California, and simulated CO vs. observed CO regression slopes to be near unity (1.0 ± 0.20). This indicated that WRF-STILT was both generating predicted CO mixing ratios that had small biases and captured the dynamics necessary to simulate CO that can change on diurnal, synoptic, and seasonal timescales. This gives confidence in the capability for WRF-STILT to simulate the dynamics of other GHG's for most seasons and sites across California with minimal mean biases. However, there are periods when important uncertainties remain, and need to be treated with care. In particular, the winter months seem to present problems at ARV and SBC that require additional analysis to determine if deficiencies at these sites were due to limitations in *a priori* emission estimates or if improved model physics are needed to accurately capture the observed GHG dynamics in the absence of extensive data filtering. As described in Section 3.1.2, in this study those problematic periods were excluded from further analysis. Additionally, the development of more sites with sufficiently precise CO measurements would be useful for constraining and evaluating errors in transport and a priori emission estimates.

We have constrained the potential influence of errors in background CO, measurement error, and uncertainty in meteorology. Overall, the measurement error was found to be minimal relative to the uncertainty of background CO and meteorology, and combined these sources of uncertainty were between 35 - 85% of the RMSE between predicted and measured CO. Background uncertainty was dominant at sites with small seasonal CO mixing ratios such as WGC during spring and summer, and ARV during spring and fall. Meteorological uncertainties were dominant at CIT, likely due to its urban location, and were largest during winter at all sites. ARV was shown to be particularly sensitive to meteorological uncertainty during winter, which provides some guidance for improving the season's poor CO prediction.

Finally, the results of this study can be used to constrain the errors associated with atmospheric inversions of GHG's in California. This study has shown that WRF-STILT typically predicts CO with small mean biases (~ < 15 ppb). Given that mean biases were small, the uncertainty of an atmospheric inversion at a site is roughly equivalent to the deviation from unity of the regression slope between observed and predicted GHG's. For example, at CIT the deviation of regression slopes ranged from 0.05 to 0.11 indicating small potential uncertainty in the atmospheric inversion of GHG's at this location of ~10%, which is less than the assumed ~15% error associated with the a priori bottom-up estimates of CO emissions. Combining the results from CIT and SBC for SoCAB and WGC and ARV for the Central Valley (Table 14), we estimate annual mean slope biases of -0.10 ± 0.08 and -0.13 ± 0.08 (at 95% confidence) for SoCAB and the Central Valley, respectively. Combined, these results indicate that on an annual basis the uncertainty associated with atmospheric inversions of CO across California are between 10% ± 10% (at 95% confidence), assuming no significant errors in the CO emissions maps. Given this information, we conclude that atmospheric inversions of GHGs (e.g., CO_2, CH_4, and N_2O) may share similar levels of uncertainty and can be usefully estimated with the WRF-STILT transport because the prior emission uncertainties for GHGs are likely larger. We also note that the prior CO emissions are unlikely to completely capture fine scale spatial and temporal variations in actual CO emissions across California (and particularly near the measurement sites) for the 2013 - 2014 period, so these results likely represent an upper limit on systematic errors in transport model simulations. We will henceforth report uncertainties in GHG emissions at the 95% confidence level with the above assumptions.

Table 14. Mean Regression Slope Bias and Associated Uncertainty (68% CL) for Combined SoCAB and Central California

Season \ Region	SoCAB	Central California
JJA	-0.12 ± 0.04	-0.04 ± 0.06
SON	0.02 ± 0.05	-0.21 ± 0.03
DJF	-0.15 ± 0.03	-0.05 ± 0.04
MAM	-0.15 ± 0.03	-0.23 ± 0.03
Annual	-0.10 ± 0.04	-0.13 ± 0.04

3.2. Fossil Fuel CO_2

We estimate $ffCO_2$ emissions using measurements at the WGC site during 2009 - 2012 and at the CIT and SBC sites during 2013 June – 2014 May. We apply a Bayesian inversion method (see Section 2.6) using different set-ups such as different temporal scales (e.g., annual, seasonal), with/without data filtering (i.e., state of particles reaching the domain boundary, hereafter ocean flag, see Section 2.5.4 for details) and different factors to calculate the **R** matrix (see Section 2.6.6). We focus on the seasonal inversion result that adopts the ocean flag and the factor of 0.5 for the **R** matrix. Other results are presented in the sensitivity analysis.

3.2.1. Inter-annual $ffCO_2$ Emissions in Central California

The local (above background) $ffCO_2$ mixing ratios at WGC used in the inversion are shown in Figure 21 (top) from March 2009 – November 2012. For WGC, measurements are available at 1400 PST. Both of the predicted and observed mixing ratios vary with seasons, showing the largest mixing ratios in winter, which is consistent with the variation of the boundary layer depth in California [Bianco et al., 2011]. For instance, the average measured mixing ratios are larger than 7 ppm in all winters, while the values in other seasons are about 2 - 4 ppm.

We conduct Bayesian inversions using the scaled Vulcan $ffCO_2$ emission map introduced in Section 2.6.3 for regional analysis, with 17 scaling factors (i.e., $\boldsymbol{\lambda} = 17 \times 1$ vector) being solved for the subregions of California (16 regions) and outside of California. Here, we focus on the emissions for Regions 3, 7 and 8 (see Figure 3) from seasonal inversions because these are the regions with sensitivity based on the WGC footprints [Jeong et al., 2012a; 2012b].

After the first inversion, outliers are identified and removed when the difference between measured and predicted mixing ratios are larger than a certain value which is a factor α (e.g., $\alpha = 2$) of the estimated error [Bergamaschi et al., 2005]. In this study, α is set to 2 to 3 by requiring that the chi-square statistics be close to 1 as in Jeong et al. [2012a; 2012b; 2013] (see Section 2.6.5). The number of outlier removals varies with season and the mean removal rate is ~10%, which is consistent with the results in other studies (e.g., removal rate = 13.4% in Jeong et al. [2012a]).

The summary for best-fit slopes and RMS errors for different seasons before and after the inversions is shown in Table 15. From the table, it can be seen that the inversion has improved the best-fit results (predicted vs. measured) and reduced the RMS error. For instance, for 2012, the slopes are improved from 1.28 ± 0.65 (RMS error = 3.49 ppm), 0.43 ± 0.46 (7.07 ppm), 2.79 ± 1.01 (4.51 ppm) and 1.51 ± 1.03 (2.41 ppm) to 1.01 ± 0.16 (1.42 ppm), 0.69 ± 0.61 (4.76ppm), 1.13 ± 0.58 (2.02 ppm) and 1.11 ± 0.55 (1.4 ppm), respectively, equivalent to 26-55% RMS error reduction.

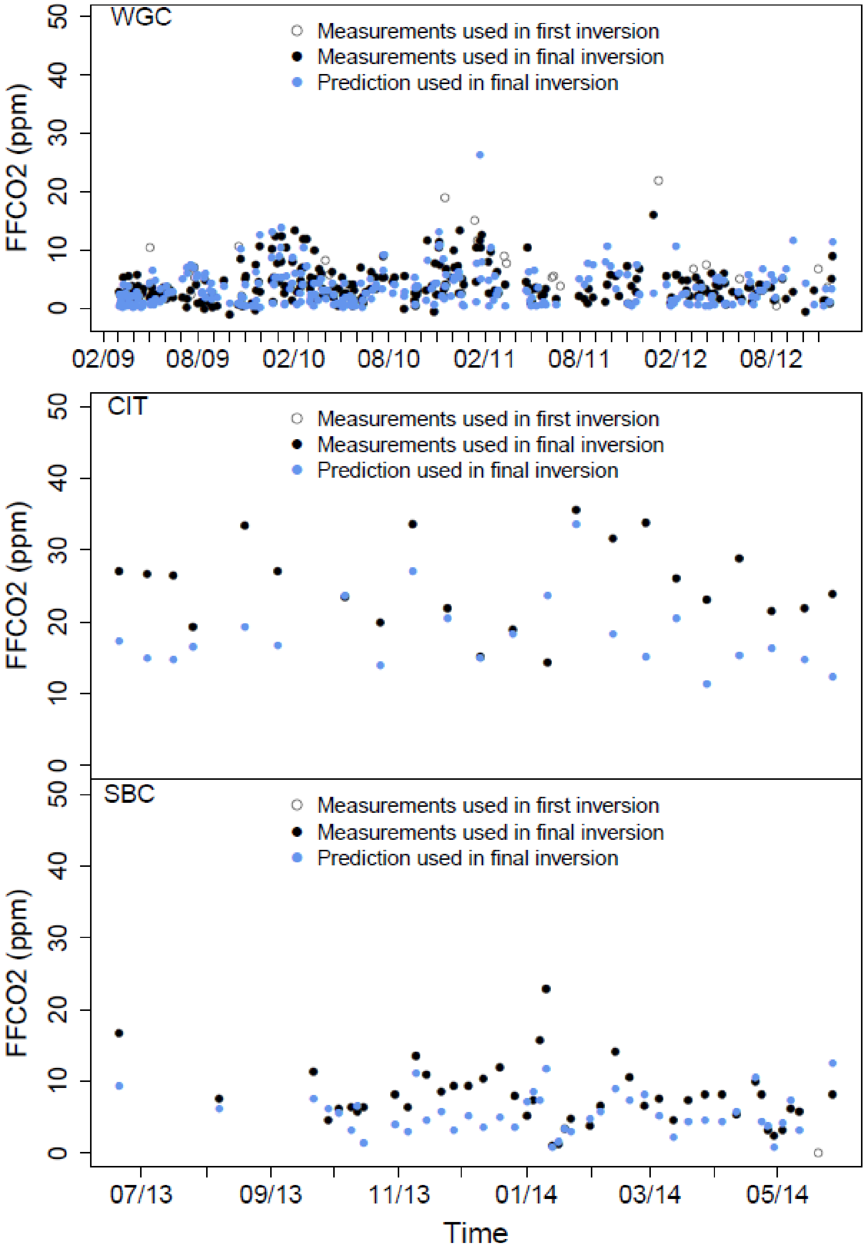

Figure 21. ffCO$_2$ local mixing ratios (after subtracting background) at WGC (top), CIT (middle) and SBC (bottom): measured ffCO$_2$ mixing ratios using the first inversion (gray open circle), measured ffCO$_2$ mixing ratios used in the final inversion (black filled circle), and WRF-STILT predicted ffCO$_2$ mixing ratios (light blue filled circle; used in final inversion).

Table 15. Best-fit Slopes from Regression of Predicted on Measured Mixing Ratios at WGC before and after Inversion during 2009 - 2012

Year		Winter	Spring	Summer	Fall
2009	Before inversion	NA	0.84±0.26 (2.17 ppm)	1.36±0.39 (3.33 ppm)	0.88±0.13 (2.42 ppm)
	After final inversion	NA	1±0.28 (1.69 ppm)	0.61±0.15 (1.43 ppm)	0.98±0.1 (1.76 ppm)
2010	Before inversion	1.02±0.23 (3.73 ppm)*	0.55±0.1 (2.51 ppm)	0.84±0.19 (2.03 ppm)	0.61±0.13 (3.7 ppm)
	After final inversion	0.98±0.22 (3.66 ppm)	0.8±0.11 (1.8 ppm)	0.96±0.21 (1.92 ppm)	0.82±0.1 (2.1 ppm)
2011	Before inversion	1.34±0.41 (5.46 ppm)	0.6±0.22 (3.17 ppm)	-1.53±0.92 (3.6 ppm)	1.46±1.03 (3.08 ppm)
	After final inversion	1.11±0.23 (3.89 ppm)	0.91±0.24 (2.17 ppm)	1.13±1.39 (1.06 ppm)	1.1±0.48 (2.29 ppm)
2012	Before inversion	0.43±0.46 (7.07 ppm)	2.79±1.01 (4.51 ppm)	1.51±1.03 (2.41 ppm)	1.28±0.65 (3.49 ppm)
	After final inversion	0.69±0.61 (4.76 ppm)	1.13±0.58 (2.02 ppm)	1.11±0.55 (1.4 ppm)	1.01±0.16 (1.42 ppm)

*The values in the parentheses are RMS errors.

The annual posterior emissions for 2009 - 2012 are shown in Figure 22, which is computed by averaging the emissions of four seasons in each year from the seasonal inversion. Here, since we don't have enough data in winter 2009 to use in the inversion, we assume that the emission in winter 2009 is similar to the average of other winters in 2010 - 2012. From the figure, it can be seen that the SF Bay Area (SFBA) is the dominant source of the ffCO_2 emissions in central California. For instance, the prior emission is 24, 64 and 11 Tg CO_2/yr for Region 3, Region 7, Region 8, respectively, and SFBA accounts for ~64% of the total emissions in central California. The corresponding posterior emissions are 24±10, 58±20, 11±6 Tg CO_2/yr (at 95% confidence), with SFBA accounting for ~62%±34% of the total emissions in central California. SFBA is the main contributor to the inter-annual variations of emissions in central California. Also, the northern Central Valley contributes to the inter-annual variation although it is relatively weak compared to that of SFBA. From the figure, it also can be seen that the total emissions in 2010 are slightly higher than those of 2009 and 2012. The total emissions from central California are 91±24, 108±22, 91±24, and 82±24 Tg CO_2/yr for 2009 – 2012, respectively. The average emission during the period of 2009 - 2012 is 93±22 Tg CO_2/yr (posterior / prior = 0.94±0.22). In terms of uncertainty reduction, the posterior emission uncertainty is mostly reduced in SFBA, while the reduction in the southern Sacramento Valley (Region 3) and the northern San Joaquin Valley (Region 8) is relatively small. This is due to the prevailing wind direction controlling the footprint of the air masses reaching the site, which indicates that WGC is a good receptor site for the dominant ffCO_2 source region of emissions in central California.

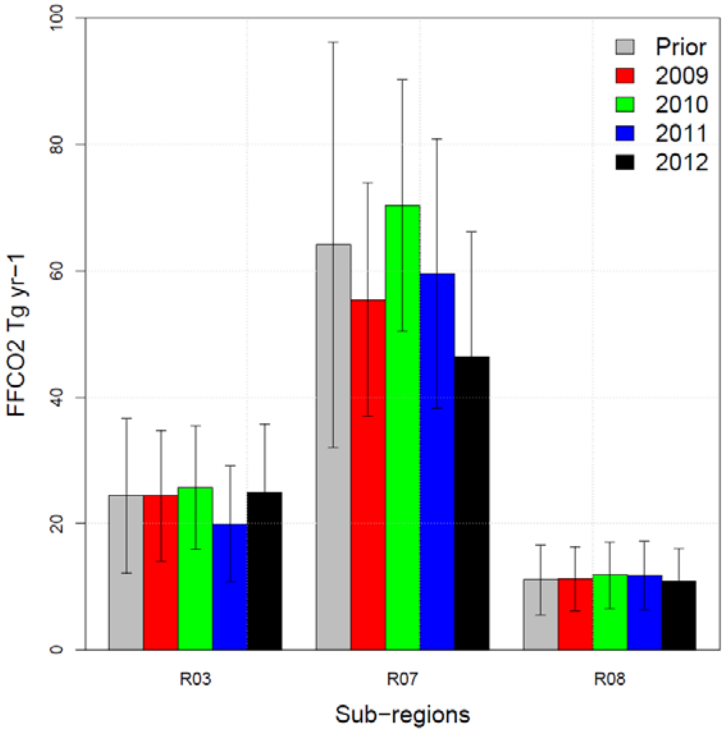

Figure 22. Posterior ffCO$_2$ emissions (posterior uncertainty at 95 confidence) based on 15 seasonal inversions in central California using measurements from WGC tower (factor for R matrix = 0.5; ocean cut used). Regions 3, 7 and 8 represent the Sacramento Valley (north Central Valley), SFBA, and the northern San Joaquin Valley (central Central Valley).

The emissions are summarized by season and are compared in Figure 23. For this inversion, all data for the same season from multi-year measurements were used to estimate each season's emissions. The emissions in central California are 109±16, 68±12, 82±14 and 108±22 Tg CO$_2$/yr at 95% confidence for spring, summer, fall and winter, respectively. In SFBA where emissions are constrained better than the other regions, the seasonal emissions are high in winter and low in summer. This is likely due to more energy use for heating required in the region.

We examine the sensitivity analysis of different assumptions on the model-data mismatch uncertainty for which we use three different factors (0.3, 0.5, and 0.7) to apply to the background-subtracted mean measurement. Also we analyze the sensitivity of inversion to different data filtering (with/without ocean flag) and temporal resolution (i.e., seasonal vs. annual). The posterior emissions based on different inversion set-ups are summarized in Table 16. As shown in the table, the ratios between posterior and prior emissions range from 0.78±0.08 to 0.94±0.22 at 95% confidence. These results show that the difference is larger when the ocean flag is not applied (i.e., not rejecting results where the majority of the STILT particles are not reaching the domain boundary). If the ocean flag is applied, the ratios between posterior and prior emissions range from 0.84±0.14 and 0.94±0.22, showing a better agreement between the prior and posterior estimates. This suggests that the posterior emissions are only weakly sensitive to the choice of the inversion set-ups given the statistical uncertainties.

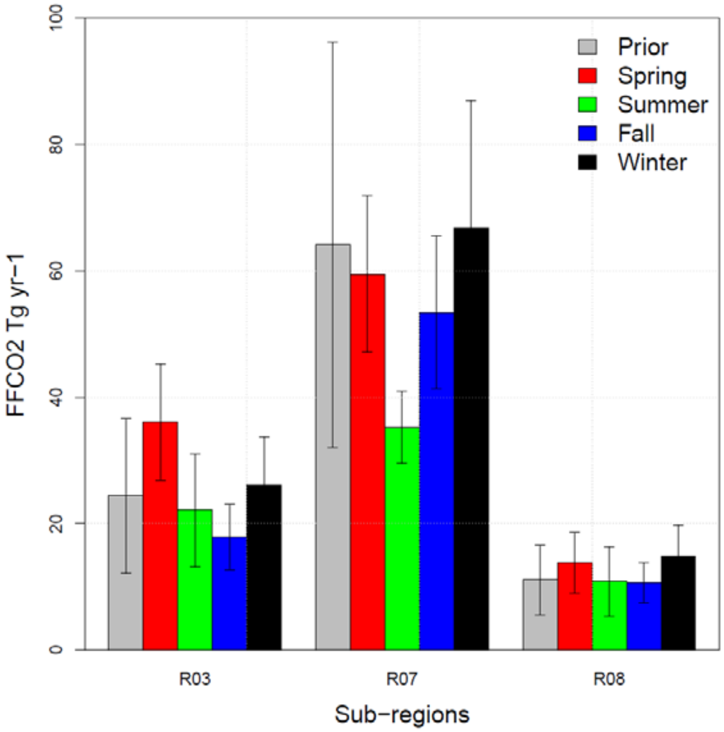

Figure 23. Posterior ffCO$_2$ emissions (posterior uncertainty at 95% confidence) based on four seasonal inversions (combining all data for each season) for central California using measurements from the WGC tower (factor for the R matrix = 0.5; ocean cut used). Regions 3, 7 and 8 represent the Sacramento Valley (north Central Valley), SFBA, and the northern San Joaquin Valley (central Central Valley).

Table 16. Ratios between Posterior and Prior Emissions Based on Different Inversion Set-ups in Central California Using Measurements from WGC

Temporal Scale	Data Filtering	Factor for R Matrix	Ratios between Posterior and Prior Emissions*
Seasonal (15 seasons)	No cut	0.3	0.91±0.16
Seasonal (15 seasons)	No cut	0.5	0.9±0.2
Seasonal (15 seasons)	No cut	0.7	0.9±0.24
Seasonal (15 seasons)	Ocean flag cut	0.3	0.94±0.18
Seasonal (15 seasons)	Ocean flag cut	0.5	0.94±0.22
Seasonal (15 seasons)	Ocean flag cut	0.7	0.92±0.26
Seasonal (4 seasons)	No cut	0.3	0.86±0.12
Seasonal (4 seasons)	No cut	0.5	0.88±0.14
Seasonal (4 seasons)	No cut	0.7	0.88±0.16
Seasonal (4 seasons)	Ocean flag cut	0.3	0.9±0.12
Seasonal (4 seasons)	Ocean flag cut	0.5	0.92±0.16
Seasonal (4 seasons)	Ocean flag cut	0.7	0.9±0.18
Annual	No cut	0.3	0.78±0.08
Annual	No cut	0.5	0.78±0.10
Annual	No cut	0.7	0.78±0.14
Annual	Ocean flag cut	0.3	0.84±0.10
Annual	Ocean flag cut	0.5	0.84±0.14
Annual	Ocean flag cut	0.7	0.84±0.16

* Uncertainties are reported at the 95% confidence level.

3.2.2. Regional $ffCO_2$ Emissions in Southern California

In southern California, we make use of the measurements at both CIT and SBC during the period of June 2013 - May 2014 (see Figure 3 for the site locations). For inverse modeling in these SoCAB sites, averaged measured and predicted mixing ratios over a short period (a few days) are used. As shown in Figure 21, the measured and predicted mixing ratios at CIT are much larger than those of SBC in all seasons. The seasonality of $ffCO_2$ is clearer at SBC than at CIT, showing a similar trend to that of WGC where mixing ratios are higher in winter than the other seasons (see Table 4 for average mixing ratio by season).

As in central California, we conduct Bayesian inverse analysis using the scaled Vulcan $ffCO_2$ emission map introduced in Section 2.6.3, and 17 scaling factors (i.e., 16 regions in California and one region outside California) are solved with each element of the 17 scaling factors representing each region. In terms of incorporation of measurements, three different set-ups for inverse modeling are used: (1) CIT measurements only, (2) SBC measurements only, and (3) combined measurements from CIT and SBC. Here, we focus the on results from the 3rd setup combining CIT and SBC.

Before inversion, the linear regression yields the best-fit slopes (predicted vs. measured mixing ratios) of 0.56 ± 0.07 (RMS error = 5.89 ppm), 0.55 ± 0.07 (9.59 ppm), 0.98 ± 0.06 (3.90 ppm) and 0.79 ± 0.08 (6.65 ppm), for spring, summer, fall and winter, respectively. After inversion, the RMS errors are reduced by 8 – 35%, and best-fit slopes are closer to unity: 0.63 ± 0.06 (5.33 ppm), 0.69 ± 0.09 (6.08 ppm), 1.13 ± 0.07 (3.36 ppm) and 1.03 ± 0.11 (6.13 ppm). However, we note that the posterior predictions are still lower than the measurements for spring and summer.

The seasonal posterior emissions for the southern California region are presented in Figure 24, which shows that the measurements form CIT and SBC mainly constrain emissions for Region 11 and Region 12, as indicated by the posterior uncertainty relative to that of the prior (at 95% confidence). The total emissions for the six regions are 205±34, 242±48, 206±38 and 242±38 Tg CO_2/yr for spring, summer, fall, and winter, respectively. The seasonality of $ffCO_2$ emissions in southern California is dominated by Region 12 (SoCAB), showing marginally higher emissions in summer and winter than in spring and fall. The posterior annual emission in southern California is 224±40 Tg CO_2/yr, which is 1.1±0.2 times the prior emission and ~2 times larger than that of central California. Among the sub-regions in southern California, the posterior emission for SoCAB is 132±38 Tg CO_2/yr, which accounts for 59±16% (54% in the prior) of the total emission in the southern California region. When measurements from only CIT or SBC are used in the inversion, we find that the results are similar to those of the combined measurements, yielding posterior annual total emissions of 217±48 and 217±44 Tg CO_2 /yr using either CIT or SBC, respectively.

As in the analysis for central California, we perform sensitivity analyses based on the uncertainty used in the **R** matrix, different temporal scales and data filtering (i.e., meeting background criteria). The sensitivity results are summarized in Table 17. The scaling factors (ratio of posterior to prior) range from 1.04±0.2 to 1.17±0.12 at 95% confidence, depending on the inversion set-up. In most cases, the scaling factors are close to unity, suggesting the posterior emissions are only weakly sensitive to the inversion set-up. In comparison with the result in central California, posterior emissions in southern California are more consistent with the prior, although ffCO$_2$ emissions are likely underestimated in the prior by ~10% in southern California.

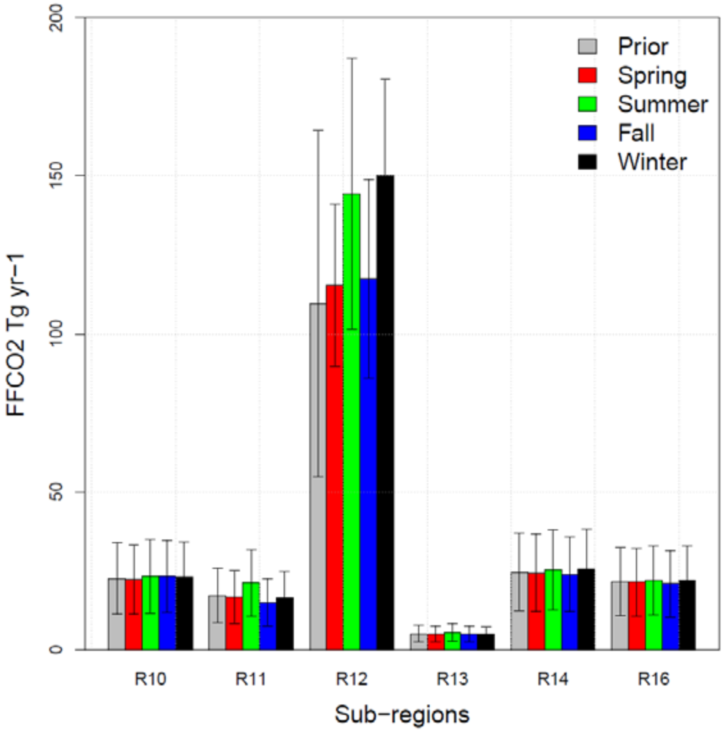

Figure 24. Posterior ffCO$_2$ emissions (posterior uncertainty at 95% confidence) in regions of southern California using combined measurements from CIT and SBC (factor for the R matrix = 0.5; ocean flag used). Regions 10, 11, 12, 13, 14 and 16 represent the Mojave Desert, South Central Coast, SoCAB, Salton Sea, San Diego County, and southern San Joaquin Valley air basins, respectively.

Table 17. Ratios between Posterior and Prior Emissions using Different Inversion Set-ups and Combined Measurements from CIT and SBC

Temporal Scale	Data Filtering	Factor for R matrix	Ratios between Posterior and Prior Emissions*
Seasonal	No cut	0.3	1.07±0.14
Seasonal	No cut	0.5	1.08±0.18
Seasonal	No cut	0.7	1.04±0.2
Seasonal	Ocean flag cut	0.3	1.14±0.16
Seasonal	Ocean flag cut	0.5	1.11±0.2
Seasonal	Ocean flag cut	0.7	1.07±0.22
Annual	No cut	0.3	1.1±0.12
Annual	No cut	0.5	1.1±0.14
Annual	No cut	0.7	1.05±0.14
Annual	Ocean flag cut	0.3	1.17±0.12
Annual	Ocean flag cut	0.5	1.14±0.14
Annual	Ocean flag cut	0.7	1.1±0.16

*at 95% confidence

3.2.3. Discussion

We further discuss the sensitivity of the inversion result to the assumption on the prior uncertainty. We conducted inversions using three different prior uncertainties of 25%, 50% and 75%, which assign the squares of 0.25, 0.5 and 0.75 (as the prior for each λ is 1) to the diagonal elements of the prior covariance matrix **Q**, respectively. The sensitivity analysis result is summarized in Table 18 for central and southern California regions. The result shows that WGC is only slightly sensitive to the assumed prior uncertainty, with the posterior emissions being statistically indistinguishable (at 95% confidence) among the three different assumptions. This is because the mean changes only by 2% (93 – 95 Tg CO_2) while the posterior uncertainty is proportional to the prior uncertainty. The increase of the posterior uncertainty with an increase in the prior uncertainty is typical in this type of inversion [Jeong et al., 2012a; Wecht et al, 2014]. The CIT and SBC result shows some sensitivity (increase in the posterior/prior ratio from 1.11±0.2 to 1.19± 0.38) although the larger uncertainty accounts for part of the increase, yielding statistically indistinguishable posterior emissions among the different assumptions.

Table 18. Sensitivity Analysis Result on Prior Uncertainty

Measurement Sites	Prior Uncertainty	Total Posterior Emission* ($Tg\ CO_2/yr$)	Posterior/Prior Ratio
WGC	25%	93±22	0.94±0.22
WGC	50%	93±30	0.93±0.30
WGC	75%	95±36	0.95±0.36
CIT and SBC	25%	224±40	1.11±0.2
CIT and SBC	50%	235±60	1.17±0.3
CIT and SBC	75%	240±78	1.19±0.38

*For WGC the estimate is the total emission for Regions 3, 7 and 8 during 2009 - 2012. For CIT and SBC, the estimate is the total for Regions 10, 11, 12, 13, 14 and 16 during 2013 - 2014. The posterior uncertainty is at 95% confidence.

We find the comparison of tower measurements and WRF-STILT-Vulcan model predictions obtains approximately consistent mixing ratios for both central and southern California. From the inter-annual analysis of WGC data, mean emissions for the central California region during 2009 - 2012 are 93±22 Tg CO_2/yr while the posterior/prior emission ratio is 0.94±0.22, suggesting emissions from central California are consistent with the *a prior* emission model to within ~ 6%±22%. We also observe potential differences with lower emissions in 2009 and 2012 and relatively larger emissions in 2010 and 2011, although these differences are not large compared to the combination of statistical and potential transport model uncertainties. In terms of spatial distribution, both the *a prior*i model and posterior results show that the urban region of the San Francisco Bay region dominates $ffCO_2$ emissions in central California. Temporally, there is an overall seasonal variation in the emissions from central California with larger emissions in winter and spring, and smaller in summer and fall, similar to the seasonality of natural gas usage reported for California (http://www.eia.gov/dnav/ng/hist/n3060ca2m.htm).

We also performed a sensitivity analysis to a combination of the model-measurement mismatch error prescribed in the **R** matrix and inclusion/exclusion of data that depends on meeting the background criteria (i.e., ocean flag cut). When the ocean cut flag is applied (accepting only data points for which the majority of STILT particles reach the domain boundary), the ratio between the posterior and prior emission (i.e., scaling factor) is in the range of 0.84±0.14 to 0.94±0.22 for different treatments of the **R** matrix. These results from different inversion set-ups provide increased confidence in the present estimation of $ffCO_2$ emissions from central California.

Similarly, the inversion analysis using the combined measurements from SBC and CIT for June 2013 to May 2014 shows that the posterior emission is 224±40 Tg CO_2/yr in the six regions of southern California (see Figure 24), with ratios of posterior to *a prior*i emission of 1.11±0.2. The CIT and SBC sites mainly constrain the emission in the Region 12 (SoCAB). Depending on the inversion se-up, the sensitivity analysis for southern California shows the scaling factor (posterior/prior) is in the range of 1.04±0.2 and 1.17±0.12, which further supports the emissions estimates. In addition, we find the ratio of estimated posterior to prior emissions is consistent for inversions using only data from CIT (1.08±0.24) or SBC (1.08±0.22) alone.

3.3. Methane

3.3.1. State Total Emissions

State total emissions were estimated by optimizing 195 scaling factors each month (i.e., dimension of $\boldsymbol{\lambda} = 195 \times 1$) given the multi-site measurements and multiplying them by the CALGEM prior emissions, which were essentially the same as the CARB inventory at the sub-region scale (see Figure 3 for each sub-region). As described, we estimate a scaling factor for each 0.3° pixel within the major emission regions (i.e., SV, SF, SJV and SC), which account for 84% of the CALGEM total emission. For other regions, we estimated a scaling factor for each region. Figure 25 compares predicted and background-subtracted measured mixing ratios using all data (used in the inversion) available for each season and also shows linear regression analysis results. Before inversion, the regression analysis estimates best-fit slopes to be 0.41 – 0.75 (predicted vs. measured). This simple analysis without full consideration of errors suggests that CH_4 emissions are underestimated by the CARB inventory. After inversion, the best-fit slope, root-mean-square error (RMSE) and coefficient of determination (R^2) for each season are significantly improved.

The HBI analysis estimates the state total annual emission is 2.04 - 2.90 Tg CH_4/yr at 95% confidence (median = 2.42) not including the (median) posterior estimate for natural wetlands (0.066 Tg CH_4/yr). This estimate is equivalent to 1.2 - 1.8 times the anthropogenic CH_4 emissions in CARB's current official inventory for the year 2013 (1.64 Tg CH_4/yr). Note that the state total in CARB's current official inventory for 2013 is only slightly different from the prior total in Table 6 after excluding the wetland emission. We report an interval of uncertainties in percentile because HBI produces a probability distribution from posterior samples (not standard errors) unlike that of the Bayesian inversion used in Jeong et al. [2013] and Wecht et al. [2014] and other studies. The state total emission estimate from HBI is consistent with the annual emission estimate from Jeong et al. [2013], 2.38±0.67 Tg CH_4/yr (at 95% confidence), which combined inverse model estimates for the Central Valley with urban emissions estimated by Wennberg et al. [2012].

As noted in the methods section (Section 2), transport model error could affect the estimate of CH_4 emissions. Comparison of predicted and measured CO mixing ratios at the four towers during June 2013 – May 2014 (Section 3.1) yields near-unity slopes for the majority of sites and seasons, suggesting that the WRF-STILT simulations are sufficient to estimate emissions of CO and likely other GHGs across California to within 10% ± 10% at 95% confidence level on annual timescales. Based on this mean result, we add a mean transport bias uncertainty of 10% in quadrature to our Bayesian statistical uncertainty estimates to estimate total uncertainty in annual state-total GHG emissions. After adding the transport bias uncertainty, we estimate state annual anthropogenic CH_4 emissions to be 2.42 ± 0.49 Tg CH_4/yr (95% CL including transport bias uncertainty), higher (1.2 - 1.8 times) than the anthropogenic emission in CARB's current inventory (1.64 Tg CH_4/yr in 2013). We note that in Section 3.1 the CO analysis showed a 10% low bias in the prediction (annual average) compared to the measurement. This suggests that the CH_4 prediction from WRF-STILT (the same transport used for both CO and CH_4) might also be lower by 10% assuming the CO result is applicable to that of CH_4. Then this low bias in the prediction (before inversion) leads to overestimation in the posterior estimate after inversion (to match the measurement). If we correct for the 10% median CH_4 emissions (0.24 Tg CH_4) assuming the bias in CO is applicable to CH_4, the estimated CH_4 emissions drop to 1.0 - 1.6 times the CARB inventory. Undiagnosed sources of uncertainty may increase these error bounds beyond that indicated here. We also note that the transport error analysis based on CO rests on an unproven assumption that *a priori* annual state total CO emissions are known to better than 10%, though Brioude et al. [2013] found that a comparison of measured and predicted CO (using the WRF-FLEXPART model) agreed to within about 15% for aircraft flights over SoCAB conducted in May and June, 2010.

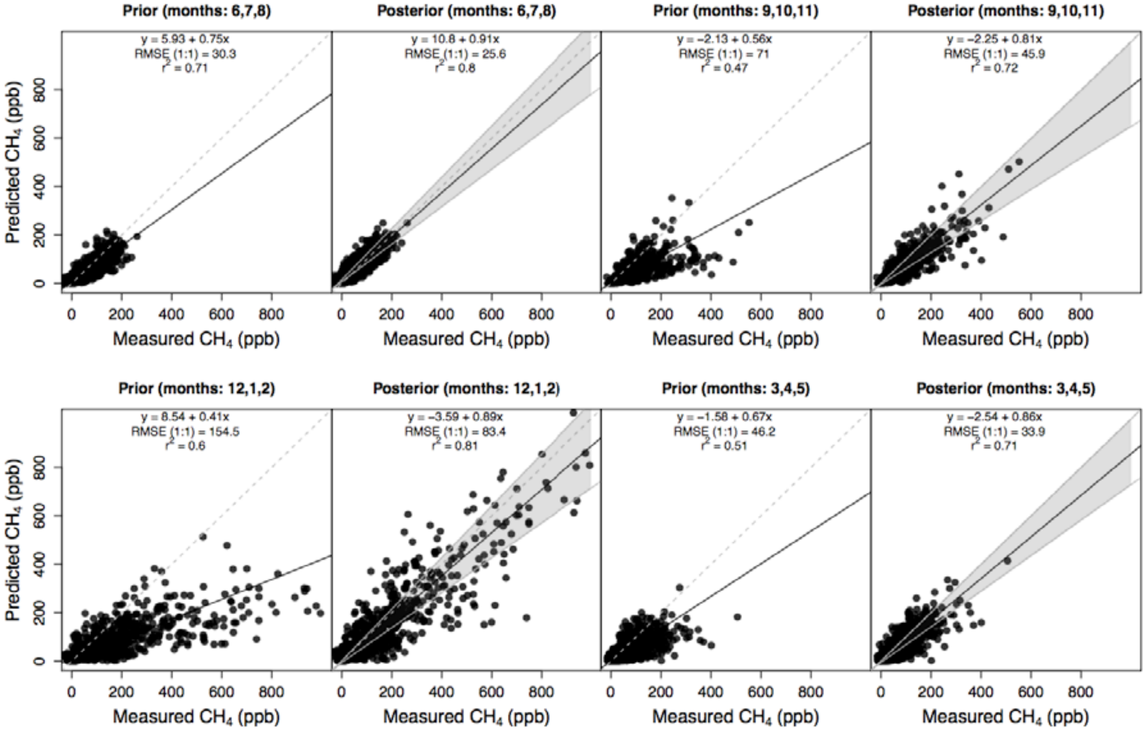

Figure 25. Comparison of predicted and measured CH_4 mixing ratios before (prior) and after (posterior) inversion for each season. The relatively low best-fit slopes in the prior comparison (left plot in each season) suggest prior emissions are underestimated. Filled circles represent individual 3-hour data points across different sites used in the inversion. The gray dashed line indicates the 1:1 line and the black solid line represents the best fit for the data shown. The regression coefficients in the posterior plot were calculated based on the median values of the 25000 MCMC samples. The gray shaded area in the posterior plot represents the 95% uncertainty region for the regression analysis using 25000 MCMC samples.

We estimate statewide CH_4 emissions for each season because our measurements are available for a full annual analysis (June 2013 – May 2014). This is the first analysis to estimate full seasonal CH_4 emissions using multi-tower measurements across California. Although Jeong et al. [2013] estimated seasonal CH_4 emissions in California using multi-tower measurements, they analyzed ten-month data only (not including July and August data) and did not constrain emissions from the southern California region. Figure 26 shows the estimated mean seasonal emissions for the state, which are the average of the monthly emissions belonging to the season. Note that the prior emissions in Figure 26 only partially account for seasonality because CALGEM has monthly emissions for crop agriculture (largely rice) and wetlands but not other sources. Across seasons, the posterior emissions are greater than the prior emissions. without strong evidence for seasonality, similar to previous work by Jeong et al. [2013].

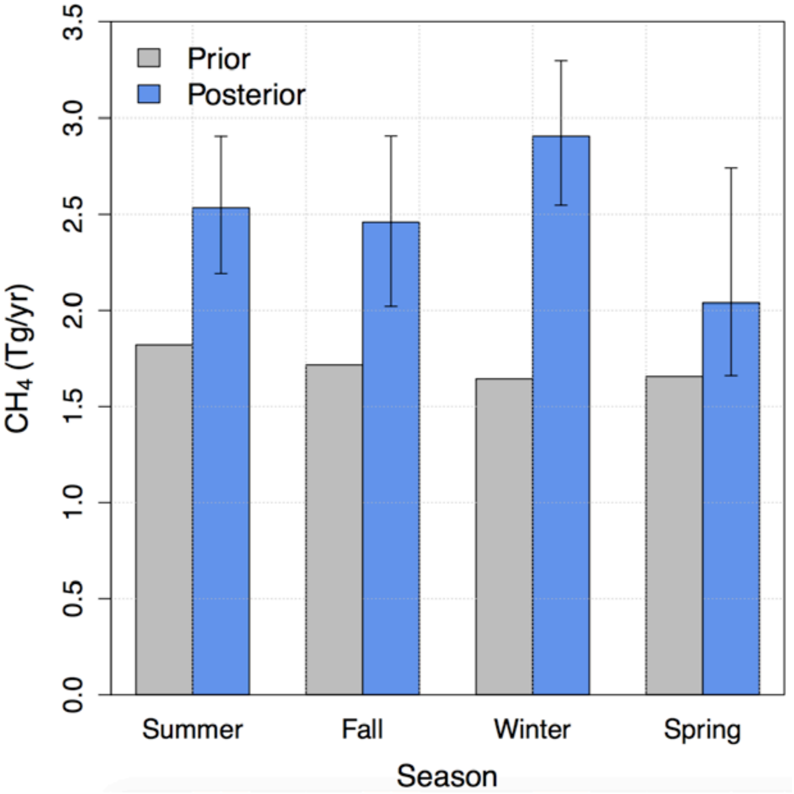

Figure 26. Inferred CH_4 emissions using measurements from 13 sites for four seasons: summer (JJA), fall (SON), winter (DJF) and spring (MAM). The error bar for HBI represents the 95% confidence interval around the median value of the posterior emission estimate.

3.3.2. Emissions in Rural and Urban Regions

The hierarchical Bayesian inversion using multiple sites across California constrains CH_4 emissions from a significant portion of both rural and urban regions in California. In particular, the inverse analysis in this study yields a large reduction in the posterior uncertainty for the urban regions of California (e.g., SoCAB) compared to the inverse analysis by Jeong et al. [2013] where urban regions were under-sampled. We first examine the emissions for the rural regions of California, focusing on the Central Valley because it accounts for about 90% of the total rural emissions based on the CALGEM prior emission.

Figure 27 shows the comparison between prior and posterior (after inversion) emissions for the major emission regions that account for 84% of the state total in the CALGEM prior emission, including the Central Valley of California (see Table 6). We estimate that the Central Valley (Regions 3 and 8) emissions are 1.02 – 1.74 Tg CH_4/yr (at 95% confidence, median = 1.38 Tg CH_4/yr). These estimates are consistent with the annual emission for the Central Valley estimated by Jeong et al. [2013], which is 1.57± 0.20 Tg CH_4/yr. These results suggest emissions from the Central Valley are underestimated in the CALGEM prior emissions (0.94 Tg CH_4/yr). The spatial distribution of posterior emissions is shown in Figure 28 along with comparison with the CALGEM prior field. As can be seen in the figure, the posterior emissions for some of the pixels in the Central Valley are significantly larger than the prior. However, it should be noted that the uncertainty range for those pixels is also significantly large. This result shows that although the emissions at the sub-regional scale are well constrained in the Central Valley (aggregated error at 95% confidence is ~25% of the posterior total of the Valley), the emission uncertainties for many of the individual pixels are still high.

For urban emissions of California, we focus on emissions from the two major urban regions (SoCAB and SFBA). According to the CALGEM prior, the two urban regions account for 25% of the state total emissions. The HBI analysis estimates the posterior emissions are 301 – 490 (median = 380, 95% confidence) Gg CH_4/yr for Region 12 (SoCAB), which are 0.9 – 1.4 times the prior (349 Gg/yr). This suggests that the prior inventory for SoCAB is consistent with our posterior estimate. Our posterior estimate is also consistent with the results of most of the recent studies that were conducted in SoCAB [Wunch et al., 2009; Hsu et al., 2010; Wennberg et al., 2012; Peischl et al., 2013; Wecht et al., 2014; Wong et al., 2015; Cui et al., 2015]. Figure 29 shows the comparison of estimated CH_4 emissions for SoCAB among eight different recent studies including this study. The estimate (600 Gg CH_4/yr) by Wunch et al. [2009] using the CH_4/CO_2 ratio is likely the upper limit for SoCAB CH_4 emissions and is not included in this comparison. Although the estimated emissions are consistent among the different studies given the reported uncertainty, there are some differences in the mean/median estimates. These differences may arise from different assumptions and undiagnosed uncertainties (e.g., spatial distribution of bottom-up emissions, transport model errors, different seasonal coverage). For example, most of the studies in SoCAB rely on the combination of measured CH_4 to CO_2 or CO ratios and the bottom-up inventory of CO_2 or CO, with uncertainties that assume those inventories are relatively well-known (e.g., 10% uncertainty assumption in CO_2 inventory by Wong et al. [2015]).

This study constrains CH_4 emissions for SFBA with a significant reduction in the posterior uncertainty, compared to Jeong et al. [2012; 2013]. We estimate the posterior emissions for SFBA to be 159 – 340 (median = 245) Gg CH_4/yr (at 95% confidence).

These emission estimates are consistent with those reported by Fairley and Fischer [2015] where they reported a total of 240±60 Gg/yr (at 95% confidence) for the recent period of 2009 to 2012 using CH_4:CO enhancement ratios from 14 air quality sites in SFBA. For SFBA, we have two bottom-up estimates to be compared with our inverse analysis: CALGEM emission model (143 Gg CH_4/yr, see Table 6) and the Bay Area Air Quality Management District (BAAQMD) inventory (124 Gg CH_4/yr, [BAAQMD, 2015]). Compared to bottom-up estimates, actual CH_4 emissions in the SFBA are likely 1.1 – 2.4 and 1.3 – 2.7 times larger than the CALGEM prior and BAAQMD's inventory, respectively. This suggests that both inventories are lower than our posterior estimate.

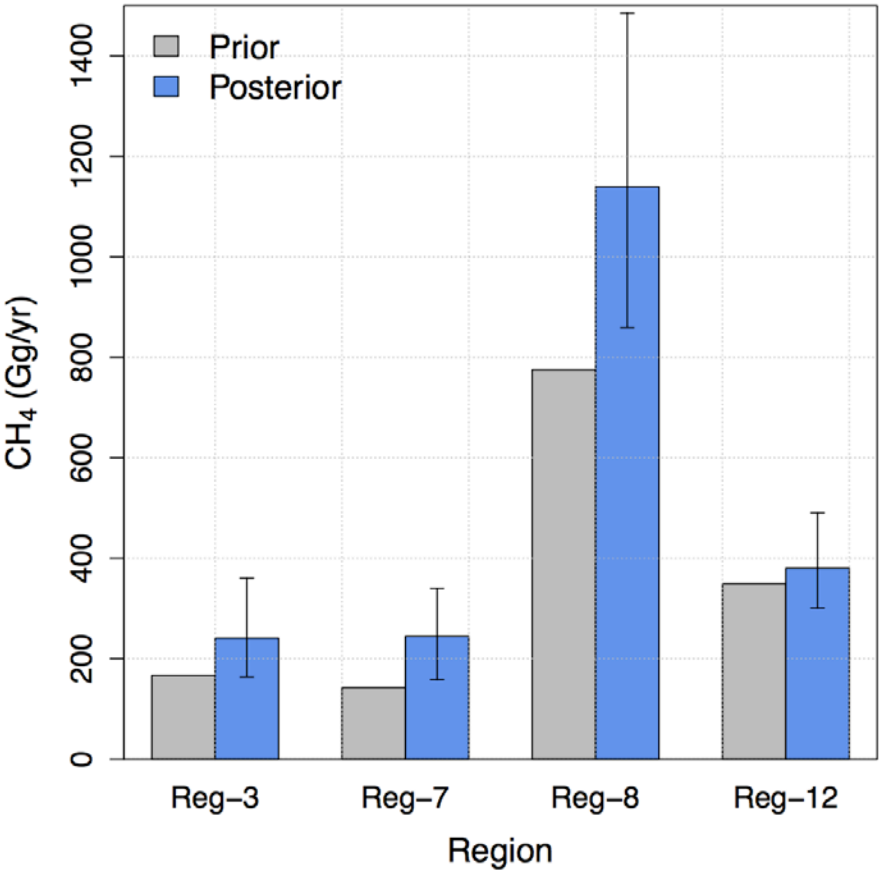

Figure 27. Estimated annual CH_4 emissions for the major emission regions (at 95% confidence). Regions 3, 7, 8 and 12 represents the Sacramento Valley (SV), San Francisco Bay Area (SF), San Joaquin Valley (SJV) and South Coast (SC) air basins, respectively.

Table 19. Posterior Annual Emission Estimates (Gg CH_4/year) by Region

Regions[a]	1 (NEP)	2 (NC)	3 (SV)	4 (MC)	5 (LC)	6 (GBV)	7 (SF)	8 (SJV)	9 (NCC)	10 (MD)	11 (SCC)	12 (SC)	13 (SS)	14 (SD)	15 (LT)
Prior	28	35	167	19	2	4	143	775	24	42	56	349	13	52	1
HBI Posterior (Upper)[b]	186	144	360	84	20	23	340	1486	180	243	162	490	68	145	2
HBI Posterior (Lower)[c]	1	1	164	1	0	0	159	859	1	1	1	301	1	37	0

[a] Region abbreviations are shown in the parentheses.

[b] 97.5th percentile

[c] 2.5th percentile

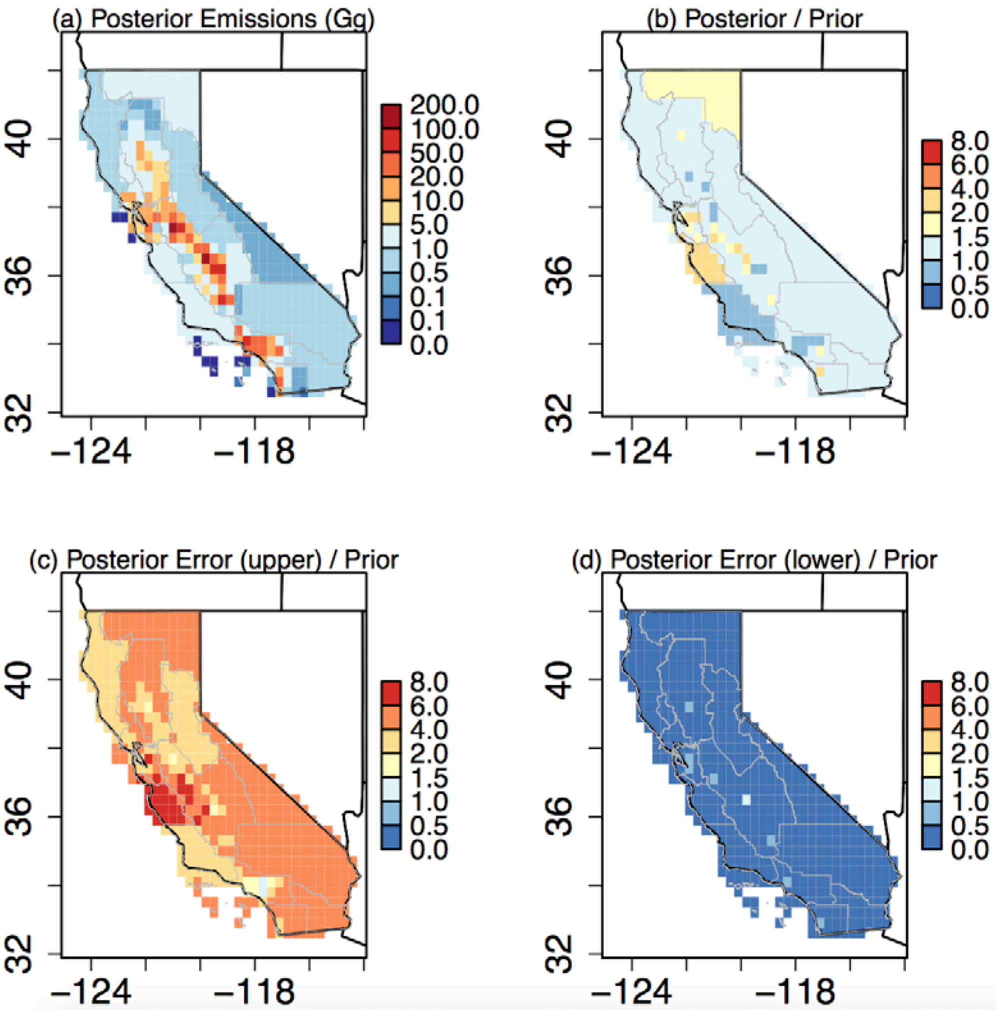

Figure 28. Estimated annual CH_4 emissions from the HBI analysis: (a) posterior (median) annual emissions (Gg/yr), (b) ratio of posterior to prior, (c) ratio of estimated 97.5th percentile to prior, and (d) ratio of estimated 2.5th percentile to prior.

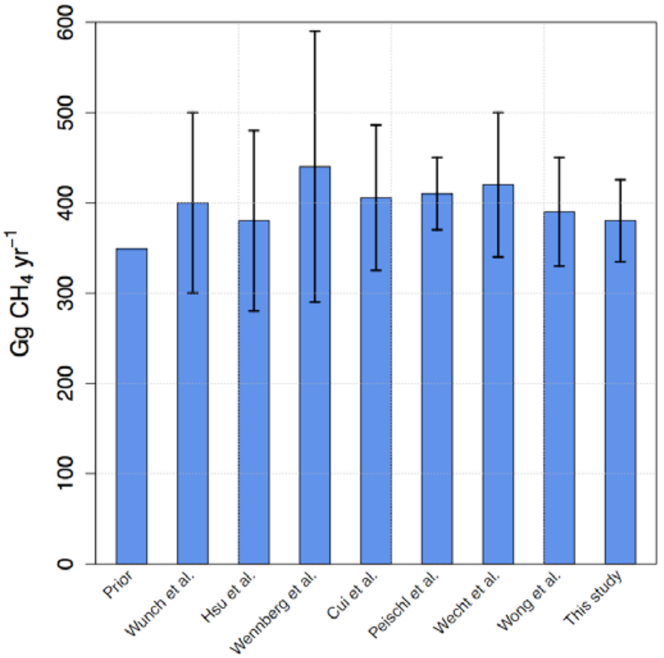

Figure 29. Comparison of the CALGEM prior (total for SoCAB = 349 Gg CH_4/yr) and estimated CH_4 emissions for SoCAB in the eight different recent studies including the posterior emission from this study. The value from Wunch et al. [2009] shows the CO-based estimate. Originally Hsu et al. reported LA County emissions (at 200 Gg CH_4/yr) and Wennberg et al. expanded the Hsu et al. results (shown here) to the full SoCAB. The uncertainty estimates are 68% confidence intervals reported by the individual studies.

3.3.3. Source Attribution of Emissions

We investigate the likely sources of emissions in the rural and urban regions of California using the results from this study and previous studies. We estimate CH_4 emissions from different sources assuming the spatial distribution of the CALGEM emission model. Based on this assumption, we scale individual prior emissions by source sector at each pixel or region by the inferred scaling factors from the HBI analysis. Figure 30 (left) shows posterior annual emissions for the HBI analysis by sector (the result is also provided in a table in Appendix H). The posterior emissions (804 – 1410 Gg CH_4, median = 1070 Gg) for the dairy livestock (DLS) are 1.1 - 1.9 times larger than the prior emissions. Assuming the distribution of the prior, the posterior estimates for the non-dairy livestock (199 – 345 Gg CH_4/yr, median = 263 Gg) are also 1.3 – 2.2 times larger than the prior. The combined total emissions for dairy and non-dairy livestock emissions (1050 - 1699 Gg CH_4/yr) are 1.2 – 1.9 times higher than the CALGEM prior. The underestimate in livestock emissions agrees with the results discussed in the region analysis that posterior emissions in the Central Valley (Regions 3 and 8) are larger than the CALGEM prior. This is also consistent with the reported livestock emissions (1265 – 1805 Gg CH_4/yr, at 95% confidence) by Jeong et al. [2013]. A recent global study suggests a similar underestimation for manure management in a bottom-up inventory. Based on published data on field-scale measurements of GHG emissions, Owen and

Silver [2015] report that predicted CH_4 emissions by the Intergovernmental Panel on Climate Change (IPCC) Tier 2 method are lower than the mean estimates using the field measurements for most manure management practices. However, we caveat the source attribution above because the spatial distribution of sources by sector may not be perfectly captured in the CALGEM model. In terms of seasonality by sector, Figure 30 (right) suggests that there is no significant seasonal variation in the posterior emissions except for the crop agriculture (CP, mostly rice) and wetland (WL) sectors.

Our inverse analysis also suggests that actual natural gas (NG; includes petroleum production) and landfill (LF) emissions are likely larger than the prior emissions. The NG result (i.e., higher posterior than prior) is perhaps because we used smaller NG prior emissions (after scaling to CARB's inventory) than those estimated by Jeong et al. [2014] where they find their spatially explicit bottom-up inventory for NG itself is generally lower than those of top-down analyses (e.g., Peischl et al. [2013], Wennberg et al. [2012]). The result for seasonal emissions by sector in Figure 30 (right) shows that the seasonal variation for NG and LF is small, consistent among seasons within error. Other sources, including petroleum refining and mobile (RM), wastewater (WW), crop (rice) emissions (CP), and wetlands (WL) are generally similar between prior and posterior emissions. The rice emissions are 39 – 101 Gg CH_4/yr, which are consistent with those of Jeong et al. [2013] (68±18 Gg, at 95% confidence) and Peischl et al. [2012] (~85 Gg). Except for WL and CP, the seasonal variation in the emissions for these other sources is small, showing similar posterior emissions within error (Figure 30).

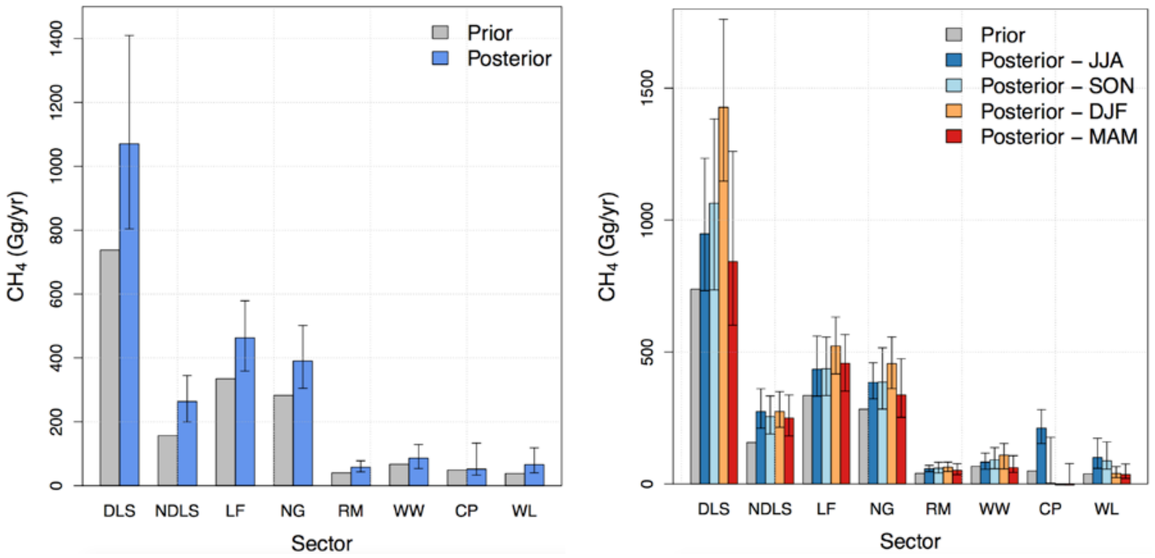

Figure 30. Posterior annual (left) and seasonal (right) emissions (Gg CH_4/yr) estimated from the HBI analysis by sector: dairy livestock (DLS), non-dairy livestock (NDLS), landfill (LF), natural gas including petroleum production (NG), petroleum refining and mobile sources (RM), wastewater (WW), crop agriculture (CP, largely rice), and wetland (WL). The error bar represents the 95% confidence interval.

3.3.4. Further Discussions

We further discuss likely source emissions by comparing our estimates with results from previous studies. Jeong et al. [2013] estimated annual CH_4 emissions from the livestock source sector in the San Joaquin Valley to be 1.13 ± 0.42 Tg CH_4/yr (at 95% confidence), significantly higher than all other sources combined in the region (Region 8). This is consistent with the finding by Gentner et al. [2014] who concluded that the "vast majority" of the total emission in San Joaquin Valley is due to dairy operations. In another similar study, Guha et al. [2015] used collocated measurements of CO and various volatile organic compounds (VOCs, e.g. alkanes) and a Positive Matrix Factorization (PMF) technique to estimate the contribution of regional sources to observed enhancements of CH_4 and N_2O. The results in Guha et al. [2015] indicate that the livestock emissions account for a majority of the CH_4 (70 - 90%, uncertainty = 29%) enhancements based on measurements near Bakersfield, California during May - June 2010. The reported 29% uncertainty is calculated from the standard deviation in the mass fraction of CH_4 attributed to the dairy source factor profile as estimated from a bootstrapping method. Although these two studies do not report estimated emissions by mass, they suggest a significant portion of the total CH_4 emission in the San Joaquin Valley (Region 8) is attributed to the livestock sector.

More quantitatively, Jeong et al. [2014] estimated CH_4 emissions from the natural gas sector (petroleum production included) for the state based on activity data and reported emission factors (mostly from US Environmental Protection Agency (EPA)). They estimated the emission from the natural gas sector to be 128 Gg CH_4/yr for the San Joaquin Valley, the majority of which was from petroleum and natural gas production. After adjusting this bottom-up estimate based on the result in SoCAB by Peischl et al. [2013], they estimated the natural gas emission in San Joaquin Valley to be 162.6 Gg CH_4/yr, with the San Joaquin Valley accounting for 30% of the state total natural gas emissions. The adjusted natural gas emission (i.e., 162.6 Gg) by Jeong et al. [2014] is 11 - 19% of the annual total emissions (0.86 – 1.49 Tg CH_4) in the San Joaquin Valley estimated in this study, which is consistent with Gentner et al. [2014], Guha et al. [2015] and Jeong et al. [2013]. Note that, based on the CALGEM prior, the San Joaquin Valley emits 82% of the total CH_4 emissions in the Central Valley, 86% of which is from the livestock sector. These results suggest that our a priori assumption about the ratio of livestock emissions to the total in the San Joaquin Valley is likely similar to the source attribution of the actual emissions in Region 8. Furthermore, our source analysis indicates that the posterior emissions for landfill, natural gas, and wastewater are generally consistent with or slightly higher than our CALGEM prior, and livestock emissions are higher than the prior although this is a statewide result (see Figure 30). Given this source analysis result, the higher posterior emissions in San Joaquin Valley (Region 8) from our region analysis (1.1 – 1.9 times the CALGEM prior) are likely mainly due to livestock sources. A recent study by Wecht et al. [2014] estimated state total emissions of 0.87, 0.64 and 1.05 Tg CH_4/yr for the livestock, natural gas-oil, and landfill-wastewater sectors, respectively, using the CalNex (May – June 2010) CH_4 observations. If we multiply these estimates by the ratio of San Joaquin Valley vs. California total emissions in our CALGEM prior, we obtain 0.64 (=0.87 × 0.74), 0.12 (0.64 × 0.18) and 0.09 (1.05 × 0.09) Tg CH_4/yr, for livestock, natural gas-oil and landfill-wastewater, respectively. This shows that the CH_4 emissions from the natural gas-oil and landfill-wastewater sector are 33% (=(0.12+0.09)/0.64) of the livestock emissions, which appears to be higher than found by Gentner et al. [2014], Jeong et al. [2013, 2014], and this study.

We also examine the emissions in SoCAB for possible source attributions by combining the results from this study and other published literature. In this study we estimated that the CH_4 emissions in SoCAB are 330 – 421 (median = 380, where we report the 68% confidence level for comparison with other work) Gg CH_4. Combining the recent studies in SoCAB including this study (for Wunch et al. the estimate based on CO/CH_4 ratios is used) we estimate the SoCAB CH_4 emission is 341 - 465 Gg CH_4/yr (at 95% confidence, mean/median = 403 Gg CH_4) [Wunch et al., 2009; Hsu et al., 2010; Wennberg et al. 2012; Peischl et al., 2013; Wong et al., 2015; Wecht et al., 2014; Cui et al., 2015]. To calculate the uncertainty in this estimate, we generated 50000 MCMC samples for each study based on the mean and uncertainty reported in individual studies (similar to generating samples for the prior distributions in HBI) and combined them for an overall mean distribution. Note that the uncertainty for the overall mean distribution is smaller than those of the individual studies because the mean estimates of individual studies are close to the combined mean (i.e., a small spread around 403 Gg CH_4), suggesting emission estimates in SoCAB are converging. It should also be noted that the emission estimates for SoCAB in most of these previous studies including ours include emissions from petroleum seepage and abandoned wells in the total without distinguishing these as non-anthropogenic emissions. This suggests that the CALGEM prior total for SoCAB (349 Gg CH_4) scaled by the CARB inventory is comparable to the recent top-down analyses for SoCAB.

For source attribution, Wennberg et al. [2012] suggest that the majority of the CH_4 enhancements observed are likely due to natural gas activities, while Peischl et al. [2013] estimates 192± 54 Gg CH_4 for the combination of emissions from natural gas transmission and distribution plus local seeps, and 32±7 Gg CH_4 for oil and gas production and processing. Hence the total of fossil fuel related activities from Peischl et al. [2013] is 224 ±55 Gg CH_4, assuming uncorrelated errors in the above estimates. This estimate is larger than our CALGEM prior for the natural gas sector (112 Gg, see Table 6) by a factor of 1.5 – 2.5, suggesting an underestimate for total fossil fuel related emissions in the CALGEM maps for SoCAB. For landfill, wastewater and livestock sectors, the CALGEM prior estimates 224 Gg CH_4/yr for SoCAB, which is consistent with that (182 ± 54 Gg CH_4/yr) of Peischl et al. [2013]. For livestock, Cui et al. [2015] estimates livestock emissions for SoCAB to be 52±15 Gg CH_4/yr, which is consistent with the CALGEM prior (44 Gg CH_4/yr). Last, Cui et al. [2015] also estimated a combined CH_4 emission of 347±71 Gg CH_4/yr for the landfill and natural gas sectors. This also supports the suggestion that natural gas emissions are likely larger than the CALGEM prior for natural gas, because their minimum estimate (276 Gg; maximum = 418 Gg) for the landfill and natural gas sectors is larger than that of the CALGEM prior for natural gas and landfills together (268 Gg).Taken together, the above comparisons suggest the following: (1) the natural gas emission in SoCAB is likely higher than the

CALGEM prior (CARB inventory), and (2) the total for the landfill, wastewater and livestock sectors are likely similar to the prior. Note that the natural gas, landfill, wastewater and livestock sectors of the CALGEM prior account for 96% of the total in SoCAB.

In summary, our measurement network across California constrains CH_4 emissions from California's urban and rural emissions, and the added measurement sites to the CH_4 network significantly reduced the posterior uncertainty estimates. This suggests that the inverse framework based on the measurement network can be an effective approach to quantifying emissions at the regional scale and monitoring long-term spatial and temporal changes in emissions. Although the CO comparison and the fossil fuel CO_2 emission estimates appear largely consistent with expectation, it is possible that undiagnosed sources of error affect the CH_4 emission estimates. In the future, a combination of improved prior emission and meteorological models, expanded multi-gas measurements, and inverse model analyses will reduce uncertainty in California's GHG emissions. Also, more efforts are needed to constrain emissions by both sector and region. For example, while our results and other studies indicate both livestock and natural gas emissions appear to be underestimated, attribution of the magnitude of errors to specific sectors is difficult. Given the importance of distinguishing the regional variations in dominant CH_4 sources (e.g., Central Valley vs. SoCAB), a combination of facility specific emission measurements and regionally representative measurements of source-specific tracers (e.g., CO, VOCs, and potentially CH4 isotopes) [Townsend-Small et al., 2012; Peischl et al., 2013; Guha et al., 2015] are likely to prove useful in the future.

3.4. Nitrous Oxide

3.4.1. State Total Emissions

State total anthropogenic N_2O emissions were estimated by optimizing scaling factors (i.e., **λ)** given the multi-site measurements and multiplying them by the CARB-scaled EDGAR prior emissions (see Figure 3 for each region). We estimated a scaling factor for each 0.3° pixel (total = 183 pixels) within the major emission regions (i.e., SV, SF, SJV and SC), which account for 72% of the total prior emission. For the other eleven regions, we estimated a scaling factor for each region. Posterior emissions were estimated for both ocean and natural forest sources (one estimate for each), but those emissions were excluded from comparison to the anthropogenic CARB inventory. We note that the fractions of monthly mean predicted mixing ratios for ocean and forest are less than ~10% of the total predicted mixing ratio (not emission) both before and after inversion in most sites except for the coastal site, STR. Note that although the total ocean emission from the prior emission map is comparable to the state total emission, ocean emissions are weighted by the weak footprint in the ocean (as compared to those on land), yielding generally less than 10% of the total mixing ratio at most sites. This low fraction of the ocean mixing ratio relative to the total mixing ratio agrees with the finding in Xiang et al. [2013] who reported only 0.2 – 0.3 ppb enhancements were explained by the ocean along California's coast during early summer of 2010. This suggests that anthropogenic emissions are dominant sources of N_2O in California, as assumed by previous studies (e.g., Jeong et al. [2012b], Kort et al. [2008]). The fraction of ocean and forest contribution to the total prediction is provided by month and site in Appendix M. Figure 31 compares predicted and background-subtracted measured N_2O using all data (used in the inversion) available for each season and shows linear regression analysis results. Before inversion, the regression analysis estimates best-fit slopes to be 0.47 – 0.62 (predicted vs. measured). This simple analysis without full consideration of errors suggests that N_2O emissions are lower than those implied by the measurement by ~50%. After inversion, the best-fit slope, root-mean-square error (RMSE) and coefficient of determination (R^2) for each season are significantly improved.

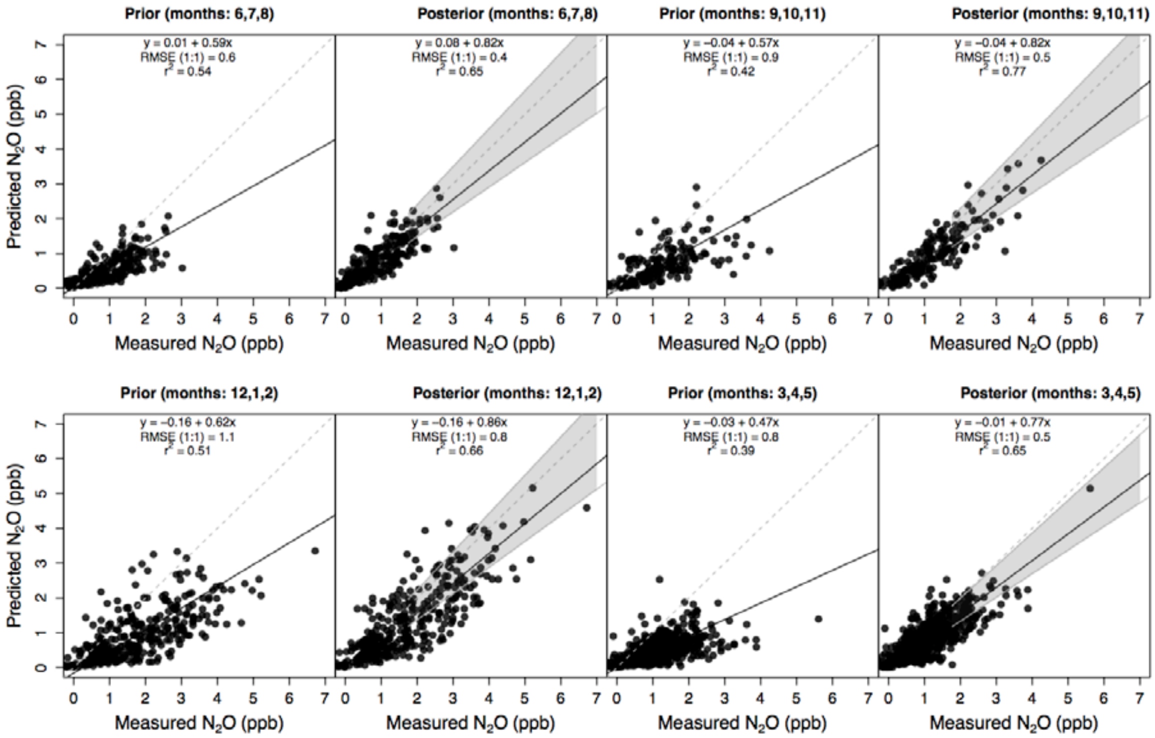

Figure 31. Comparison of predicted and measured N_2O mixing ratios before (prior) and after (posterior) inversion for each season. The gray dashed line indicates the 1:1 line and the black solid line represents the best fit for the data shown. The regression coefficients in the posterior plot were calculated based on the median values of the 50000 MCMC samples. The gray shaded area in the posterior plot represents the 95% uncertainty region for the regression analysis using 50000 MCMC samples.

The HBI analysis estimates the state total annual anthropogenic emission is 67 - 108 Gg N_2O/yr (at 95% confidence). Note that in this study we mostly report an interval of probable emissions since HBI produces a probability distribution (instead of mean and standard error) from posterior samples that is not exactly symmetric unlike that of the non-hierarchical Bayesian inversion (e.g., Jeong et al. [2012b, 2013] and Wecht et al. [2014]). An example of the histogram from the posterior distribution is shown in Figure 32. The posterior state total emissions are 1.4 – 2.3 times larger than the prior total used in inverse modeling (i.e., hybrid inventory which estimates emissions at 48 Gg N_2O/yr, see Table 8) and 1.5 – 2.5 times larger than the current CARB inventory (which estimates 2013 N_2O emissions at 44 Gg N_2O/yr). This result is generally consistent with that of Jeong et al. [2012b] where their annual N_2O emission estimates for central California during 2008 - 2009 were more than twice the state inventory. Jeong et al. [2012b] used a single tower (WGC, see Figure 3) located in central California and could not effectively constrain the southern San Joaquin and southern California regions. However, when we conducted inverse analysis for the 2008-2009 period using the updated background, emission maps and meteorology, the posterior emission (28 ± 10 Gg N_2O/yr at 95%

confidence) was lower than the previous result of 38 ± 14 Gg N_2O/yr reported by Jeong et al. [2012b] although the two results are statistically consistent (at 95% confidence). The updated background was prepared using the measurements in the Pacific Ocean only, which is more relevant to California and is expected to be more accurate. Also, the new emission maps include emissions from both ocean and natural forest and would separate the anthropogenic emissions better than the previous analysis in Jeong et al. [2012b]. The difference between the two results is likely the result of a combination of different background, prior emissions and meteorology.

As noted in the method section (Section 2), transport model error could affect the estimate of N_2O emissions. Comparison of predicted and measured CO mixing ratios at the four towers during June 2013 – May 2014 (Section 3.1) yields near-unity slopes for the majority of sites and seasons, suggesting that the WRF-STILT simulations are sufficient to estimate emissions of CO and likely other GHGs across California to within 10% ± 10% at 95% confidence level on annual timescales. Based on this mean result, we add a mean transport bias uncertainty of 10% in quadrature to our Bayesian statistical uncertainty estimates to estimate total uncertainty in annual state-total GHG emissions. After adding the transport bias uncertainty, we estimate state annual anthropogenic N_2O emissions to be 87 ± 22 Gg N_2O/yr (at 95% confidence including transport bias uncertainty), higher (1.5 - 2.5 times) than the anthropogenic emission in CARB's current inventory (44 Gg N_2O/yr in 2013). As in the CH_4 analysis (see Section 3.3.1), we note that the estimated N_2O emissions drop to 1.3 - 2.3 times the 2013 CARB inventory if we correct for the 10% median N_2O emissions assuming the bias in CO is applicable to N_2O. Undiagnosed sources of uncertainty may increase these error bounds beyond that indicated here. We also note that the transport error analysis based on CO rests on an unproven assumption that *a priori* annual state total CO emissions are known to better than 10%, though Brioude et al. [2013] found that a comparison of measured and predicted CO (using the WRF-FLEXPART model) agreed to within about 15% for aircraft flights over SoCAB conducted in May and June, 2010.

We also estimate statewide N_2O emissions for each season because measurements are available for a full annual analysis (June 2013 – May 2014). Figure 32 shows the comparison between the prior state total emission and the posterior emission for each season. For all seasons, the posterior emissions are higher than the prior emissions. Spring season may have slightly larger emissions compared to the other seasons though they are similar within error. This seasonal analysis result is consistent with earlier work by Jeong et al. [2012b] that found N_2O emissions for central California varied from 1.6(±0.3 at 68% confidence) to 2.4(±0.4 at 68% confidence) times the EDGAR prior (18.7 Gg N_2O/yr) from winter to summer, respectively. For another comparison, Xiang et al. [2013], applied airborne N_2O measurements across California's Central Valley during late May – early June of 2010 to estimate that state total N_2O emissions for that period. Despite using different spatial model for the prior emissions, the Xiang et al. [2013] also found N_2O emissions were larger than expected during the early summer period. Last, we note that the similarity of average summer emissions suggests that the spatial averaging afforded by the large (~ 50 - 100 km) footprints of the measurements reduce sensitivity to episodic N_2O emissions from management in individual fields (e.g. irrigation and fertilization).

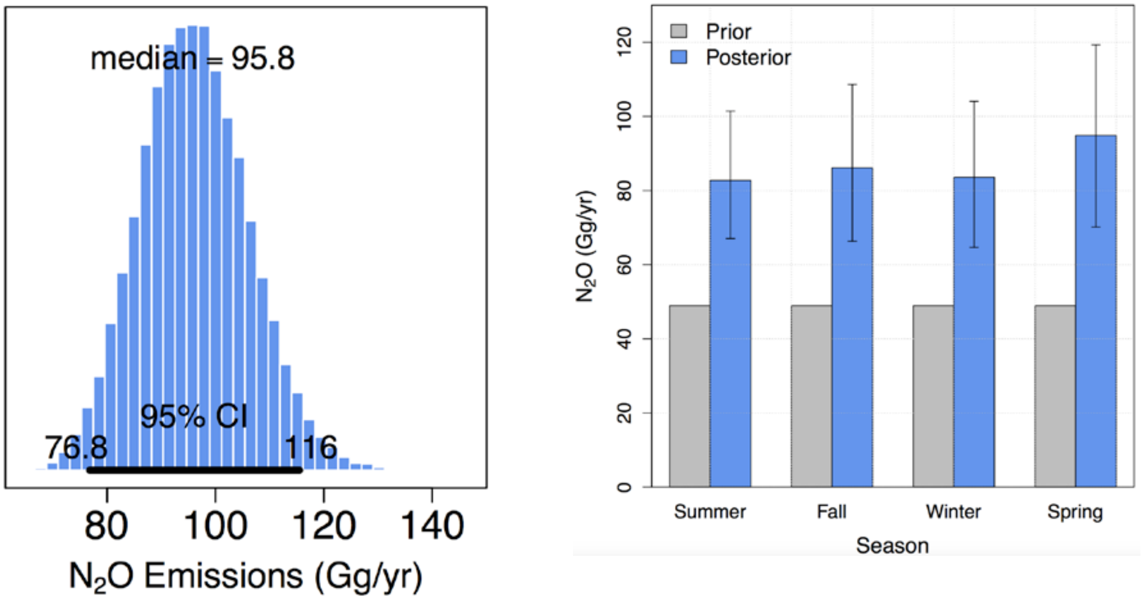

Figure 32. Example of histogram for the samples (May 2014 result) from the posterior distribution (left) and the inferred anthropogenic N_2O emissions (right) for four seasons: summer (JJA), fall (SON), winter (DJF) and spring (MAM). The error bar represents the 95% confidence interval around the posterior median emission estimate. In the histogram plot, the 95% confidence interval is shown at the bottom with the median value at the top.

3.4.2. Emissions in Rural and Urban Regions

The hierarchical Bayesian inversion using multiple sites across California constrains N_2O emissions from a significant portion of expected emissions in both rural and urban regions of California. In particular, using measurements from three sites (CIT, SBC, STR), the inverse analysis in this study yields a significant reduction in the posterior uncertainty for the urban regions of California (e.g., SoCAB), which were not constrained well in the previous study [Jeong et al., 2012b].

We first examine the emissions for the rural regions of California, focusing on the Central Valley. Figure 33 shows the comparison between prior and posterior emissions for the major emission regions that account for 72% of the state total in the prior emission, including the Central Valley of California (see Table 20 for all regions). We estimate that the Central Valley (Regions 3 and 8) emissions are 30.3 – 49.6 Gg N_2O/yr (at 95% confidence). This result suggests that the inferred posterior emissions are larger than the prior emissions (22.3 Gg N_2O/yr) for the Central Valley by factors of 1.4 – 2.2.

The spatial distribution of anthropogenic posterior emissions is shown in Figure 34 along with comparison with the CARB-scaled EDGAR prior emission field. As can be seen in the figure, the posterior emissions for some of the pixels in the Central Valley are significantly larger than the prior. However, it should be noted that the uncertainty range for those pixels is also large. This result shows that although the emissions at the sub-regional scale are well constrained in the Central Valley, the emission uncertainties for many of the individual pixels are still high.

For urban N_2O emissions of California, we focus on emissions from the two major urban regions (SoCAB and SF). According to the prior emission map, these urban regions account for 26% of the state's total N_2O emission. The HBI analysis estimates a total of 8.1 – 14.6 Gg N_2O for SoCAB (Region 12, at 95% confidence), which is 0.9 – 1.7 times the prior. We estimate the SF N_2O emissions to be 4.4 – 13.1 Gg N_2O/yr, which are 1.1 – 3.2 times the prior. Comparing the two regions, we find that the posterior uncertainty for SoCAB is smaller than that of SF. This is because we have two sites (CIT and SBC) with in-situ measurements that constrain SoCAB while SF is relatively weakly constrained by a discrete sampling site (STR, once a day) and the WGC tower with in-situ measurements in the Valley. Combining the emissions from the two major urban regions, we estimate the posterior emissions for the two regions to be 14.3 – 25.4 Gg N_2O/yr (at 95% confidence), which are larger than the prior by factors of 1.1 – 2.0. Since the spatially explicit EDGAR prior emissions were scaled to CARB's inventory by source sector, with the addition of personal product use in the IPU sector from EDGAR, comparison with CARB's inventory for the urban regions requires an assumption about the spatial distribution of N_2O emissions. If EDGAR's spatial distribution of N_2O emissions is applied to the urban regions, the HBI analysis result suggests that the actual urban N_2O emissions in California are only marginally higher than CARB's inventory. However, Xiang et al. [2013] suggested that the EDGAR inventory does not appear to provide good spatial representation of surface emissions in California's Central Valley. In this study, we first scaled the EDGAR emissions to match CARB's inventory by sector. Also, we used pixel-based inversion with a very large uncertainty (>100%) for the prior emissions to allow adjustment for potentially misrepresented emissions with more flexibility. We expect that this approach improved the estimate of N_2O emissions compared to previous work [Jeong et al., 2012b]. As shown in the comparison between plots of prior and posterior predictions to actual measurements (Figure 31), the posterior shows much higher correlations (R^2>0.6 for all seasons) than those of the prior. That said, it would still be advantageous to develop spatiotemporally explicit California-specific N_2O emissions maps.

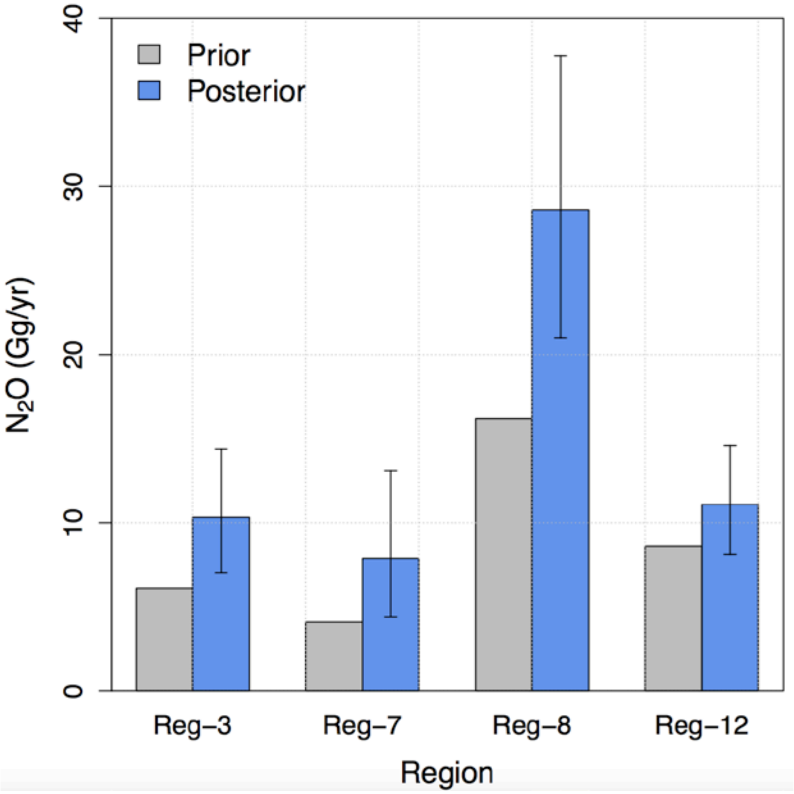

Figure 33. Estimated annual N_2O emissions for the major emission regions (at 95% confidence). Regions 3, 7, 8 and 12 represents the Sacramento Valley (SV), San Francisco Bay Area (SF), San Joaquin Valley (SJV) and South Coast (SC) air basins, respectively.

Table 20. Posterior Annual Anthropogenic N_2O Emissions (Gg N_2O/year) by Region

Region[a]	1 (NEP)	2 (NC)	3 (SV)	4 (MC)	5 (LC)	6 (GBV)	7 (SF)	8 (SJV)	9 (NCC)	10 (MD)	11 (SCC)	12 (SC)	13 (SS)	14 (SD)	15 (LT)
Prior	1.6	1.1	6.1	1.5	0.2	0.5	4.1	16.2	1.5	1.9	2.2	8.6	1.6	1.4	0.0
HBI Posterior[b]	10.2	5.5	14.4	6.8	0.8	3.3	13.1	37.8	10.0	13.9	16.0	14.6	8.7	4.9	0.1
HBI Posterior[c]	0.1	0.1	7.0	0.1	0.0	0.0	4.4	21.0	0.1	0.1	0.1	8.1	0.1	1.0	0.0

[a] Region abbreviations are shown in the parentheses.

[b] 97.5th percentile

[c] 2.5th percentile

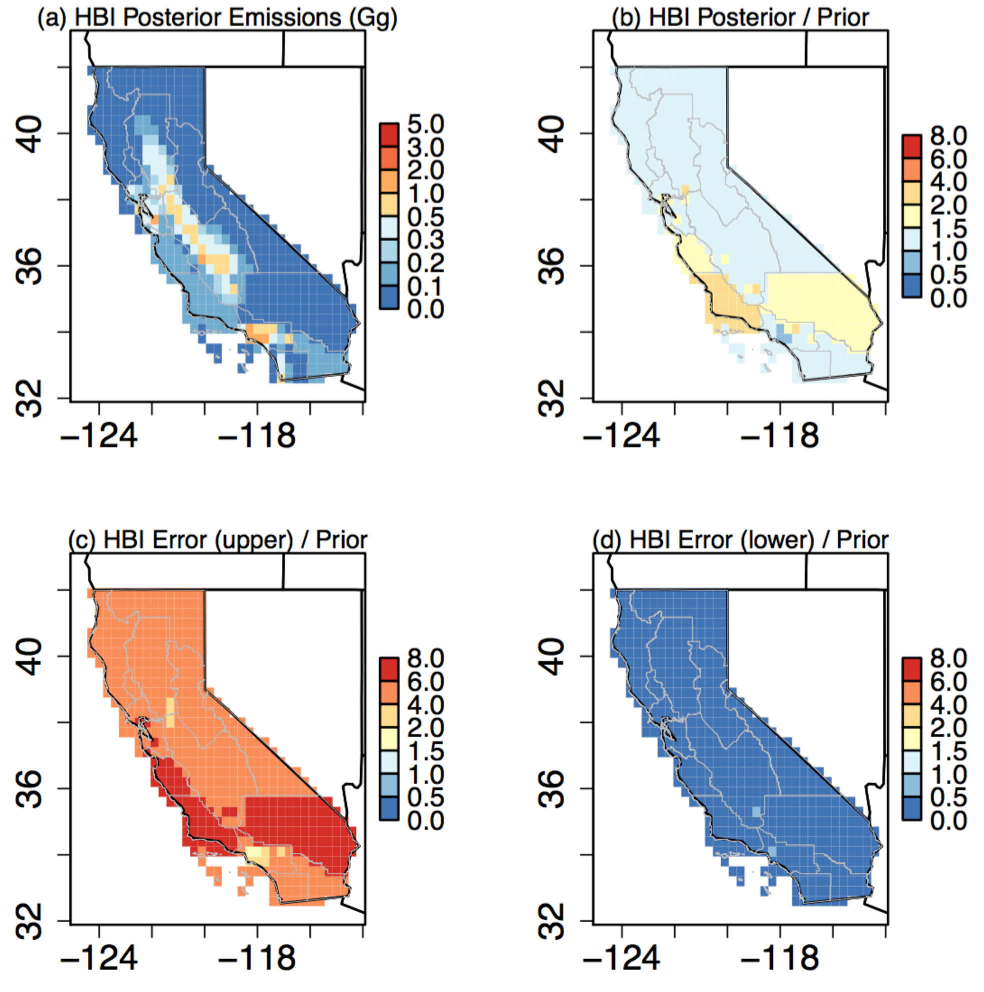

Figure 34. Estimated anthropogenic annual N_2O emissions from the HBI analysis: (a) posterior (median) annual emissions (Gg N_2O/yr), (b) ratio of posterior to prior, (c) ratio of estimated 97.5th percentile to prior, and (d) ratio of estimated 2.5th percentile to prior.

3.4.3. Further Discussion

Source attribution of emissions provides important information in planning mitigation strategies, allowing for prioritizing target sectors. We investigate the likely sources of emissions in the rural and urban regions of California using the results from this study and previous studies. We estimate N_2O emissions from different sources assuming the spatial distribution of the CARB-scaled EDGAR emission model, with the caveat that its spatial patterns may not be always correct. Based on this assumption, we scale individual source prior emissions at each pixel or region by the corresponding inferred scaling factor from the HBI analysis to obtain posterior source sector emissions. Figure 35 shows posterior annual emissions for major source sectors estimated from the HBI analysis (see Appendix N for all 12 source sectors). We estimate agricultural soil direct N_2O (AGS) emissions to be 21.6 - 37.3 Gg N_2O/yr (at 95% confidence), which are 1.4 – 2.4 times the prior while indirect N_2O (N2O) emissions are 6.2 – 10.7 Gg N_2O/yr (1.4 – 2.4 times the prior). This is consistent with the larger inferred emissions for the Central Valley (see Figure 33 and Table 20) as well as a recent study that attributed a large portion of the increase in global atmospheric N_2O to the use of fertilizers [Park et al., 2012].

Although the agricultural soil sector accounts for the largest portion of the state total N_2O emission, its relative contribution to the total is lower in California compared to that of the US N_2O emission. While our HBI analysis suggests that posterior agricultural soil emissions (direct and indirect N_2O from soils) are ~43% of the state total posterior emission, US EPA estimates agricultural soils account for ~74% of the US total (1.19 Tg N_2O/yr for the year 2013) N_2O emissions [US EPA, 2015]. This relatively low ratio of agricultural soil to the total is supported by the result in the previous section where the annual posterior emission (across sectors) for the Central Valley dominated by the agricultural industry was ~50% of the state total. This result also suggests that other N_2O source emissions from non-agricultural regions (e.g., SF, SoCAB) of California are important. Note that non-agricultural sources (all sectors excluding AGS, N2O and MNM) account for ~36% of the total posterior emissions.

The HBI analysis indicates that the second largest sources of N_2O emissions in California are likely manure management (MNM) and industrial processes and product use (IPU) (Figure 35). The posterior emissions from the two sectors are statistically indistinguishable although the IPU emissions (emissions from chemicals and solvents, e.g., nitric acid, adipic acid and caprolactam; http://edgar.jrc.ec.europa.eu/ingos/JRC-INGOS-report.pdf) are slightly larger than those of the MNM sector (9.7 vs. 9.5 Gg N_2O/yr) based on the prior emission model. Although the MNM and IPU posterior emissions are similar within error (12.6 – 23.9 vs. 10.8 – 19.4 Gg N_2O/yr, Figure 35), the deviation of the posterior estimate from the prior is larger in the MNM sector than in the IPU sector. Assuming the spatial distribution of the EDGAR prior model, our HBI analysis suggests that the total posterior MNM emission is 1.5 – 2.1 times higher than the prior estimate. This is possibly a result that is significant based on the findings by Owen and Silver [2015] where they compared N_2O manure management emission rates from published field-scale measurements with those predicted by the IPCC Tier 2 modeling approach. When they applied the revised emission factors based on the published field measurements to the US, the N_2O emissions from solid manure piles and anaerobic lagoons alone (included in the MNM sector) increased by an order of magnitude (5 – 13 times the US EPA estimate of 1.7 Gg N_2O/yr). This increased emission in the two (solid manure files and anaerobic lagoon) subsectors is equivalent to 11 – 37 % of the total MNM N_2O emission from US EPA [EPA, 2015].

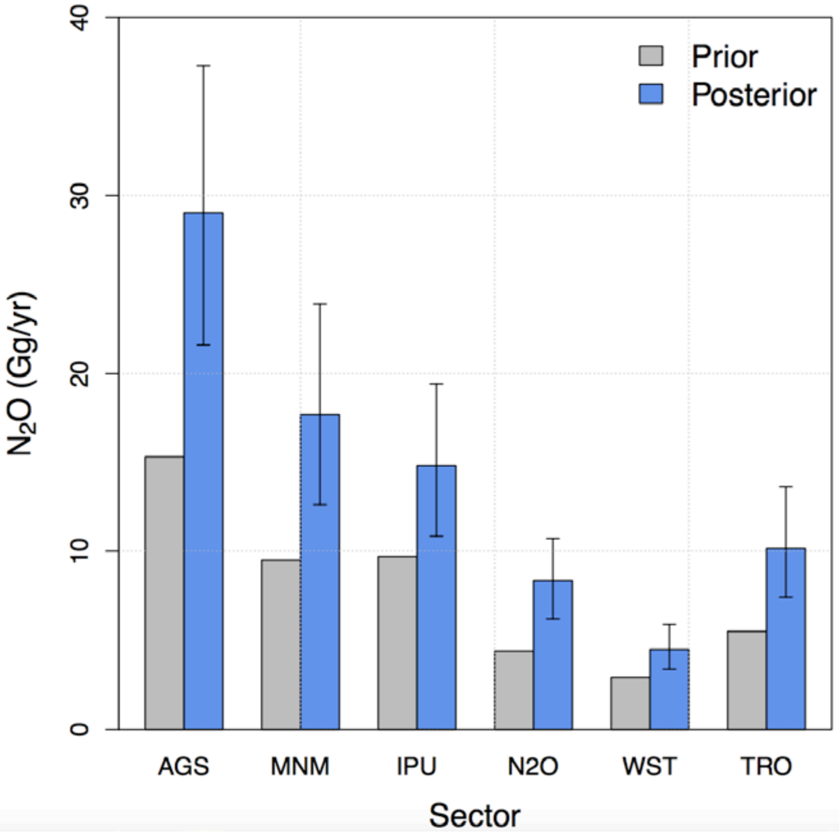

Figure 35. Posterior anthropogenic emissions (Gg N_2O/yr) from the HBI analysis for major source sectors: agricultural soils (AGS), manure management (MNM), industrial processes and product use (IPU), indirect N_2O emissions from agriculture (N2O), waste (solid & wastewater) (WST), road transportation (TRO). The error bar represents the 95% confidence interval. The comparison for all sectors including minor sectors (e.g., TRN) is provided in Appendix N.

The HBI analysis suggests that posterior MNM N_2O emissions account for 15 - 28% of the state total posterior N_2O emission, similar to the prior emissions which indicate 20% of N_2O is from manure management. Nationally, US EPA estimates the manure accounts for only 5% of the US total N_2O in 2013. However, Guha et al. [2015] report dairy and other livestock contribute 60 – 70% of the daily enhancement of N_2O using measurements near Bakersfield (southern San Joaquin Valley, Region 8 in this study), California during May – June 2010. Although their estimate for the uncertainty based on a bootstrapping method (100 runs) is large (~33%) and the analysis is limited temporally and spatially to represent the entire California, their result suggests that the contribution of the MNM sector in California is likely much larger than the national average, in agreement with posterior emissions and the CARB inventory. In addition, this result for MNM emissions is supported by recent CH_4 emissions studies in California (e.g., Jeong et al. [2013], Gentner et al. [2014]), which suggested that dairy livestock is the dominant source of CH_4 emissions in the Central Valley. Note that in California the total CH_4 emission from dairy MNM is slightly larger than that of dairy enteric fermentation (55 vs. 45%) [CARB, 2014].

Next, we further discuss the likely seasonality in California N_2O emissions based on the results in the previous section (see Figure 32 for seasonal emissions) and other work. Miller et al. [2012] reported that the estimated N_2O emissions from the Midwest US during early summer (fertilizer application season) were three times those in winter and twice the annual average. Xiang et al. [2013] applied this strong seasonality to extrapolate N_2O emissions from those early summer observations to estimate California annual emissions of 49 – 83 Gg N_2O/yr, which is marginally consistent with those of this study (75 – 97 Gg N_2O /yr, at 68% confidence). However, we note that the emissions in the mid-western region of the US are governed by strong seasonal climate variations in the continental interior and result in seasonality in agricultural activities. The strong correlation between climate, agricultural activities, and emissions in the Midwest US [Miller et al., 2012] indicates that we might expect smaller seasonality in California N_2O emissions because the milder climate in California has smaller seasonal temperature variations and hence more continuous agricultural activities.

In summary, our measurement network across California constrains N_2O emissions from California's urban and rural emissions, and the added measurement sites to the N_2O network significantly reduced the posterior uncertainty estimates over previous studies. This suggests that the inverse framework based on the tower network of measurements can be an effective approach to quantifying emissions at the regional scale and monitoring long-term spatial and temporal changes in emissions. Our study results reinforce the understanding that a large portion of the increase in global atmospheric N_2O can be attributed to the use of fertilizers [Park et al., 2012] and agricultural activities are likely a significant source of anthropogenic N_2O emissions in California [Jeong et al., 2012b, Xiang et al., 2013]. Our results also indicate that seasonal variations in California's N_2O emissions are relatively small compared to that of the Midwestern region of the US. However, to further characterize seasonal and interannual variability of emissions that are affected by weather patterns, fertilizer use and crop production [US EPA, 2015], more measurements with better temporal and spatial coverage are required. Although the CO comparison and the fossil fuel CO_2 emission estimates appear largely consistent with expectation, it is possible that undiagnosed sources of error affect the N_2O emission estimates. In the future, a combination of improved prior emission and meteorological models, expanded multi-gas measurements, and inverse model analyses will reduce uncertainty in California's GHG emissions.

4. Summary and Conclusions

- This study continued measurements of all major GHGs at the WGC tall-tower in central California, implemented full-suite GHG measurements at a tower in San Bernardino (SBC) and brought together measurements in a collaborative ground-based GHG measurement network across California. The combined network conducted GHG measurements for $ffCO_2$ (from 3 sites), CH_4, (13 sites) and N_2O (6 sites), significantly increasing its network density compared to those of Jeong et al. [2012a,b] and Jeong et al. [2013]. In particular, the expanded GHG network is now likely to be effective in constraining CH_4 and N_2O emissions from California's major urban and rural regions, and provided (albeit limited) spatial coverage for $ffCO_2$ emissions in both central and southern California.

- This study assessed the uncertainty in WRF-STILT transport model predictions using a combination of meteorological and CO measurements. Comparing model predictions with CO measurements from four tower sites in California from June 2013 through May 2014, we assessed the seasonal biases and random errors in predicted CO mixing ratios. In general, the seasonal mean biases in boundary layer wind speed ($< \sim 0.5$ m s^{-1}), direction ($< \sim 15°$), and boundary layer height ($< \sim 200$ m) are not statistically significant and small compared to random errors (~1.5 – 3.0 m s^{-1} for wind speed; ~ 40 - 60° for wind direction; ~ 300-500 m for boundary layer height). Comparison of predicted and measured CO mixing ratios at the four towers yield near-unity slopes (i.e., within 1.0 ± 0.20) for the majority of sites and seasons, though a subset of sites and seasons exhibit larger (~ 30%) uncertainty, particularly when weak winds are combined with complex terrain in the southern Central Valley. Looking across sites and seasons, these results suggest that the WRF-STILT simulations are sufficient to estimate emissions of CO and likely other GHG's across California to within 10% ± 10% (at 95% confidence) on annual timescales, assuming uncertainty in the CO emission is ~10%.

- Regional inversions using radiocarbon $^{14}CO_2$ observations for 2009 – 2012 from the central California site (i.e., WGC) suggest fossil fuel CO_2 emissions are higher in winter and spring and lower in summer and fall, approximately consistent with variations in estimated natural gas usage. Taking all years together, we estimate $ffCO_2$ emissions from central California are within 6% ± 20% of the prior estimate for that region. Inversions using measurements in SoCAB during June 2013 - May 2014 suggest that emissions in SoCAB are 11% ±20% larger than the prior estimate for that region, though with less seasonality. Combining the analysis results from central California and SoCAB, these results indicate emissions are within ~10% of the prior estimate with larger seasonal variations in the Bay Area compared with SoCAB. Although the emissions in central California and SoCAB are generally consistent with the prior emission, more measurements in the Central Valley and major urban regions are necessary to evaluate the statewide total ffCO_2 emission and its seasonality in California.

- Using measurements from 13 sites across California, the hierarchical Bayesian inversion for CH_4 constrains a significant portion of emission regions including the Central Valley and the southern California region. Summing across all regions of California, posterior CH_4 emission results suggest that state annual anthropogenic CH_4 emissions are higher (1.2 - 1.8 times at 95% confidence) than the anthropogenic emission in CARB's current 2013 GHG inventory. The estimated CH_4 emissions drop to 1.0 - 1.6 times the CARB inventory if results are corrected for the 10% median CH_4 emissions assuming the model bias in CO is applicable to CH_4. The CH_4 emissions from the Central Valley and urban regions (San Francisco Bay and South Coast Air Basins) account for 58% and 26 % of the total posterior emissions, respectively. For emission sources, this study combined with other studies (e.g., analysis from VOC measurements as in Gentner et al. [2014]) suggests the livestock sector is likely the major contributor to the state total CH_4 emissions.

- Using N_2O measurements from six sites across California, hierarchical Bayesian inversion estimates state annual anthropogenic N_2O emissions to be higher (1.5 – 2.5 times at 95% confidence) than the current 2013 CARB inventory. The estimated N_2O emissions drop to 1.3 - 2.3 times the CARB inventory if corrected for the 10% median N_2O emissions assuming the model bias in CO is applicable to N_2O. Our study results reinforce the understanding that a large portion of the increase in global atmospheric N_2O can be attributed to the use of fertilizers [Park et al., 2012] and agricultural activities (manure management) are likely a significant source of anthropogenic N_2O emissions in California [Jeong et al., 2012b, Xiang et al., 2013]. Our results also indicate that seasonal variations in California's N_2O emissions are relatively small compared to that of the Midwestern region of the US. However, to further characterize seasonal and interannual variability of emissions that are affected by weather patterns, fertilizer use and crop production [US EPA, 2015], more measurements with better temporal and spatial coverage are required.

- In summary, while the ffCO_2 emission, which accounts for 84% of the total GHG in California [CARB, 2015], are similar to the CARB inventory in central and southern California regions, this study shows that the state inventory underestimates both CH_4 and N_2O emissions. In particular, this full annual analysis reinforces the previous study result that actual CH_4 and N_2O emissions in the Central Valley region are higher than the state inventory.

5. Recommendations

- The assessment of transport modeling in California using CO measurements and meteorological observations suggests that the WRF-STILT simulations are sufficient to estimate emissions of CO and likely other GHGs across California to ~20% (at 95% confidence) at annual and state total scales. While the approach taken in this study is a significant advance for transport evaluation, the evaluation was performed based on observations from a limited number of meteorological stations. In particular, there are only few continuous meteorological upper air and boundary layer depth measurements for some of the sub-regions of California available for evaluation of transport modeling. Hence, although the CO comparison and the fossil fuel CO_2 emission estimates appear largely consistent with expectation, it is possible that undiagnosed sources of error affect the CH_4 and N_2O emission estimates. In the future, additional meteorological measurements including upper air observations in the Bay Area and the southern San Joaquin Valley as well as the coastal urban region of southern California will improve evaluation of transport modeling that will contribute to long-term monitoring of GHGs in California. For the sub-regions with relatively larger uncertainties than others due to complex topography and seasonally varying meteorology, we expect that high-resolution modeling would be very useful in resolving sub-regional and local variations in emissions. In addition, our transport assessment results show that transport model simulations with a single configuration of parameters and schemes (e.g., land surface scheme) cannot easily reproduce the surface and upper air meteorological conditions in California. For future studies, a combination of multi-model simulations and mass-conserving data assimilation might further reduce biases in transport and emission estimates.

- While the $ffCO_2$ emission, which accounts for the majority (>80%) of the total anthropogenic GHG emission in California, is similar to the state inventory in central and southern California regions, continued analysis that constrains statewide $ffCO_2$ emissions is necessary. In particular, it would be valuable for CARB to enhance the CO_2 emission inventory to include spatially and temporally explicit anthropogenic CO_2 emission model with uncertainties for use as a prior model in top-down analyses. This, together with expanded tower measurements of radiocarbon $^{14}CO_2$ in areas of the Central Valley as well as the major urban regions of California, will be particularly effective in improving statewide estimates of $ffCO_2$ emissions.

- Observations from the current CH_4 measurement network are effective for use in constraining emissions from both major urban and rural regions of California. Combined with other studies (e.g., analysis from VOC measurements), this study suggests the livestock sector is likely the major contributor to the state total CH_4 emissions and is underestimated from the state inventory. Although there is growing evidence that this is the case, further effort to attribute emissions to specific source sectors (e.g., landfills, livestock, petroleum and natural gas) will be valuable. In this regard, measurements of additional source specific tracers (e.g., VOCs, and potentially CH_4 isotopes) will help differentiate the contributions from the source sectors of CH_4, and facility scale measurements of manure emissions will be particularly helpful.

- Although this work took a major step forward to quantify N_2O emissions using multi-site observations over a year-long period, source speciation as well as further confirmation of the statewide total emission remains a challenge towards establishing mitigation strategies by source sector and region. Development of a spatially explicit N_2O emission maps including uncertainty estimates would be helpful in this regard, particularly if compared with facility specific measurements. We also suggest an expanded tower measurement network with well-calibrated instruments, in particular in the Central Valley where manure management and agricultural soils contribute significantly to the total emission. Finally, as with CH_4, we expect measurements of additional source specific tracers will help separate different sources of N_2O.

REFERENCES

A. E. Andrews, J. D. Kofler, M. E. Trudeau, J. C. Williams, D. H. Neff, K. A. Masarie, D. Y. Chao, D. R. Kitzis, P. C. Novelli, C. L. Zhao, E. J. Dlugokencky, P. M. Lang, M. J. Crotwell, M. L. Fischer, J. T. Lee, D. D. Baumann, A. R. Desai, C. O. Stanier, S. F. J. de Wekker, D. E. Wolfe, J. W. Munger, M. J. Parker, and P. P. Tans (2014), CO_2, CO and CH_4 measurements from the NOAA Earth System Research Laboratory's tall tower greenhouse gas observing network: instrumentation, uncertainty analysis and recommendations for future high-accuracy greenhouse gas monitoring efforts, Atmospheric Measurement Techniques, 6, 1461–1553.

Angevine, W. M., L. Eddington, and K. Durkee (2012), Meteorological model evaluation for CalNex 2010, Mon. Wea. Rev., 140, 3885–3906, doi:10.1175/MWR-D-12-00042.1.

BAAQMD (2015), Bay Area Emissions Inventory Summary Report: Greenhouse Gases Base Year 2011 (updated January 2015), http://www.baaqmd.gov/~/media/Files/Planning%20and%20Research/Emission%20Inventory/BY2011_GHGSummary.ashx?la=en (accessed May 2015)

Bagley, J. E., and J. Miller (2015), Biophysical impacts of climate smart agriculture in the Midwest United States, Plant, Cell and Environment, 38, 1913–1930,, doi:10.1111/pce.12485.

Bao, J.-W., S. A. Michelson, and P. Persson (2008), Observed and WRF-simulated low-level winds in a high-ozone episode during the Central California Ozone Study, J. Appl. Meteor. Climatol., 47, 2372–2394, doi:10.1175/2008JAMC1822.1.

Bergamaschi, P., M. Krol, F. Dentener, A. Vermeulen, F. Meinhardt, R. Graul, M. Ramonet, W. Peters, and E. J. Dlugokencky (2005), Inverse modelling of national and European CH_4 emissions using the atmospheric zoom model TM5, Atmos. Chem. Phys., 5, 2431–2460.

Bianco, L., and J. M. Wilczak (2002), Convective boundary layer depth: Improved measurement by Doppler radar wind profiler using fuzzy logic methods, J. Atmos. Oceanic Technol., 19(11), 1745–1758, doi:10.1175/ 1520-0426(2002)019<1745:CBLDIM>2.0.CO;2.

Bianco, L., J. Wilczak, and A. White (2008), Convective boundary layer depth estimation from wind profilers: Statistical comparison between an automated algorithm and expert estimations, J. Atmos. Oceanic Technol., 25, 1397–1413, doi:10.1175/2008JTECHA981.1.

Bianco, L., I. V. Djalalova, C. W. King, and J. M. Wilczak (2011), Diurnal evolution and annual variability of boundary-layer height and its correlation to other meteorological variables in California's Central Valley, Boundary Layer Meteorol., 140, 491–511, doi:10.1007/s10546-011-9622-4.

Brioude, J., et al. (2013), Top-down estimate of surface flux in the Los Angeles Basin using a mesoscale inverse modeling technique: assessing anthropogenic emissions of CO, NOx and CO_2, Atmospheric Chemistry and Physics, 13, 3661-3677. doi:10.5194/acp-13-3661-2013.

Bouwman, A.F., K.W. van der Hoek and J.G.J. Olivier (1995), Uncertainties in the global source distribution of nitrous oxide, J. Geophys. Res., 100, 2785-2800.

CARB (2014), California Greenhouse Gas Emissions Inventory. California Air Resources Board Staff Report, Accessed January 2015 (http://www.arb.ca.gov/cc/inventory/inventory.htm, version March 2014).

CARB (2015), California Greenhouse Gas Emissions Inventory. California Air Resources Board Staff Report, Accessed September 2015 (http://www.arb.ca.gov/cc/inventory/inventory.htm, version April 2015).

Chen, F. and J. Dudhia (2001), Coupling an Advanced Land Surface Hydrology Model with the Penn State NCAR MM5 Modeling System. Part 1: Model Implementation and Sensitivity, Mon. Weather Rev., 129, 569–585.

Cui, Y. Y., J. Brioude, S. A. McKeen, W. M. Angevine, S.-W. Kim, G. J. Frost, R. Ahmadov, J. Peischl, N. Bousserez, Z. Liu, T. B. Ryerson, S. C. Wofsy, G. W. Santoni, E. A. Kort, M. L. Fischer, and M. Trainer (2015), Top-down estimate of methane emissions in California using a mesoscale inverse modeling technique: The South Coast Air Basin. J. Geophys. Res. Atmos., 120, 6698–6711. doi: 10.1002/2014JD023002.

de la Rue du Can, S., T. Wenzel, and M. L. Fischer (2008), Spatial disaggregation of CO_2 emissions for the State of California, Environmental Energy Technologies Division, Lawrence Berkeley National Lab, LBNL-759E.

Dye, T. S., C. G. Lindsey, and J. A. Anderson (1995), Estimates of mixing depth from “boundary layer” radar profilers. Preprints from the 9th Symposium on Meteorological Observations and Instrumentation, Charlotte, NC, March 27-31, 156-160 (STI-94212-1451).

Fairley, D. and M. L. Fischer (2015). Top-Down Methane Emissions Estimates for the San Francisco Bay Area from 1990 to 2012, Atmospheric Environment, doi:10.1016/j.atmosenv.2015.01.065.

Ganesan A. L. et al. (2014), Characterization of uncertainties in atmospheric trace gas inversions using hierarchical Bayesian methods. Atmos. Chem. Phys., 14, 3855–3864, doi:10.5194/acp-14-3855-2014.

Gelman, A. and J. Hill (2007), Data analysis using regression and multilevel/hierarchical models, Cambridge University Press, New York, NY, USA.

Gelman A., J. B. Carlin, H. S. Stern, D. B. Dunson, A. Vehtari, and D. B. Rubin (2014), Bayesian data analysis (3rd Ed.), Chapman & Hall/CRC.

Gentner, D.R., et al. (2014), Emissions of organic carbon and methane from petroleum and dairy operations in California’s San Joaquin Valley, Atmos. Chem. Phys. 13, 28225–28278.

Gerbig, C, J. Lin, S. Wofsy, B. Daube, A. E. Andrews, B. Stephens, P. S. Bakwin and C. Grainger (2003), Toward constraining regional-scale fluxes of CO_2 with atmospheric observations over a continent: 2. Analysis of COBRA data using a receptor-oriented framework. J. Geophys. Res., 108(D24), doi:10.1029/2003JD003770.

Gerbig, C., S. Koerner, and J. C. Lin (2008), Vertical mixing in atmospheric tracer transport models: error characterization and propagation, Atmos. Chem. Phys., 8(3), 591–602.

Göckede, M., A. M. Michalak, D. Vickers, D. P. Turner, and B. E. Law (2010), Atmospheric inverse modeling to constrain regional-scale CO_2 budgets at high spatial and temporal resolution, J. Geophys. Res., 115, D15113, doi:10.1029/2009JD012257.

Guha, A., D.R. Gentner, R.J. Weber, R. Provencal, A. Gardner, and A.H. Goldstein (2015), Source apportionment of methane and nitrous oxide in California's San Joaquin Valley at CalNex 2010 via positive matrix factorization, Atmos. Chem. Phys. Discuss., 15, 6077-6124, doi:10.5194/acpd-15-6077-2015.

Gurney, K., D. Mendoza, Y. Zhou, M.L. Fischer, C. Miller, S. Geethakumar, and S. du Can (2009), High resolution fossil fuel combustion CO_2 emission fluxes for the United States, Environ. Sci. Technol., 43, 5535–5541.

Harding, K. J., and P. K. Snyder (2012), Modeling the atmospheric response to irrigation in the Great Plains. Part I: General impacts on precipitation and the energy budget, J. Hydrometeor, doi:10.1175/JHM-D-11-098.1.

Hofman, D. J., J. H. Butler, E. J. Dlugokencky, J. W. Elkins, K. Masarie, S. A. Montzka, and P. Tans (2006), The role of carbon dioxide in climate forcing from 1979 - 2004: Introduction of the Annual Greenhouse Gas Index, Tellus B, 58B, 614-619.

Hong, S., Y. Noh, and J. Dudhia (2006), A New Vertical Diffusion Pack- age with an Explicit Treatment of Entrainment Processes, Mon. Weather Rev., 134, 2318–2341, doi:10.1175/MWR3199.1.

Hsu, Y.-K., T. VanCuren, S. Park, C. Jakober, J. Herner, M. FitzGibbon, D. R. Blake, and D. D. Parrish (2010), Methane emissions inventory verification in southern California, Atmos. Environ., 44, 1 – 7, doi:10.1016/j.atmosenv.2009.10.002.

Intergovernmental Panel on Climate Change (2007), Climate Change 2007: The Physical Science Basis. Contribution of Working Group I to the Fourth Assessment Report of the Intergovernmental Panel on Climate Change, edited by S. Solomon et al., Cambridge University Press, Cambridge, U. K.

Janjić, Z. I. (1990), The step-mountain coordinate: Physical package, Mon. Weather Rev., 118, 1429–1443, doi:10.1175/1520-0493(1990)118<1429: TSMCPP>2.0.CO;2.

Jeong, S., C. Zhao, A. E. Andrews, L. Bianco, J. M. Wilczak, and M. L. Fischer (2012a), Seasonal variation of CH_4 emissions from central California. J. Geophys. Res., 117, D11306, doi:10.1029/2011JD016896.

Jeong, S., C. Zhao, A. E. Andrews, E. J. Dlugokencky, C. Sweeney, L. Bianco, J. M. Wilczak, and M. L. Fischer (2012b), Seasonal variations in N_2O emissions from central California. Geophys. Res. Lett., 39, L16805, doi:10.1029/2012GL052307.

Jeong, S., Y.-K. Hsu, A. E. Andrews, L. Bianco, P. Vaca, J. M. Wilczak, and M. L. Fischer (2013), A multitower measurement network estimate of California’s methane emissions, J. Geophys. Res. Atmos., 118, 11,339–11,351, doi:10.1002/jgrd.50854.

Jeong, S., D. Millstein, and M. L. Fischer (2014), Spatially explicit methane emissions from petroleum production and the natural gas system in California, Environ. Sci. Technol., 48, 5982–5990.

Jiménez, P A., and J. Dudhia (2012), Improving the representation of resolved and unresolved topographic effects on surface wind in the WRF Model., J. Appl. Meteor. Climatol., 51, 300–316, doi: http://dx.doi.org/10.1175/JAMC-D-11-084.1.

Korner-Nievergelt, F, T. Roth, S. von Felten, J. Guélat, B. Almasi, and P. Korner-Nievergelt (2015), Bayesian Data Analysis in Ecology Using Linear Models with R, BUGS, and Stan: Including Comparisons to Frequentist Statistics. Elsevier Science.

Kort, E. A., J. Eluszkiewicz, B. B. Stephens, J. B. Miller, C. Gerbig, T. Nehrkorn, B. C. Daube, J. O. Kaplan, S. Houweling, and S. C. Wofsy (2008), Emissions of CH_4 and N_2O over the United States and Canada based on a receptor-oriented modeling framework and COBRA-NA atmospheric observations, Geophy. Res. Lett., 35, L18808, doi:10.1029/2008GL034031.

Kueppers, L. M., and M. A. Snyder (2007), Irrigation cooling effect: Regional climate forcing by land- use change, Geophys. Res. Lett., 34, L03703, doi:10.1029/2006GL028679.

Kruschke, J. K. (2015), Doing Bayesian data analysis (2nd Ed.), Academic Press, 759 pp.

Lin, J. C., and C. Gerbig (2005), Accounting for the effect of transport errors on tracer inversions, Geophys. Res. Lett., 32, L01802, doi:10.1029/ 2004GL021127.

Lin, J. C., C. Gerbig, S. C. Wofsy, A. E. Andrews, B. C. Daube, K. J. Davis, and C. A. Grainger (2003), A near-field tool for simulating the upstream influence of atmospheric observations: The Stochastic Time-Inverted Lagrangian Transport (STILT) model. J. Geophys. Res., 108(D16), 4493, doi:10.1029/2002JD003161.

McKain , K. et al. (2015),
use in the urban region of Boston, Massachusetts, Proc Natl Acad Sci USA, 112 (7), 1941 – 1946, www.pnas.org/cgi/doi/10.1073/pnas.1416261112.

McKeigue, P. M., H. Campbell, S. Wild, V. Vitart, C. Hayward, I. Rudan, A. F. Wright, J. F. Wilson (2010). Bayesian methods for instrumental variable analysis with genetic instruments ('Mendelian randomization'): example with urate transporter SLC2A9 as an instrumental variable for effect of urate levels on metabolic syndrome, Int. J. Epidemiol, 39(3), 907-18. doi: 10.1093/ije/dyp397.

Mellor, G. L., and T. Yamada (1982), Development of a turbulence closure model for geophysical fluid problems, Rev. Geophys., 20, 851–875, doi:10.1029/RG020i004p00851.

Mesinger, F., G. DiMego, E. Kalnay, K. Mitchell, P. C. Shafran, W. Ebisuzaki, D. Jovic, J. Woollen, E. Rogers, E. H. Berbery, M. B. Ek, Y. Fan, R. Grumbine, W. Higgins, H. Li, Y. Lin, G. Manikin, D. Parrish, and W. Shi (2006), North American Regional Reanalysis. Bull. Amer. Meteor. Soc., 87 (3), 343-360.

Michalak, A. M., A. Hirsch, L. Bruhwiler, K. R. Gurney, W. Peters, and P. P. Tans (2005), Maximum likelihood estimation of covariance parameters for Bayesian atmospheric trace gas surface flux inversions, J. Geophys. Res., 110, D24107, doi:10.1029/2005JD005970.

Michelson, S. A., and J.-W. Bao (2008), Sensitivity of low-level winds simulated by the WRF model in California's Central Valley to uncertainties in the large-scale forcing and soil initialization, J. Appl. Meteor. Climatol., 47, 3131–3149, doi:10.1175/2008JAMC1782.1.

Miller, J. B., et al. (2012), Linking emissions of fossil fuel CO_2 and other anthropogenic trace gases using atmospheric $^{14}CO_2$, J. Geophys. Res., 117, D08302, doi:10.1029/2011JD017048.

Miller, S. M., et al.,(2012), Regional sources of nitrous oxide over the United States: Seasonal variation and spatial distribution, J. Geophys. Res., 117, D06310, doi:10.1029/2011JD016951.

Miller, S.M., et al. (2013), Anthropogenic emissions of methane in the United States, Proc Natl Acad Sci USA, 110(50): 20018–20022, doi:10.1073/pnas.1314392110.

Montzka, S. A., E. J. Dlugokencky, and J. H. Butler (2011), Non-CO_2 greenhouse gases and climate change. Nature, 476, 43-50.

Nehrkorn, T., J. Eluszkiewicz, S. C. Wofsy, J. C. Lin, C. Gerbig, M. Longo, and S. Freitas (2010), Coupled weather research and forecasting - stochastic time-inverted lagrangian transport (WRF-STILT) model. Meteor. Atmos. Phys., 107 (1), 51-64, doi:10.1007/s00703-010-0068-x.

Newman, S., X. Xu, H. P. Affek, E. Stolper, and S. Epstein (2008), Changes in mixing ratio and isotopic composition of CO_2 in urban air from the Los Angeles basin, California, between 1972 and 2003, J. Geophys. Res., 113, doi:10.1029/2008JD009999.

Newman, S., S. Jeong, M. L. Fischer, X. Xu, C. L. Haman, B. Lefer, S. Alvarez, B. Rappenglueck, E. A. Kort, A. E. Andrews, J. Peischl, K. R. Gurney, C. E. Miller, and Y. L. Yung (2013), Diurnal tracking of anthropogenic CO_2 emissions in the Los Angeles basin megacity during spring 2010, Atmos. Chem. Phys., 13, 4359–4372, doi:10.5194/acp-13-4359-2013.

Nakanishi, M. and H. Niino (2006), An improved Mellor Yamada level-3 model: its numerical stability and application to a regional prediction of advection fog, Bound. Layer Meteorol., 119, 397– 407.

National Research Council (2010), Verifying Greenhouse Gas Emissions: Methods to support international climate agreements, Natl. Acad. Press, Washington, D. C.

Owen, J., and W. L. Silver (2015), Greenhouse gas emissions from dairy manure management: a review of field-based studies, Global Change Biology, 21, 550–565, doi: 10.1111/gcb.12687.

Plummer, M. (2003), JAGS: A program for analysis of Bayesian graphical models using Gibbs sampling, Proceedings of the 3rd International Workshop on Distributed Statistical Computing (DSC 2003), March 20–22, Vienna, Austria. ISSN 1609-395X.

Park, S., et al. (2012), Trends and seasonal cycles in the isotopic composition of nitrous oxide since 1940, Nature Geosci., 5, 261 – 265, doi: 10.1038/NGEO1421.

Peischl, J., et al. (2013), Quantifying sources of methane using light alkanes in the Los Angeles basin, California, J. Geophys. Res. Atmos., 118, doi:10.1002/jgrd.50413.

Pillai, D., C. Gerbig, and R. Ahmadov (2011), High-resolution simulations of atmospheric CO_2 over complex terrain–representing the Ochsenkopf mountain tall tower, Atmos. Chem. Phys., 11, 7445-7464, doi:10.5194/acp-11-7445-2011.

Rasmussen, C. E., and C. K. I. Williams (2006), Gaussian Processes for Machine Learning, MIT Press, Cambridge, Massachusetts.

Ruiz, J. J., C. Saulo, and J. Nogue´s-Paegle (2010), WRF model sensitivity to choice of parameterization over South America: Validation against surface variables, Mon. Wea. Rev., 138, 3342–3355.

Sacks, W. J., B. I. Cook, N. Buenning, and S. Levis (2009), Effects of global irrigation on the near-surface climate, Clim Dyn, Climate Dynamics, 33(2), 159-175, doi:10.1007/s00382-008-0445-z.

Skamarock, W.C., J. B. Klemp, J. Dudhia, D.O. Gill, D. M. Barker, X. Z. Huang, W. Wang, and J. G. Powers (2008), A description of the advanced research WRF version 3. Technical Note 475+STR. Mesoscale and Microscale Meteorology Division, NCAR, Boulder, Colorado.

Smith, A., N. Lott, and R. Vose (2011), The integrated surface database: recent developments and partnerships, Bull Amer Met Soc, 92(6), 704–708, doi:10.1175/2011BAMS3015.1.

Sorooshian, S., J. Li, K.-l. Hsu, and X. Gao (2011), How significant is the impact of irrigation on the local hydroclimate in California's Central Valley? Comparison of model results with ground and remote-sensing data, J. Geophys. Res., 116, D06102, doi:10.1029/2010JD014775.

Strach, R. G., B. L. Weber, A. S. Frisch, C. G. Little, D. A. Merritt, K. P. Moran, and D. C. Welsh (1987), The precision and relative accuracy of profiler wind measurements, J. Atmos. Oceanic Technol., 4, 563–571, doi: http://dx.doi.org/10.1175/1520-0426(1987)004<0563:TPARAO>2.0.CO;2

Townsend-Small, A., S. C. Tyler, D. E. Pataki, X. Xu, and L. E. Christensen (2012), Isotopic measurements of atmospheric methane in Los Angeles, California, USA: Influence of "fugitive" fossil fuel emissions, J. Geophys. Res., 117, D07308, doi:10.1029/2011JD016826.

Turnbull, J., J. Miller, S. Lehman, P. Tans, R. Sparks and J. Southon (2006), Comparison of $^{14}CO_2$, CO, and SF_6 as tracers for recently added fossil fuel CO_2 in the atmosphere and implications for biological CO_2 exchange, Geophys Res Lett., 33(1), L01817.

US EPA (2015), Inventory of U.S. Greenhouse Gas Emissions and Sinks: 1990 – 2013, EPA 430-R-15-004 (http://www.epa.gov/climatechange/Downloads/ghgemissions/US-GHG-Inventory-2015-Main-Text.pdf).

Wecht, K. J., Jacob, D. J., Sulprizio, M. P., Santoni, G. W., Wofsy, S. C., Parker, R., Bösch, H., and Worden, J. (2014) Spatially resolving methane emissions in California: constraints from the CalNex aircraft campaign and from present (GOSAT, TES) and future (TROPOMI, geostationary) satellite observations, Atmos. Chem. Phys., 14, 8173-8184, doi:10.5194/acp-14-8173-2014.

Wennberg, P. O., W. Mui, D Wunch, E. A. Kort, D. R. Blake, E. L. Atlas, G. W. Santoni, S. C. Wofsy, G. S. Diskin, S. Jeong, and M. L. Fischer (2012), On the Sources of Methane to the Los Angeles Atmosphere. Environ. Sci. Technol., 46 (17), 9282 - 9289, doi:10.1021/es301138y.

Wong, K. W., Fu, D., Pongetti, T. J., Newman, S., Kort, E. A., Duren, R., Hsu, Y.-K., Miller, C. E., Yung, Y. L., and Sander, S. P. (2015) Mapping CH_4 : CO_2 ratios in Los Angeles with CLARS-FTS from Mount Wilson, California, Atmos. Chem. Phys., 15, 241-252, doi:10.5194/acp-15-241-2015.

Wunch, D., P. O. Wennberg, G. C. Toon, G. Keppel-Aleks, and Y. G. Yavin (2009), Emissions of greenhouse gases from a North American megacity, Geophys. Res. Lett., 36, L15810, doi:10.1029/2009GL039825.

Wyngaard, J. C., and M. A. LeMone (1980), Behavior of the refractive index structure parameter in the entraining convective boundary layer, J. Atmos. Sci., 37, 1573–1585.

Xiang, B., et al. (2013), Nitrous oxide (N_2O) emissions from California based on 2010 CalNex airborne measurements, J. Geophys. Res. Atmos., 118, 2809–2820, doi:10.1002/jgrd.50189.

Xu, X., S. E. Trumbore, S. Zheng, J. R. Southon, K. E. McDuffee, M. Luttgen and J. C. Liu (2007), Modifying a sealed tube zinc reduction method for preparation of AMS graphite targets: Reducing background and attaining high precision, Nucl. Instr. and Meth. in Phys. Res. B 259, 320–329.

Zhao, C., A. E. Andrews, L. Bianco, J. Eluszkiewicz, A. Hirsch, C. MacDonald, T. Nehrkorn, and M. L. Fischer (2009), Atmospheric inverse estimates of methane emissions from Central California. J. Geophys. Res., 114, D16302, doi:10.1029/2008JD011671.

APPENDICES

APPENDIX A. Recent trend of dairy cows in SoCAB

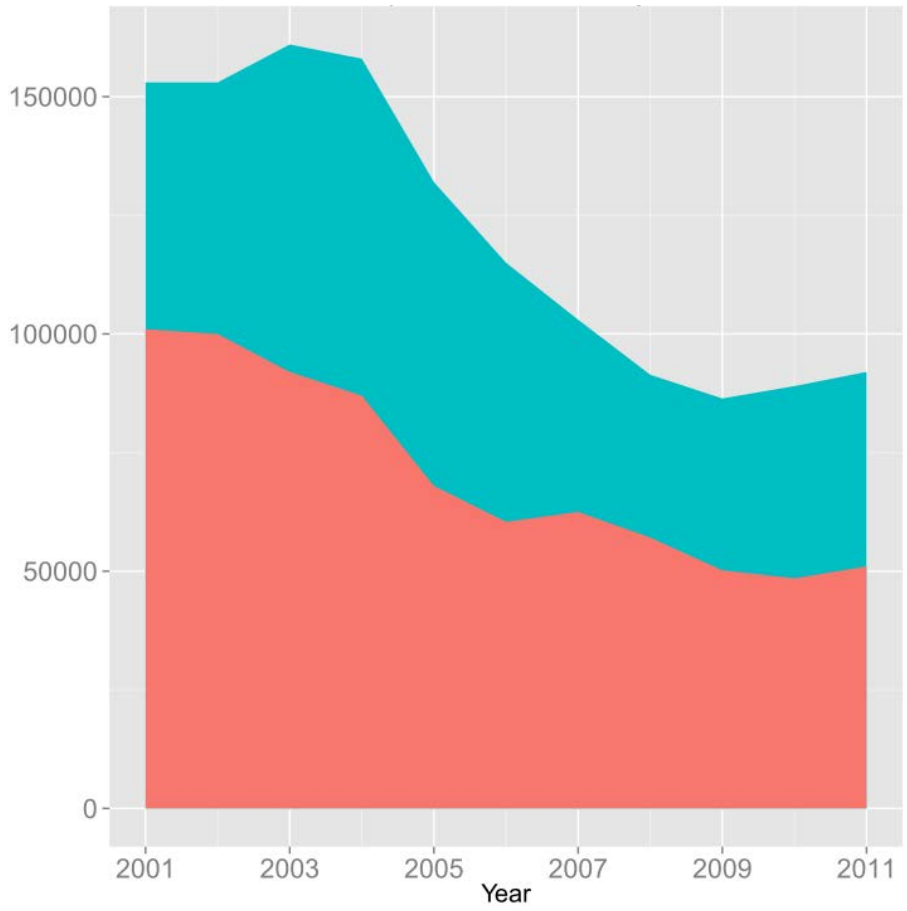

Recent trend of the number of dairy cows in the SoCAB counties (source: http://www.nass.usda.gov/Statistics_by_State/California/Publications/County_Estimates/, red = Riverside, blue = San Bernardino).

APPENDIX B. PBLH comparison of WRF predictions vs. wind profiler measurements at SAC

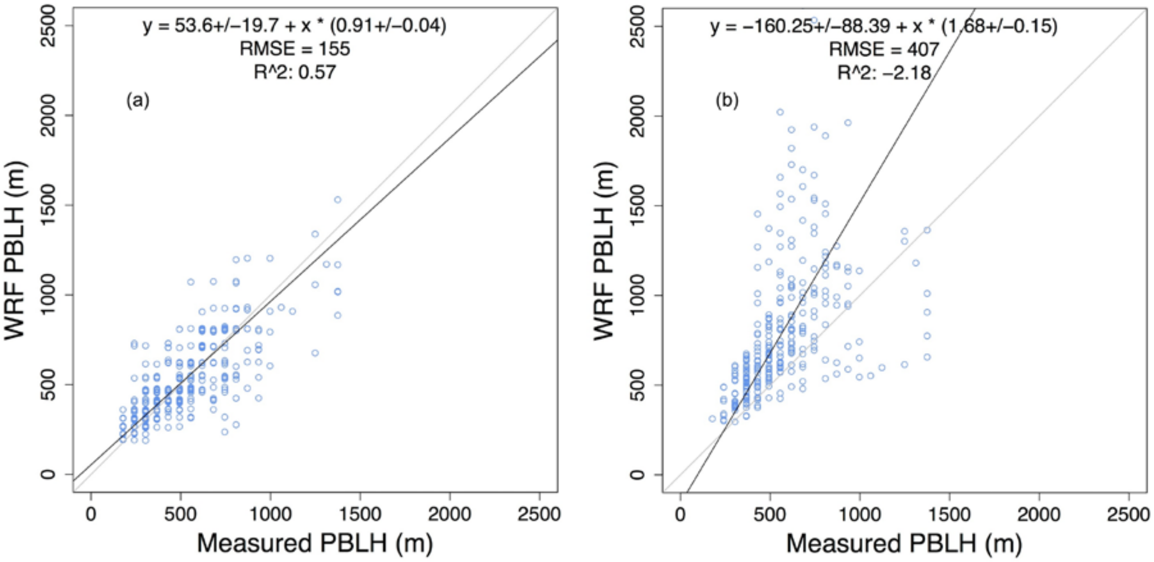

PBLH comparison of WRF predictions vs. wind profiler measurements at the SAC wind profiler site for July 2012: (a) 5-layer thermal diffusion land surface scheme and (b) Noah land surface scheme. As discussed in Jeong et al. [2013], the Noah land surface scheme overestimates PBLH at the Central Valley site.

APPENDIX C. Example of the half Cauchy distribution for the model-measurement mismatch uncertainty

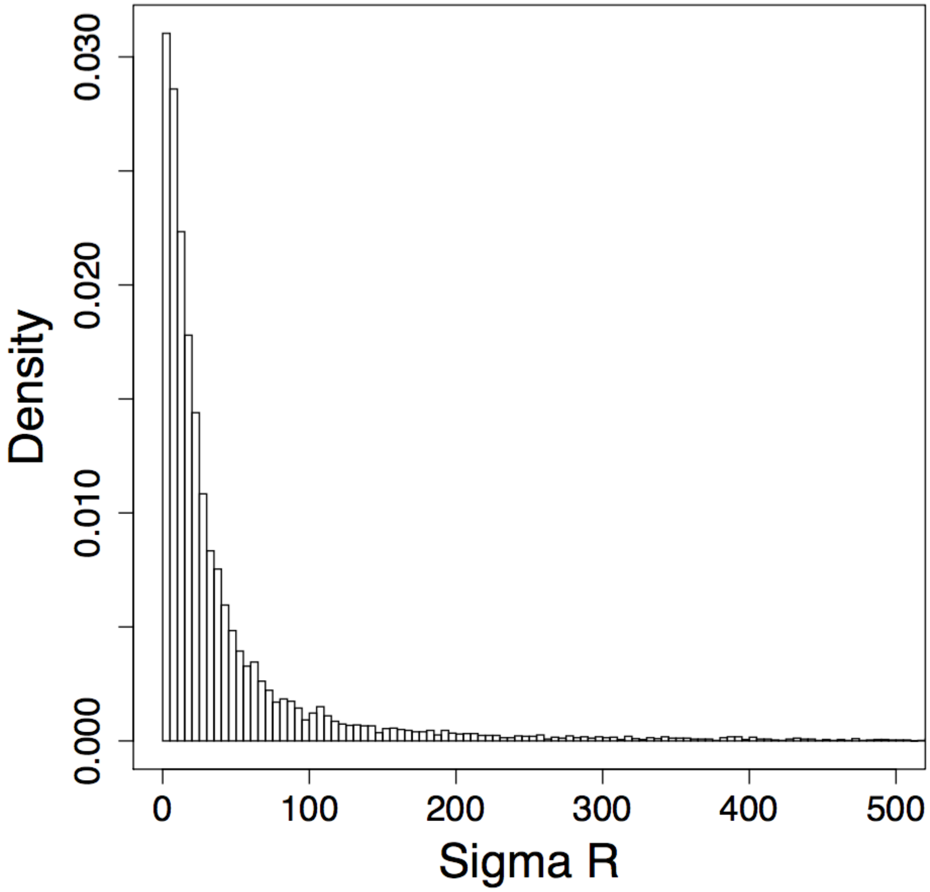

Example of the half Cauchy distribution for the model-measurement mismatch uncertainty with a 50th quantile value of 20 ppb (for the scale parameter) which is similar to those during the summer months. The simulated uncertainty values are positive and yield a long-tailed distribution.

APPENDIX D. Comparison of the model-measurement mismatch uncertainty

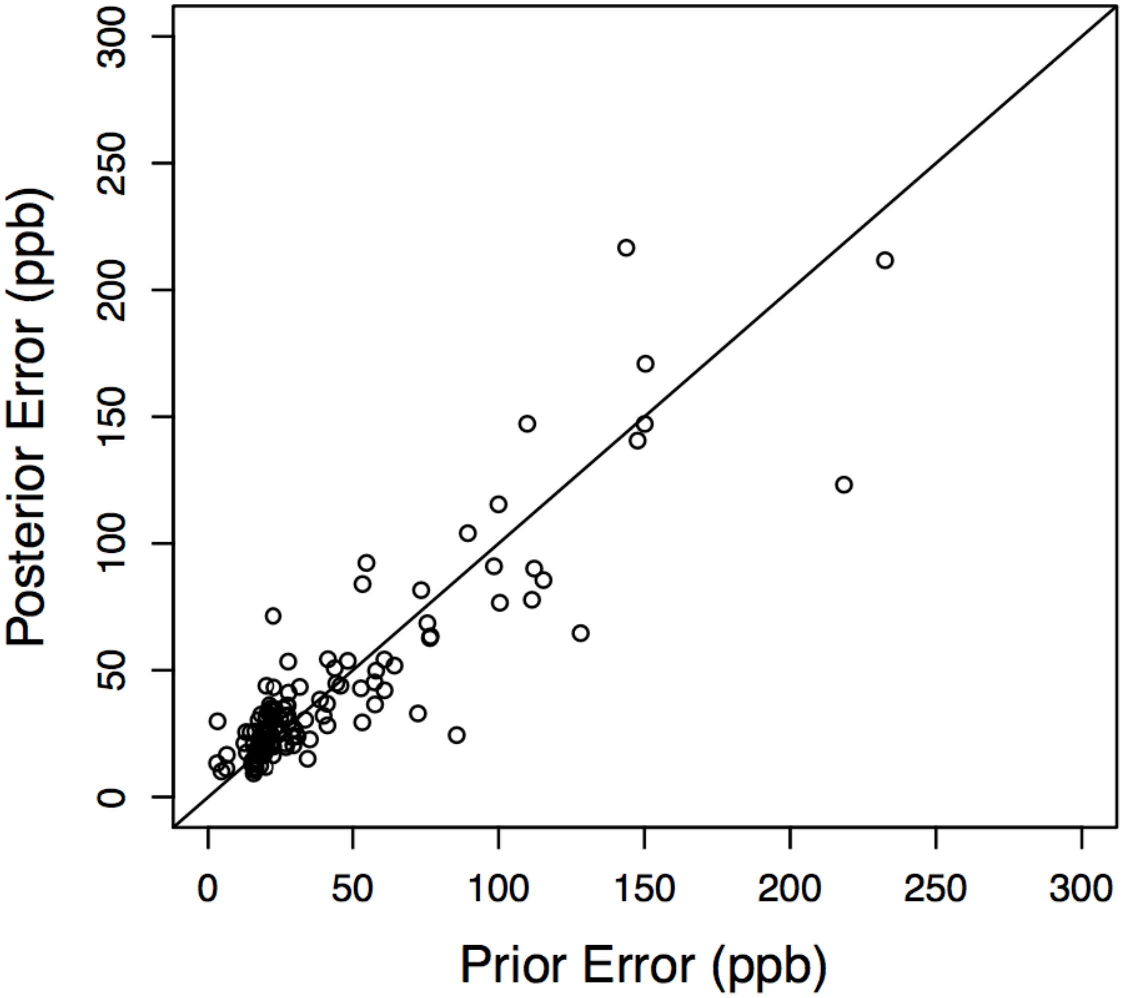

Comparison of the posterior model-measurement mismatch uncertainty, which was optimized, and the prior uncertainty calculated from explicit estimation (e.g., as in Jeong et al. [2013]). The explicit estimation includes errors due to transport (winds and PBL), background, limited number of particles used in STITL simulations, and aggregation. The data points represent the comparison for all 12-month estimates from all sites across California.

APPENDIX E. Example posterior distribution of the uncertainty for the scaling factor (i.e., prior uncertainty) and estimated posterior σ_λ

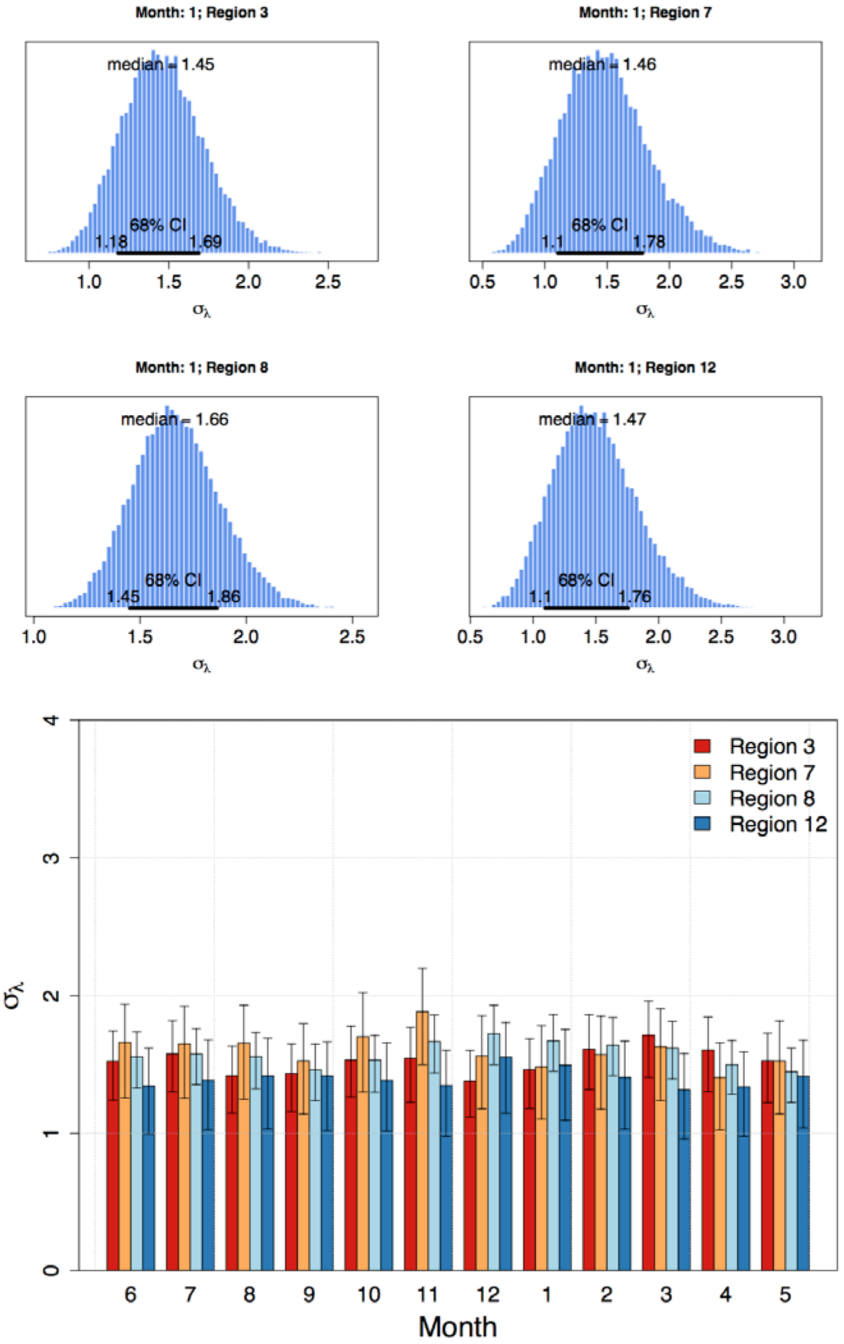

Example (January result) posterior distribution (histogram) of the uncertainty for the scaling factor (i.e., $\boldsymbol{\sigma_\lambda}$) for the major regions (Regions 3, 7, 8 and 12) based on the 25000 samples (upper panel) and posterior $\boldsymbol{\sigma_\lambda}$ averaged for the major regions by month (lower panel). The posterior estimates for individual 0.3° pixels within each region vary, but the region average value shows the overall uncertainty used in the inversion.

APPENDIX F. Initial (prior) estimates of model-data mismatch uncertainty (in units ppb) for CH_4 by site and month*

Site\Month	**6**	**7**	**8**	**9**	**10**	**11**	**12**	**1**	**2**	**3**	**4**	**5**
ARV	28	32	29	61	48	53	144	218	112	111	76	46
CIT	19	20	20	21	22	26	44	55	41	28	23	17
LVR	16	17	16	18	30	58	150	89	28	40	27	19
MAD	23	28	25	61	64	98	150	233	100	77	53	34
SBC	23	22	21	18	12	16	13	18	22	18	15	13
SIO	16	16	15	35	17	30	76	115	41	19	18	3
STB	22	22	22	15	19	39	20	27	27	22	19	21
STR	23	16	15	6	5	41	72	22	3	20	6	5
THD	16	16	15	NA	NA	NA	NA	NA	NA	NA	NA	NA
TRA	21	23	23	58	57	100	110	148	73	44	35	30
TSB	19	21	18	17	20	28	18	24	20	19	23	16
VTR	15	14	16	NA	NA	NA	NA	NA	NA	NA	NA	NA
WGC	18	20	17	25	27	29	86	128	53	31	22	20

*As described in the main report, these uncertainty values (i.e., $\sigma_{R_{p|s}}$, see Section 2.7.4 for details) are used as “prior mean” for posterior estimation of model-data mismatch uncertainties in a hierarchical manner.

APPENDIX G. Initial Estimation of the Model-Measurement Mismatch for Summer CH_4 Emissions

Here we describe the method to explicitly estimate model-data mismatch uncertainties for summer CH_4 emissions. For the other seasons, we assume the uncertainties are proportional to the background-subtracted mean mixing ratios. These estimates are used as the "prior" information for the probability distribution for the model-measurement mismatch uncertainty to estimate its posterior value. Following Gerbig et al. [2003], Zhao et al. [2009], Göckede et al. [2010], and Jeong et al. [2012a; 2013], the model-measurement mismatch matrix, **R** (an $n \times n$ matrix), is represented as the sum of uncertainties in quadrature from several error sources and modeled as a diagonal matrix:

$$\mathbf{R}_i = \mathbf{S}_{\mathrm{meas}} + \mathbf{S}_{\mathrm{part}} + \mathbf{S}_{\mathrm{aggr}} + \mathbf{S}_{\mathrm{bkgd}} + \mathbf{S}_{\mathrm{transPBL}} + \mathbf{S}_{\mathrm{transWIND}},$$

where the measurement error (S_{meas}) is due to the uncertainty in the measurement system. The particle number error (S_{part}) is due to the finite number of released particles at the receptor location while the aggregation error (S_{aggr}) arises from aggregating heterogeneous fluxes within a grid cell into a single average flux. The background error (S_{bkgd}) is due to the uncertainty in estimating the background contribution to the CH_4 measurements at the receptor. $\mathbf{S}_{\mathrm{transWIND}}$ and $\mathbf{S}_{\mathrm{transPBL}}$ represent the uncertainty in CH_4 mixing ratios caused by the errors in winds and the errors in planetary boundary layer (PBL) heights, respectively. The detailed method for estimating each of the uncertainty terms is provided in Jeong et al. [2012a; 2012b; 2013].

For the aggregation error ($\mathbf{S}_{\mathrm{aggr}}$), we adopt the result from Jeong et al. [2012a; 2013] and use 11% of the background-subtracted mean mixing ratio. The background error ($\mathbf{S}_{\mathrm{bkgd}}$) is estimated by combining (in quadrature) the RMS error in the estimation of the 3-D curtain and the standard error of 500 WRF-STILT background samples [Jeong et al., 2013]. Average values for S_{bkgd} were calculated for each month during the summer of

background value has an uncertainty estimate that is the time-, height-, and latitude-dependent root-mean-square (RMS) error of the residuals of the data that were used to construct the background curtain. Only time points for which more than 80% of the particles reached the western boundary of the domain (130°W) were included in the study [Jeong et al., 2013].

To estimate the uncertainty in predicted CH_4 mixing ratios due to errors from modeled PBL heights ($\mathbf{S}_{\mathrm{transPBL}}$), we evaluated WRF model errors in PBL heights and then calculated the RMS difference in CH_4 mixing ratios obtained from simulations with and without input of an additional stochastic component of PBL errors in STILT [Jeong et al., 2013]. We evaluated WRF-simulated PBL heights (*Zi*) using measured data from wind profiler sites across California. The measured PBL heights used in this study were estimated from sub-hourly vertical velocity and returned signal strength (signal-to-noise ratio) data using the algorithms and qualitative analysis following Wyngaard and LeMone [1980], Bianco and Wilczak [2002], and Bianco et al. [2008]. The wind profiler can detect PBL heights from about 150 m to 4000 m with an accuracy of ±200 m [Dye et al., 1995]. Since late 2010, some of the profilers in the Central Valley, which includes Chowchilla (CCL) and Lost Hills (LHS), have stopped operating. Also, the Livermore (LVR) profiler data have not been available since 2011. For those sites, we use the results from Jeong et al. [2012a, 2013]. Wind and *Zi* measurements from the closest profiler to the greenhouse gas (GHG) measurement site were used to evaluate Weather Research and Forecasting (WRF) simulations. For example, most relevant to the WGC GHG measurement site, we compared *Zi* from WRF with measurements from the SAC profiler. For the CIT (Caltech) GHG site, we used the measured *Zi* that were available during the May – June 2010 CalNex campaign period, as described in Newman et al. [2013] to evaluate WRF *Zi*. Newman et al. [2013] showed WRF simulated *Zi* relatively well compared to the measurements during the afternoon hours (RMS error = 246 m). Here, we find the updated WRF model provides somewhat better comparison (RMS error = 166 m) even though we used all June 2010 data including nighttime data. Across all sites, we find WRF simulated *Zi* generally agreed well with the measured *Zi* in a manner consistent results of Jeong et al. [2013]. The mean biases at all sites except LAX (Los Angeles Airport) were less than 200 m, which is within the accuracy of the wind profiler [Dye et al., 1995]. At the LAX site, WRF underestimated *Zi* during the daytime, yielding mean biases of 25 and 38% as a fraction of the measured mean *Zi* for 2012 (we also compared for 2012 summer) and 2013, respectively. However, the low WRF Zi occurs only on a few grid cells near the coast showing a large horizon gradient of Zi from ocean to land. The impact of low WRF Zi on the predicted mixing ratio at CIT and SBC was estimated to be small during the summer season based on the sensitivity analysis of mixing ratios to *Zi*. When STILT was run twice to compare the sensitivity of mixing ratios to *Zi* between the default case and the case with *Zi* decreased by 20%, the difference in mixing ratio was less than 5% of the mean background-subtracted mixing ratio. Also, the CO comparison between predictions and measurements at CIT (near LAX) does not show a significant systematic bias.

Following Jeong et al. [2012a, 2012b, 2013], we estimate the contribution to random error in CH_4 signals (C_{CH4}) due to random variations in PBL to 1st order as the product of RMS uncertainty in PBL depth and CH_4 mixing ratio sensitivity to a PBL perturbation in STILT. Here we estimated the sensitivity using a 20% perturbation in *Zi* to estimate the sensitivity of C_{CH4} to *Zi* (i.e., dC_{CH4}/dZi) and calculated the monthly mean dC_{CH4}/dZi (in units of ppb/m). Then we multiplied the estimated RMS PBL errors (in units of m) by dC_{CH4}/dZi to estimate CH_4 mixing ratio errors (in ppb) associated with *Zi* for each site. As in Jeong et al. [2013], when the measured *Zi* is not available for a given month, we assume that the RME errors do not vary significantly during this summer season and thus used the result from available adjacent month or the results from Jeong et al. [2012a, 2013]. In fact, comparing different months during the two different years, we found that the RMS errors during the summer months are all less than the nominal accuracy of 200 m for the wind profiler. Thus, we used the RMS error of 200 m for all sites where the estimated RMS errors are less than 200 m [Jeong et al., 2013]. Combining the 200 m RMS error with the sensitivity of mixing ratios to *Zi*, the estimated uncertainties for these summer months ranged from ~2 ppb to over 10 ppb, which are lower than those of the other seasons reported in Jeong et al. [2013].

To estimate the combined uncertainty in CH_4 mixing ratios due to winds ($\mathbf{S}_{\text{transWIND}}$) and particle number ($\mathbf{S}_{\text{part}}$) we followed the approach originally developed by Lin and Gerbig [2005] and applied previously by Jeong et al. [2013]. Here, we examined wind errors for the summer months where measured winds were available. In general, WRF simulated winds were consistent with the measurements for both Central Valley and SoCAB sites. We excluded a few episodic events that showed large biases in wind speeds and/or directions (e.g., June 4th – 7th, 2013 at LAX) from the inversion as in Jeong et al. [2013]. In this study we used results from Jeong et al. [2013] for the Central Valley sites and computed new results specific to SoCAB. Following Jeong et al. [2013], we ran the STILT model 10 times and computed 10 ensemble mixing ratios to estimate the RMS variation of CH_4 mixing ratios about the mean of the ensemble mixing ratios. The results for the SoCAB suggest wind and particle number uncertainties are 3 – 7 ppb, which are 3 - 9% of background-subtracted mean mixing ratios.

Following previous work, we assume that individual uncertainty terms are independent and are summed in quadrature to populate the diagonal elements of the model-measurement mismatch matrix [Jeong et al., 2012a; 2012b; 2013; Göckede et al., 2010]. Resulting uncertainties for the model-measurement mismatch during the summer months varied from ~ 15 to 30 ppb. As described, the uncertainties for the summer months were explicitly estimated here, and those of the other months were assumed to be proportional to the mean background-subtracted mixing ratios or were adopted from Jeong et al. [2013]. The explicitly estimated values for the model-measurement mismatch for the entire inversion period are provided by site in Appendix F. Note that these explicit estimates (i.e., $\sigma_{R_{p|s}}$) are used as “prior” information for posterior estimation of model-data mismatch uncertainties in the form of a scale parameter for the half Cauchy distribution (see Section 2.7.3 in the main report).

APPENDIX H. Posterior annual state CH_4 emission (CH_4 Gg/yr) by sector

Sector	DLS	NDLS	LF	NG	PL	WW	DNDC	WL
Prior	738	157	335	283	40	67	49	38
Posterior Median	1070	263	463	391	58	86	52	66
Posterior (Upper)[a]	1410	345	579	502	78	129	133	118
Posterior (Lower)[b]	804	199	359	305	43	54	33	40

[a] 97.5th percentile

[b] 2.5th percentile

APPENDIX I. Identified natural forest pixels (~10 km) in California

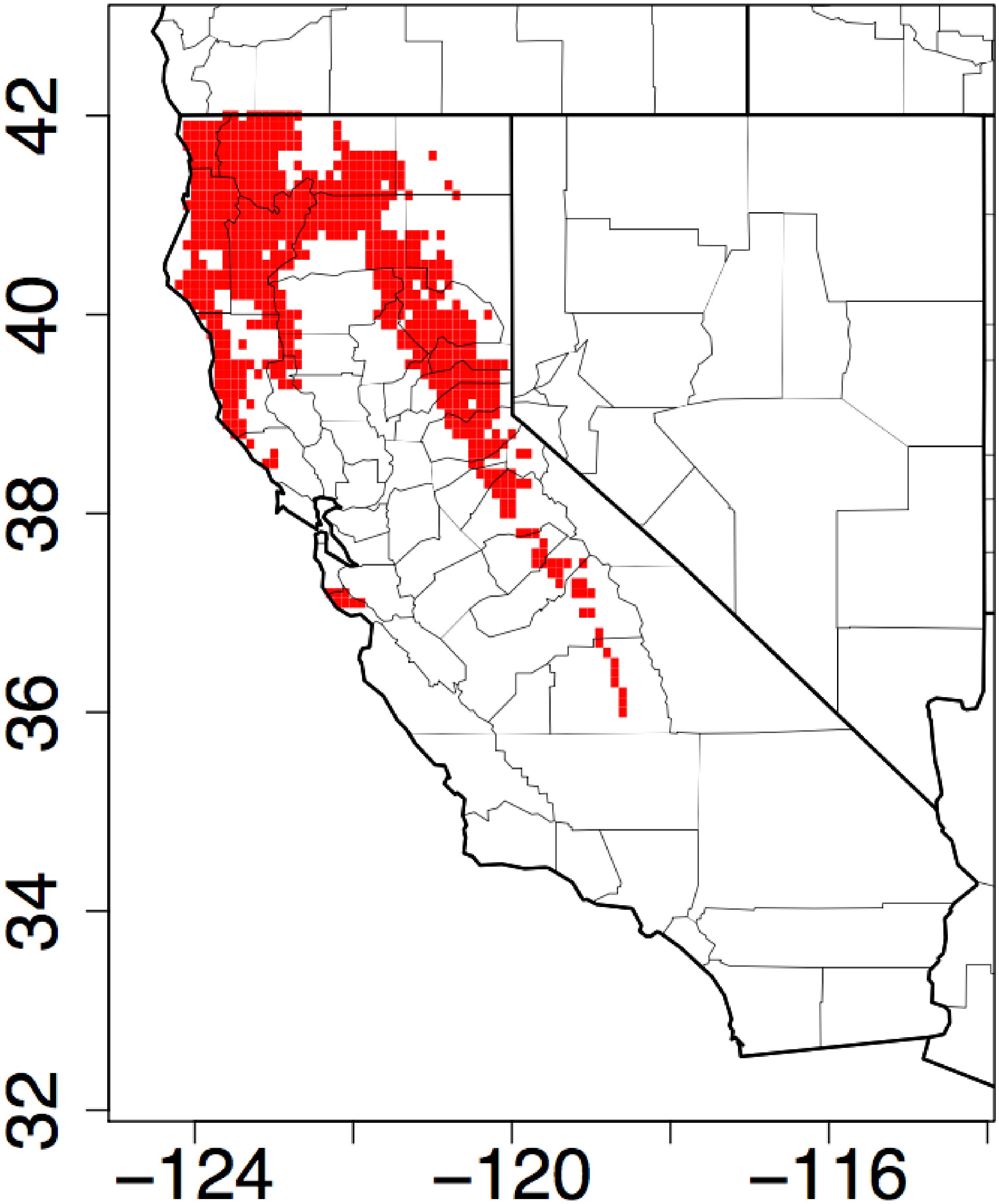

Identified natural forest pixels (~10 km) in California using MODIS.

APPENDIX J. Derived natural forest N_2O emissions

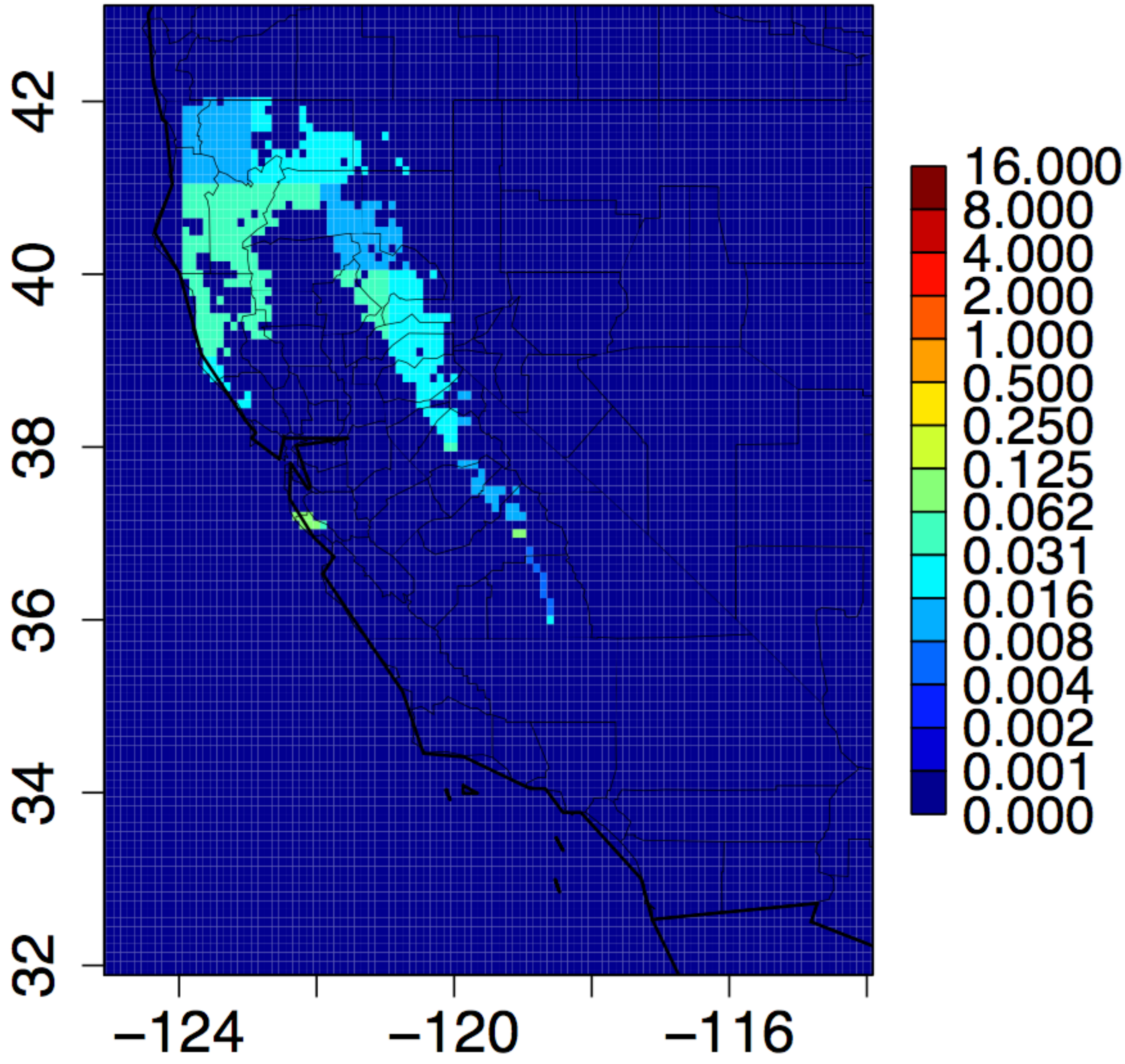

Derived natural forest N_2O emissions (nmol/m^2/s) based on GEIA emissions.

APPENDIX K. GEIA ocean N_2O emissions

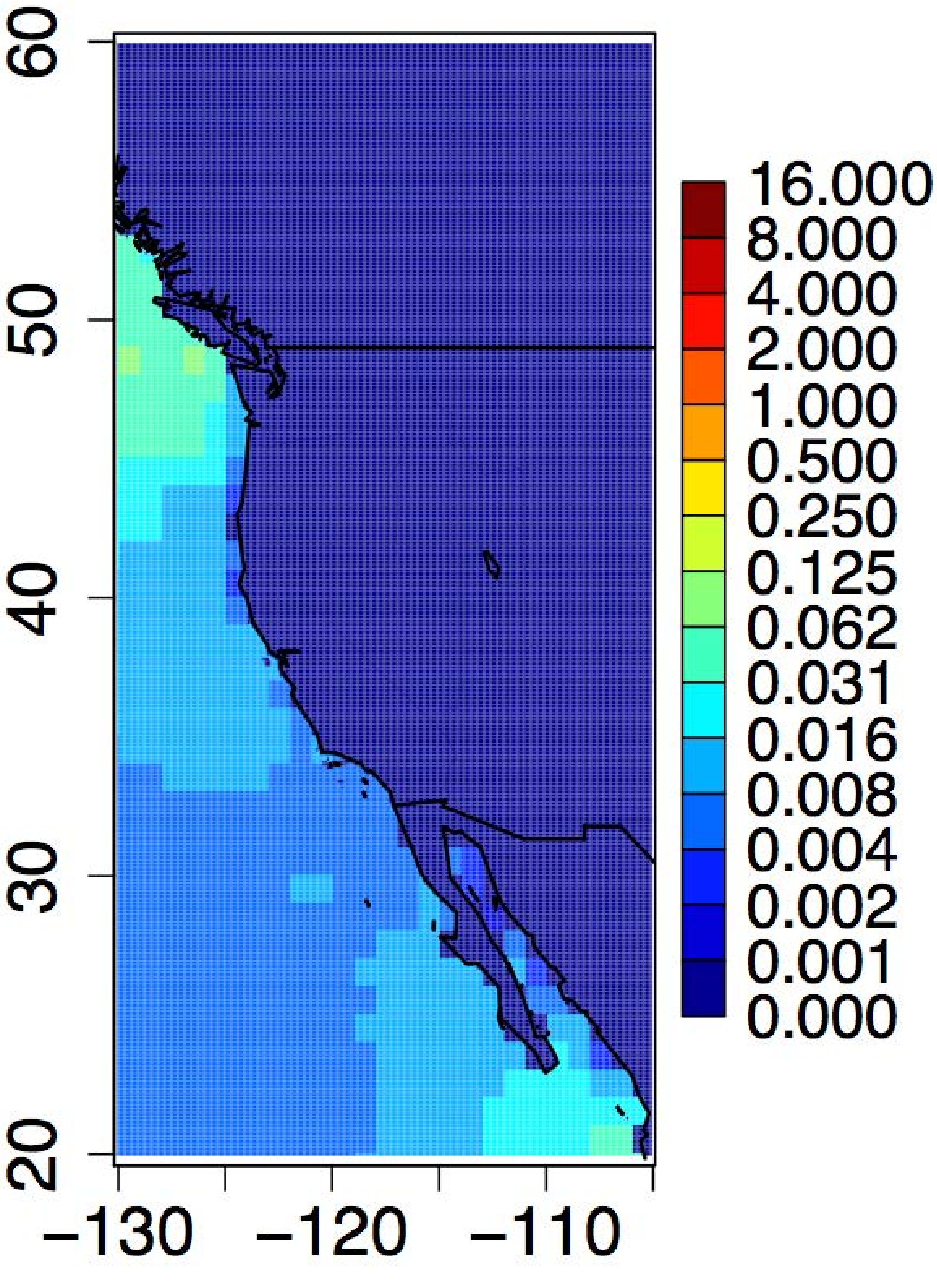

Regridded (at 10 km resolution) GEIA ocean N_2O emissions (nmol/m^2/s) for the entire model domain.

APPENDIX L. Example posterior distribution of the N_2O prior uncertainty ($\boldsymbol{\sigma_\lambda}$)

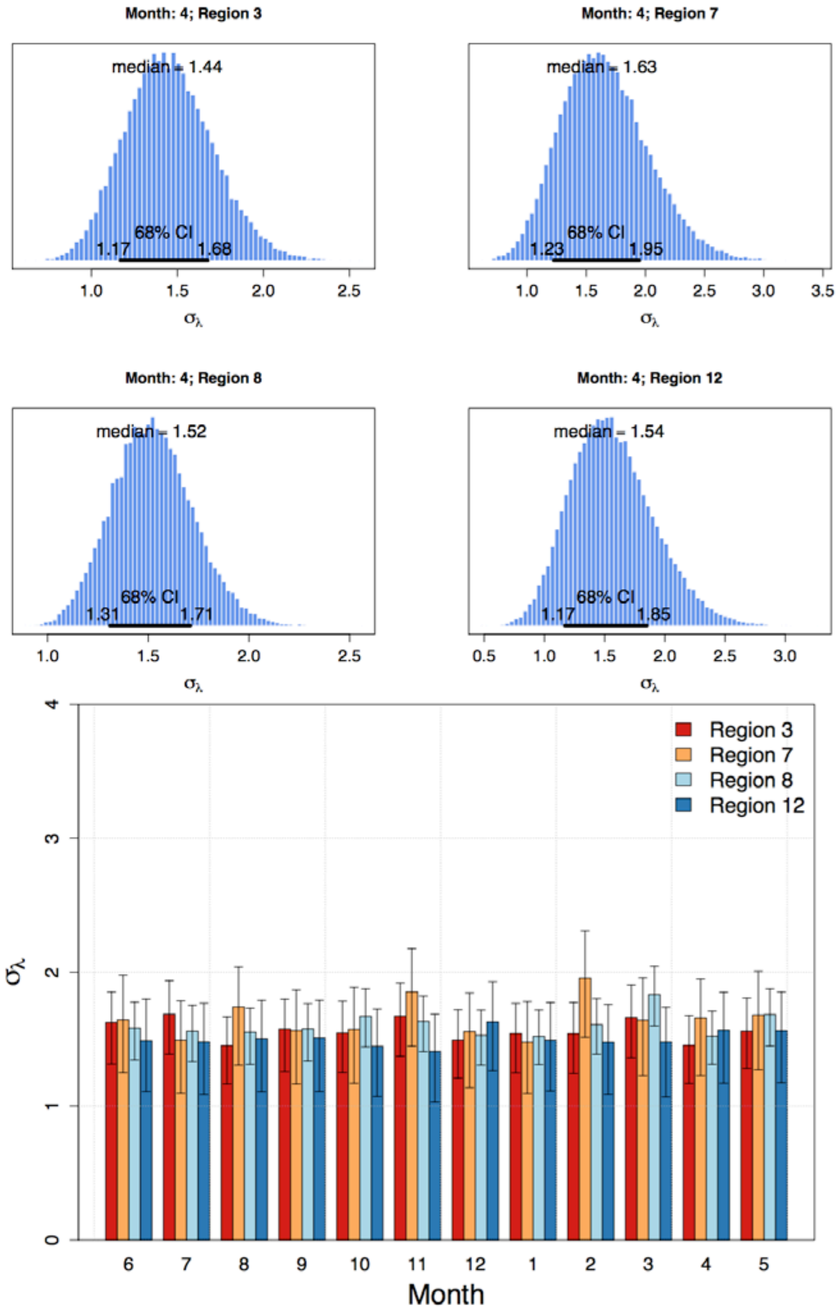

Example (April result) posterior distribution (histogram) of the N_2O prior uncertainty (i.e., $\boldsymbol{\sigma_\lambda}$) for the major regions (Regions 3, 7, 8 and 12) based on the 50000 samples (upper panel) and posterior N_2O $\boldsymbol{\sigma_\lambda}$ averaged for the major regions by month (lower panel). The posterior estimates for individual 0.3° pixels within each region vary, and the region average value shows the overall uncertainty used in the inversion.

APPENDIX M. Predicted monthly mean mixing ratios for ocean and forest

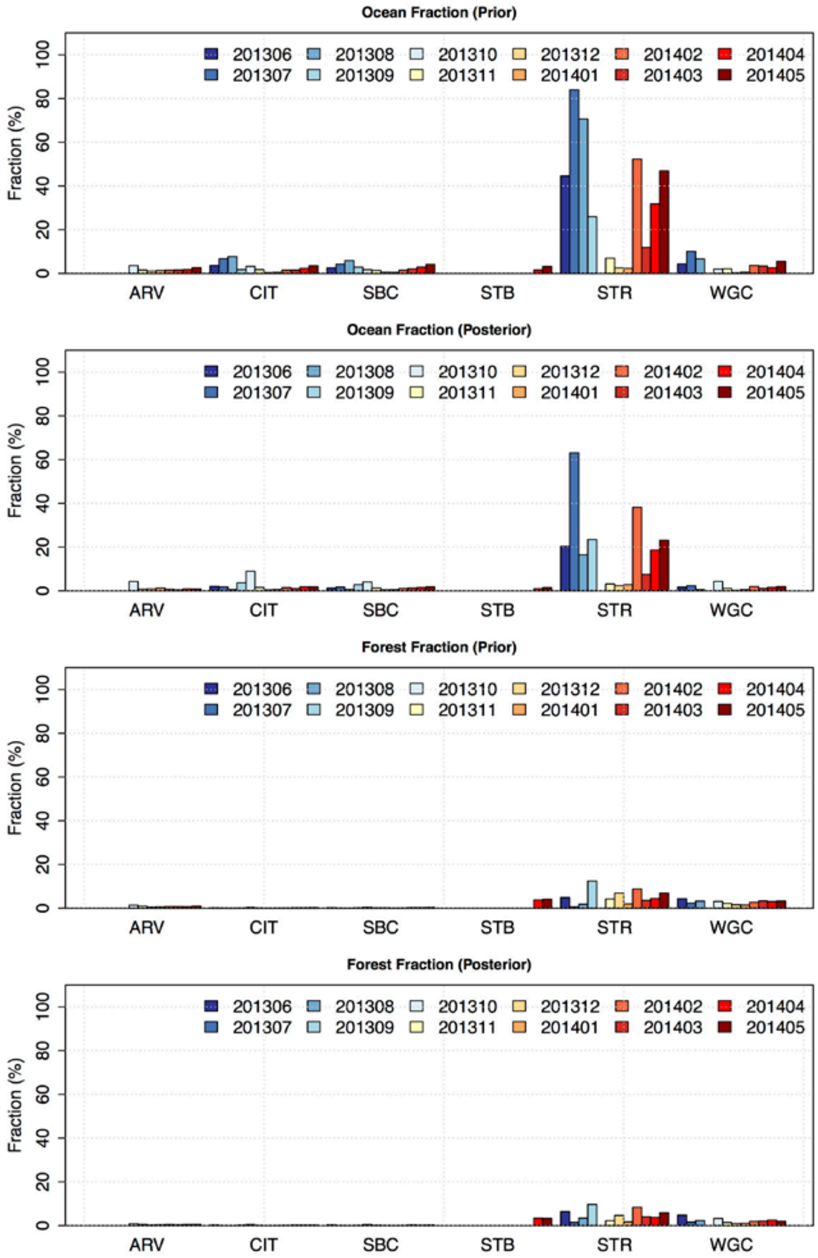

Predicted monthly mean mixing ratios for ocean and forest as a fraction (%) of the total prediction by site and month. The top two panels show the ocean fraction before (prior) and after (posterior) inversion, respectively, and the bottom panels show the forest fraction before and after inversion. Except for the coastal site, STR, the fraction for both forest and ocean is less than ~10%. The natural ocean N_2O is distributed over the large area in the eastern Pacific. However, because most of the measurement sites are inland where the footprint influence of ocean emissions is weak, ocean signals are small except for STR.

APPENDIX N. Annual state anthropogenic posterior emissions (Gg N_2O/yr) for N_2O by sector

Sector	AGS	MNM	AWB	IPU	EMT	IDE	N2O	OPR	RCO	WST	TNR	TRO
Prior	15.3	9.5	0.2	9.7	0.3	0.2	4.4	0	0.2	2.9	0.2	5.5
Posterior (Median)	29.0	17.7	0.3	14.8	0.5	0.3	8.3	0.0	0.3	4.5	0.3	10.1
Posterior (Upper)[a]	37.3	23.9	0.4	19.4	0.7	0.6	10.7	0.0	0.4	5.9	0.5	13.6
Posterior (Lower)[b]	21.6	12.6	0.2	10.8	0.4	0.2	6.2	0.0	0.2	3.4	0.2	7.4

[a] 97.5th percentile

[b] 2.5th percentile